NMR RELAXATION METHODS TO DETECT PROTEIN DYNAMICS: EVALUATION OF ACCURACY, IMPROVEMENT OF THE METHODOLOGY, AND ITS APPLICATION

by

Wazo Zaw Myint

BS in Chemistry, University of Richmond, 2006

Submitted to the Graduate Faculty of

School of Medicine in partial fulfillment

of the requirements for the degree of

Doctor of Philosophy

University of Pittsburgh

2013

UNIVERSITY OF PITTSBURGH

School of Medicine

This dissertation was presented

by

Wazo Zaw Myint

It was defended on

July 23, 2013

and approved by

Dr. Billy W. Day, Professor, Department of Pharmaceutical Sciences, Department of Chemistry, Department of Environmental & Occupational Health, Department of Computational & Systems Biology, Clinical & Translational Sciences Institute.

Dr. Pei Tang, Professor, Department of Anesthesiology, Department of Pharmacology and Chemical Biology, Department of Computational and Systems Biology, Department of Structural Biology.

Dr. Daniel M. Zuckerman, Associate Professor, Department of Computational & Systems Biology.

Committee Chair: Dr. Gordon S. Rule, Professor, Department of Biological Sciences, Carnegie Mellon University

Dissertation Advisor: Dr. Rieko Ishima, Associate Professor, Department of Structural Biology.

NMR RELAXATION METHODS TO DETECT PROTEIN DYNAMICS: EVALUATION OF ACCURACY, IMPROVEMENT OF THE METHODOLOGY, AND ITS APPLICATION

Wazo Zaw Myint, PhD

University of Pittsburgh, 2013

Proteins are dynamic molecules whose ability to undergo conformational changes and fluctuations can impact their biological function, such as enzyme catalysis and substrate recognition. Mutations or perturbations that do not significantly change protein structure can often have a significant effect on the function by disrupting important internal motions and conformational states. Due to the importance of protein dynamics on function, dynamics have been extensively studied by many different biophysical methods as well as computational means. One of the methods to characterize protein dynamics is by nuclear magnetic resonance (NMR) spectroscopy. NMR spectroscopy is a powerful tool for the characterization of the structure as well as the dynamics of biological molecules. In particular, NMR relaxation experiments have been used to characterize protein motion in a wide range of timescales ranging from sub-nano second (ns) motions up to millisecond (ms) and above. Recent advances in instrumentation, such as the introduction of commercially available cryogenic probes and higher field static magnets (with ^{1}H Larmor frequency of 900 MHz and above), have increased the sensitivity of NMR experiments. However, reevaluation of the methods used in NMR relaxation experiments and the analysis of the data is required to confirm whether the same experimental methods remain valid for the improved instrumentation. In this thesis, the NMR relaxation experiments were evaluated and improvements in the experimental aspects and the analysis of the NMR relaxation data are made for high resolution NMR experiments. In addition, NMR relaxation experiments

were used to investigate the dynamics of the Sarcoplasmic Reticulum Ca^{2+} ATPase and the Human Immunodeficiency Virus Type 1 Protease wild-type (WT) and mutant forms.

TABLE OF CONTENTS

LIST OF TABLES

LIST OF FIGURES

PREFACE

I am grateful to my thesis advisor, Prof. Rieko Ishima for all her direction and guidance throughout my graduate studies. From her, I gained significant knowledge of biophysics and structural biology as well as learned how to be a scientist. She has been a fountain of support and guidance through the many research projects presented in this thesis.

I would also like to thank my dissertation committee members: Prof. Gordon Rule, who served as my committee chair, Prof. Billy Day, Prof. Pei Tang, and Prof. Daniel Zuckerman for their guidance, suggestions, and stimulating discussions through my graduate work.

I would also like to thank the department of Structural Biology and the Molecular Biophysics and Structural Biology program. The teachers through my courses ingrained in me the essential skills necessary to pursue my scientific study.

Finally, I would like to thank my family and my friends for their love and continued support.

1.0 INTRODUCTION

In the field of biophysics and structural biology, the relationship between the structure and function of biological molecules has been extensively studied to gain better understanding of how they function. In the case of proteins, detailed atomic and molecular level structures determined from a variety of biophysical methods (such as X-ray crystallography, Nuclear Magnetic Resonance spectroscopy, and Cryo-electron microscopy.) have been useful in getting insight into protein function. However, proteins are dynamic molecules and the internal motions and conformational changes of proteins are important for their function. Full understanding of the mechanism of protein function can not be obtained based only on structural information but require characterization of the associated internal dynamics.

Many different experimental and computational methods have been used to characterize internal motions of proteins. NMR relaxation experiments are one set of methods that have been widely used to study the dynamics of protein backbone and side-chain (34; 152; 86; 51; 153; 21; 166; 96). For the characterization of the protein backbone motions, experiments to measure the backbone amide ^{15}N longitudinal relaxation rate, R_1, transverse relaxation rate, R_2, and $\{^1H\}$-^{15}N nuclear Overhauser enhancement ($\{^1H\}$-^{15}N NOE) are useful in the elucidation of the sub-nano second timescale motions (34; 152; 153; 21; 96). For a more quantitative characterization of

internal motions from the backbone relaxation parameters, model-free analysis (116; 117) can be performed to extract order parameters (S^2) and timescales of internal motions (τ_i) which describe the amplitudes and timescales of motion independent of the overall molecular tumbling.

In addition to the sub-nano second dynamics, constant time Carr-Purcell-Meiboom-Gill (CT-CPMG) R_2 relaxation dispersion experiments can be employed to characterize millisecond to microsecond timescale dynamics and conformational populations (120; 191; 200; 179; 190; 201; 15; 37). These experiments have been utilized extensively to characterize biological function in proteins. However, advances in NMR spectrometer hardware (cryogenic probes (186; 185) and high field magnets (126; 141)) have increased sensitivity and reduced experimental noise in NMR experiments. Since NMR relaxation experiments are often used to characterize small differences (such as 1% populated intermediate states (105; 106)), the experimental methods and the processing protocols need to be reevaluated and if necessary, more accurate relaxation experiments and data analysis methods need to be developed to avoid misinterpretation of relaxation data. ***The aim of the thesis is to determine the accuracy of protein NMR relaxation methods and how these methods can be improved to ensure correct interpretation of relaxation data to characterize protein dynamics.*** To this end, the current NMR relaxation methods and the associated errors were evaluated by experiment and simulation. In addition, optimized methods of data processing will be used in the evaluation of experimental data for the study of biological problems. In the next two sections, a general overview of NMR methods and the experiments analyzed in this thesis will be outlined.

1.1 SOLUTION NMR SPECTROSCOPY FOR THE STUDY OF PROTEINS

Advances in protein NMR spectroscopy have allowed for detailed characterization of structure and dynamics. The development of Fourier Transform NMR(109) as well as multidimensional NMR(39) methods have significantly improved the applicability of NMR spectroscopy for studying proteins by allowing for faster experiments and correlation of resonances between spatially proximal or bound nuclei. Advances in molecular biology methods have allowed for isotopic enrichment of NMR sensitive ^{13}C and ^{15}N nuclei and overexpression of proteins in *E. coli* have made sequential backbone assignment of backbone $^{13}C\alpha$, ^{13}CO, ^{1}H, and ^{15}N atoms possible(199; 80; 97; 163; 17; 62). The assignment of protein backbone resonances can also aid in the resonance assignment of the directly bound side chain atoms and provide information on the dynamics and conformational states of both the protein backbone and sidechain. Furthermore, as mentioned above, the development of high field (^{1}H Larmor frequencies of 900 MHz and above(126; 141)) NMR spectrometers as well as cryogenically cooled probes (186; 185) have significantly increased the sensitivity and resolution of NMR experiments.

Multi-dimensional NMR experiments that correlate the resonance frequency of the backbone nuclei of one amino acid residue (i residue) with that of the preceding (i_{-1}) or the succeeding (i_{+1}) residue are typically used for the sequential assignment of the protein backbone and sidechain nuclei ($^{13}C\alpha$, $^{13}C\beta$, ^{13}CO, ^{1}H, and ^{15}N). For example, the 3-dimensional HNCA experiment (97) provides correlation between the ^{1}H and ^{15}N nuclei of the backbone amide group with the $^{13}C\alpha$ chemical shifts of the i residue and

the i_{-1} residue. The connectivity information can be used in a daisy chain process (linking the i_{-1} residue with the i residue and the i residue with the succeeding i_{+1} residue etc.) to complete assignment of the backbone ^{15}N, ^{1}H, and $^{13}C\alpha$ nuclei. To distinguish possible ambiguities on which resonances originate from the i and i_{-1} residue, HN(CO)CA experiment (14) can be performed, which only shows correlation of the backbone ^{1}H and ^{15}N with the i_{-1} $^{13}C\alpha$ nuclei and not the i $^{13}C\alpha$ resonance.

Other experiments, such as the CBCA(CO)NH(60) and the HNCACB(61) experiments (which provide similar correlation information as the HN(CO)CA and the HNCA experiments with the addition of $^{13}C\beta$ resonances) or the HNCO experiment (97) (which provide correlation of the backbone ^{1}H and ^{15}N resonances with the ^{13}CO resonance) can aid in the assignment of the protein backbone nuclei. The assignment of additional sidechain nuclei can be performed using the HCCH-TOCSY experiment(13; 147) that show correlation of resonances of the sidechain ^{13}C atoms to the backbone nuclei ($^{13}C\alpha$ and $^{1}H\alpha$). In this thesis, the experiments outlined above were utilized to aid in the sequential backbone resonance assignment.

The NMR resonance assignments for backbone and sidechain atoms can be used for the study of both structural as well as dynamical aspects of the protein. Chemical shifts reflect the overall chemical environment of the nuclei and changes in the backbone ^{1}H, ^{13}C, and ^{15}N chemical shifts can reflect changes in the protein's conformation, presence of bound ligand, or differences in side chain due to mutation. In my thesis work, backbone ^{1}H and ^{15}N chemical shift differences between wild-type (WT) and mutant forms of proteins as well as chemical shift changes on ligand binding are

compared for a qualitative characterization of conformational changes and residues involved in ligand binding.

1.2 DYNAMICS INFORMATION FROM NMR RELAXATION EXPERIMENTS

NMR relaxation experiments can be used to characterize internal molecular motion of proteins in the nanosecond to picosecond (ns-ps) timescale and also in the millisecond to microsecond timescales (ms-μs). In particular, protein ^{15}N longitudinal relaxation rate, R_1, transverse relaxation rate, R_2, and the $\{^1H\}$-^{15}N heteronuclear Overhauser enhancement, $\{^1H\}$-^{15}N NOE, parameters have been used to characterize the overall flexibility of the protein backbone(40; 152; 86; 153; 166; 96).

The R_1 rate, which is also known as the spin-lattice relaxation rate, represents the relaxation of the longitudinal (collinear with the static magnetic field) component of the bulk nuclear magnetic spin vector from the excited state to the equilibrium state with the release of the energy into the lattice(1). Unlike in UV-visible absorbance or fluorescence (photoluminescence) spectroscopy, the relaxation of the nuclear spin from an excited state to the equilibrium state does not occur through thermal vibrations or through emission of photons since the energy level differences between the excited and ground states in NMR is significantly smaller(1). Relaxation is stimulated by fluctuations in the effective local magnetic field observed by the nucleus. The local magnetic field on the nucleus is often different from the overall static field due to shielding of the static field by electron clouds and to coupling of the nuclear magnetic dipoles with other (either nuclear or electronic) magnetic dipoles in the proximity of the atom. In the case

of protein backbone amide ^{15}N spin, the R_1 relaxation rate is driven by fluctuations in the effective magnetic field due to the chemical shift anisotropy (CSA) and the dipolar coupling (DD) interactions experienced by the nuclear spin. (181; 122) Changes in the local magnetic field by CSA and DD interactions can be dependent on molecular motions that arise from protein rotational or translational motions as well as internal motions of the protein such as conformational changes and loop motions.

The R_2, which is also known as the spin-spin relaxation, describes the rate of relaxation of the transverse component of the bulk nuclear magnetic resonance spin vector back to equilibrium state from a coherent non-equilibrium state. (1) The R_2 differs from the R_1 in that the transverse relaxation does not result in a change in the energy levels of the nuclear spin and only reflects the dephasing of transverse nuclear spin coherence due to fluctuations in the local magnetic field from CSA and DD interactions. (181; 122) Although the mechanisms of relaxation are similar between R_1 and R_2 relaxation rates, the frequency dependence of magnetic field fluctuations are different and for large biological molecules, the rates are typically different. Furthermore, the R_2 rate can also be increased by presence of conformational exchange in the ms-μs timescale that leads to chemical exchange. Chemical exchange is a phenomenon where the nucleus undergoes exchange between two or more distinct chemical environments that contributes to R_2 relaxation, R_{ex}(26; 171). Below, an experiment for the characterization of chemical exchange that is analyzed in this thesis will be overviewed.

The $\{^1H\}$-^{15}N NOE parameter is the steady state Nuclear Overhauser Enhancement which is sensitive to ns-ps timescale motions(143; 171). The steady

state {^{1}H}-^{15}N NOE results from the dipolar cross relaxation of the ^{15}N nucleus due to the directly attached amide ^{1}H nucleus(143; 171). The {^{1}H}-^{15}N NOE is determined by comparing the equilibrium ^{15}N magnetization to the steady state ^{15}N magnetization in the presence of ^{1}H magnetization that is saturated by r. f. pulses(40; 143; 171). The magnitude of the steady state ^{15}N magnetization is dependent on internal motions in the ns-ps timescale. (40; 143; 171)

Although the backbone ^{15}N R_1, R_2, and {^{1}H}-^{15}N NOE rates reflect the internal motions of the protein, they also depend on the overall molecular motion, which is typically in the ns timescale for most proteins. A more quantitative interpretation of the internal motion can not be directly derived from the parameters. Lipari-Sazbo model free analysis (116; 117) and improvements to the method (12; 125) are used to extract the internal motion of the N-H backbone amide bond vector from the overall global molecular tumbling of the protein. Model free analysis assumes a simple model of motion and relates the experimental R_1, R_2, and {^{1}H}-^{15}N NOE parameters to the overall tumbling of the molecule, τ_R, as well as a generalized order parameter (which describes the amplitude of internal motions), S^2, and a timescale of internal motion, τ_i. Assuming a single τ_R for all residues in the protein(116; 117), the S^2 and τ_I parameters can be determined for each residue. In my thesis, the experiments used to measure the R_2 rate were analyzed in detail and suggestions for improvement of the methodology are presented. In addition, model free analysis was used to characterize the effect of mutation on the internal dynamics.

The Constant Time Carr-Purcell-Meiboom-Gill (CT-CPMG) R_2 relaxation dispersion experiment is one experiment used for the characterization of slower motions

in the ms-μs timescale(120; 51; 191; 200; 179; 190; 201; 15; 37). The CT-CPMG R_2 relaxation dispersion experiments have been beneficial in the characterization of protein motions necessary for enzyme catalysis, ligand binding, and protein folding. In the CT-CPMG experiment, the R_{ex} due to chemical shift is modulated by varying the frequency of 180º ^{15}N refocusing pulses in the CPMG pulse sequence. By comparing the dependence of the observed R_2 (which includes the intrinsic R_2 as well as R_{ex}) on the spacing of the ^{15}N refocusing pulses and optimizing the experimental data to solutions(25; 94) to the Bloch-McConnell equations (130) (which describes chemical exchange), the timescales, populations of exchanging conformations, chemical shift difference between conformations, and the intrinsic R_2 rates can be determined. The populations of minor conformational states can give insight into functionally important minor states. In my thesis, the error analysis involved in CT-CPMG R_2 relaxation dispersion experiments were evaluated and the experiments were applied to the study of mutation effects on the minor conformation populations of the Human Immunodeficiency Virus (HIV) Type-1 protease(22).

1.3 SUMMARY OF GOAL AND SUBPROJECTS

Dynamics determined from NMR relaxation experiments can provide insight into the mechanism of protein function. However, due to improvements in NMR instrumentation, the NMR relaxation experiments used to study protein dynamics need to be reevaluated to ensure accuracy of the relaxation data. For this purpose, I evaluated the effectiveness of ^1H decoupling pulse sequences (Chapter 2), estimated

the magnitude of errors in the CT-CPMG R_2 relaxation dispersion experiment (Chapter 3), compared different methods of R_2 error estimation (Chapter 4), and tested the applicability of a phase alternating pulse sequence (Chapters 3 and 4).

In addition, I worked towards improving the methodology for incorporation of the phase alternating pulse sequence in the CT-CPMG R_2 relaxation dispersion experiment (Chapter 3), estimation of error in R_2 experiments (Chapter 4), and model selection for model free analysis (Chapter 6). Also, I applied relaxation experiments and other biophysical methods for the study of biological problem in my characterization of mutation effects in the Sarcoplasmic Reticulum Ca^{2+} ATPase nucleotide binding domain (Chapter 5) and evaluation of differential flap dynamics in the WT and mutant HIV protease (Chapter 6).

2.0 PRACTICAL ASPECTS OF ^{15}N CPMG TRANSVERSE RELAXATION EXPERIMENTS FOR PROTEINS IN SOLUTION

The ^{15}N transverse relaxation as measured by the Carr-Purcell-Meiboom-Gill (CPMG) sequence is often used to characterize protein backbone dynamics in solution. In the ^{15}N CPMG experiment, the delay between ^{15}N CPMG pulses typically is set sufficiently short to minimize the effects of relaxation by the ^{15}N-^{1}H antiphase component. This limits the total relaxation duration of the CPMG experiment because frequent application of the high B_1 field to the heteronucleus may cause probe damage. The resulting antiphase component can be minimized by using ^{1}H composite decoupling or by applying ^{1}H 180° pulses more frequently than the ^{15}N CPMG pulses. In this study, we simulated ^{15}N CPMG relaxation in the presence of either ^{1}H composite decoupling or ^{1}H 180° pulses and compared the results with the experimental transverse relaxation data acquired with [u-^{15}N]- or [u-^{15}N, u-^{2}H]- ubiquitin samples. We explain systematic errors resulting from these CPMG experiments and describe a method for recording ^{15}N transverse relaxation in a manner that minimizes probe problems. The results presented in this chapter have been published in *Concepts in Magnetic Resonance Part A*, 2009, 34A:63-75. In this chapter, my main contributions were the simulations of the pulse sequences.

2.1 INTRODUCTION

NMR relaxation is well suited for the characterization of the internal motion of individual sites within proteins (34; 86; 51; 153; 21; 166; 96; 79; 93). The ^{15}N transverse relaxation rate (R_2) is of particular interest because it is sensitive to motions close to zero frequency and is indispensable in model-free analysis to detect protein backbone dynamics (99; 30; 152). Furthermore, R_2, measured by either the Carr-Purcell-Meiboom-Gill (CPMG) or the spin lock experiment, can be used to characterize chemical exchange (33; 150; 90; 135). Typically, in a ^{15}N CPMG transverse relaxation experiment, 180° proton pulses are applied every 5-10 ms to suppress cross correlation between ^{15}N-^{1}H dipolar interaction and ^{15}N chemical shift anisotropy (CSA). In addition, the half duration between the CPMG 180° ^{15}N pulses, τ_N, must be set sufficiently short (< 0.5ms) to reduce generation of the antiphase component (59; 158; 98; 155). Reduction of the antiphase component is important for obtaining accurate ^{15}N R_2 values because the antiphase component relaxes by both ^{1}H spin-flip effects and ^{15}N transverse relaxation (98).

To conduct the ^{15}N CPMG experiment with a short τ_N, the total CPMG relaxation period must be relatively brief to prevent probe damage. For example, for an NMR probe that has a specification of ^{15}N decoupling at 1.47 kHz B_1 field strength for 140 ms, we estimate that ^{15}N CPMG pulses of 5 kHz B_1 field and a 10% duty cycle (as an average power against the time) should be applied for less than 100 ms, with ^{15}N GARP

decoupling at 0.83 kHz for 50 ms during the spectral acquisition. However, a 100 ms period may not be sufficiently long for CPMG experiments on mobile regions in proteins. Additionally, a 5 kHz B_1 field may not sufficiently cover the full spectral range for ^{15}N CPMG experiments carried out at very high magnetic field strengths. Depending on the probe design, a 10% CPMG duty cycle may still cause heating. Because acquisition decoupling of 50 ms at 0.83 kHz B_1 field strength deposits the same energy in the probe as a 1.47 kHz field applied for only 16ms, the probe's power limit may reach even when ^{15}N acquisition decoupling is not applied.

For NMR users, it is typically difficult to estimate the upper power limit for NMR probes. A safe approach is to use a pulse sequence that has less frequent ^{15}N pulses but minimizes the contribution to ^{15}N R_2 from antiphase components. This can be achieved by applying ^1H composite decoupling. Because ^1H decoupling reduces generation of the antiphase component, τ_N can be increased, in cases where the chemical exchange contribution is small. Previously, Palmer and colleagues numerically simulated ^{15}N transverse relaxation assuming N_X and $2N_XH_Z$ terms and experimentally found that the error caused by the use of ^1H composite decoupling remained even when the composite decoupling was synchronized to the ^{15}N CPMG pulses (155). Nevertheless, a few reports indicated that ^1H composite decoupling is practical, because it introduces minimal error (202; 157; 201). Thus, whether ^1H composite decoupling can be generally applied to suppress the antiphase effects in the ^{15}N CPMG relaxation is still in question. Another alternative method to minimize the antiphase component is to employ frequent ^1H 180° pulses during a moderately long τ_N period. Although applications of ^1H 180° inversions may saturate water magnetization

(49), ^{1}H saturation occurs even by the use of ^{1}H composite pulses. Thus, use of frequent ^{1}H 180° pulses is expected to yield spectra that are similar to those obtained using ^{1}H composite pulses.

Such employment of frequent ^{1}H pulses may cause sample heating by dielectric or inductive losses particularly in NMR samples containing high salt (52; 76; 100; 72). However, in the experiments with samples containing low salt, ^{1}H pulses may have advantages, compared to more frequent ^{15}N pulses, in reduction of RF coil heating or of perturbation of the lock phase. Pulse sequences with ^{1}H composite decoupling and frequent ^{1}H 180° pulses may often the best approach to determine ^{15}N transverse relaxation rates provided these experiments cause no artifacts. To examine this, we performed simulations and experiments of ^{15}N CPMG transverse relaxation under three primary conditions (**Figure 2.1**): Scheme I, a standard CPMG experiment with frequent ^{15}N CPMG 180° pulses and with infrequent ^{1}H 180° pulses (98); Scheme II, a CPMG experiment with infrequent ^{15}N CPMG 180° pulses in the presence of ^{1}H composite decoupling; Scheme III, a CPMG experiment with infrequent ^{15}N CPMG 180° pulses and frequent ^{1}H 180° pulses. Schemes I and III differ in that generation of the antiphase components was minimized by ^{15}N pulses and ^{1}H pulses, respectively. Although several other alternative methods have been proposed (78; 209), we evaluated only these three basic CPMG pulse schemes.

In our simulations, the time-dependence of ^{15}N magnetization was calculated using the master equation for a two-spin system that accounted for chemical shift and J-coupling evolution, RF pulse effects, and relaxation (6; 7). Our simulation results showed that ^{15}N CPMG relaxation experiments in all the three experiments contained

off-resonance error that are relatively small (< 4% of R_2 values) when ^{15}N signals were within 1 kHz of the carrier frequency (169). ^{15}N relaxation experiments complementary to the simulations were performed using [u-^{15}N, u-^{2}H]- ubiquitin and a 600 MHz NMR instrument equipped with an ambient temperature probe or a 800 MHz instrument equipped with a cryogenic probe. The experimental R_2 values determined using Schemes II and III essentially agreed with those of Scheme I, demonstrating basic consistency with the simulation results. Minor discrepancies were also found between the simulation and experimental results, which was most likely due to multiple sources. ^{15}N relaxation measurements were also carried out with [u-^{15}N]- ubiquitin. With this sample, Scheme II results in observed TOCSY transfer to aliphatic protons, caused by the use of ^{1}H composite decoupling, but provided R_2 values consistent with those recorded using Scheme I. This was presumably because averaging of the two antiphase signals occurred in each unit of the composite pulses, regardless of the absolute intensity of the ^{1}H antiphase components. Overall, the simulations and experiments elucidate the utility of alternative CPMG schemes. Finally, comparison of the three Schemes is summarized.

2.2 METHODS

2.2.1 Simulation

To estimate the magnitudes of the systematic error in ^{15}N CPMG relaxation, we explicitly calculated the time course of magnetization in a scalar-coupled two-spin

system (AX), in which 16 Cartesian product operators in the basis set were prepared as described by Allard et al (7).

$$E/2 \quad N_X \quad N_Y \quad N_Z \quad H_X \quad H_Y \quad H_Z \quad 2N_XH_X$$
$$2N_YH_X \quad 2N_ZH_X \quad 2N_XH_Y \quad 2N_YH_Y \quad 2N_ZH_Y \quad 2N_XH_Z \quad 2N_YH_Z \quad 2N_ZH_Z \qquad (2.1)$$

Six 16×16 matrices (R_1, R_2, … R_6) that assume (i) 90° ^{1}H pulse from phase x, (ii) 90° ^{1}H pulse from phase –x, (iii) 90° ^{15}N pulse from phase x, (iv) both ^{1}H (phase x) and ^{15}N pulse, (v) both ^{1}H (phase -x) and ^{15}N pulse, and (vi) no pulses, respectively, were prepared. In all the matrices, relaxation, chemical shift evolution, and 90 Hz ^{1}H-^{15}N J-coupling effects were included (7). Time dependence of magnetization was calculated by solving each relaxation matrix, R_i, for a given short unit time, t_0, for each of the pulses and/or evolution.

In this calculation, relaxation parameters were assumed with the following parameters: a spectral density function with a single rotational correlation time of 8 ns; ^{1}H resonance frequency, 800.13 MHz; ^{15}N CSA, 170 ppm; N-H distance, 1.02 Å. For the effects of dipolar relaxation from external protons that could not be calculated explicitly due to spin-diffusion effects, arbitrary numbers were assumed: R_1 of external protons, 2 s^{-1}; R_2 of external protons, 20 s^{-1}; a rate of proton spin flip in N_ZH_Z term, 10 s^{-1}. Depending on pulse widths used in each step, t_0 was set to 10, 20, 40, or 50 μs. At the starting of the CPMG relaxation, ^{15}N and ^{1}H magnetizations were assumed to be located at x and z orientation, respectively.

Three types of time courses were simulated: Scheme I, a standard CPMG experiment with frequent ^{15}N CPMG 180° pulses (τ_N = 0.6 ms) and infrequent ^{1}H 180° pulses (τ_H = 2.4 ms); Scheme II, a CPMG experiment with infrequent ^{15}N CPMG 180° pulses (τ_N = 0.6ms, 1.2 ms or 2.4 ms) in the presence of ^{1}H composite ^{1}H decoupling; and Scheme III, a CPMG experiment with infrequent ^{15}N CPMG 180° pulses (τ_N = 2.4 ms) and with frequent ^{1}H 180° pulses (τ_H = 0.6 ms) (**Figure 2.1**). In each type of simulation, ^{15}N CPMG pulses were applied with a 5 kHz B_1 field strength. In Scheme II, composite ^{1}H decoupling sequences, WALTZ-4, WALTZ-8, and WALTZ-16 (177) were employed assuming a 5 kHz B_1 field strength. Lengths of one super-cycle for these composite pulse sequences corresponded to 1.2 ms, 2.4 ms, and 4.8 ms at 5 kHz B_1 field strength, respectively. In Scheme I, the ^{1}H 180° pulses had a 25 kHz B_1 field strength. In Scheme III, three types of ^{1}H 180° pulses were applied: (i) 5 kHz B_1 field strength (50 μs as a 90° pulse width), (ii) 12.5 kHz B_1 field strength (20 μs as a 90° pulse width), or (iii) 11.4 kHz B_1 field strength (22 μs as a 90° pulse width, but applied the duration that corresponds to the 12 .5 kHz B_1 field strength). Note that the pulse width of the 11.4 kHz B_1 field in (iii) was applied for a duration that corresponded to that of the 12.5 kHz B_1 field strength (20 μs as a 90° pulse width) in order to examine the effects of ^{1}H pulse imperfection on ^{15}N transverse relaxation. These delays and pulse widths are summarized in **Table 2.1** (SI to SIII). All the 180° pulses were applied from the x direction unless otherwise noted. All simulations were performed over 134.4ms time course by use of MATLAB software (The Mathworks Inc., Natick, MA).

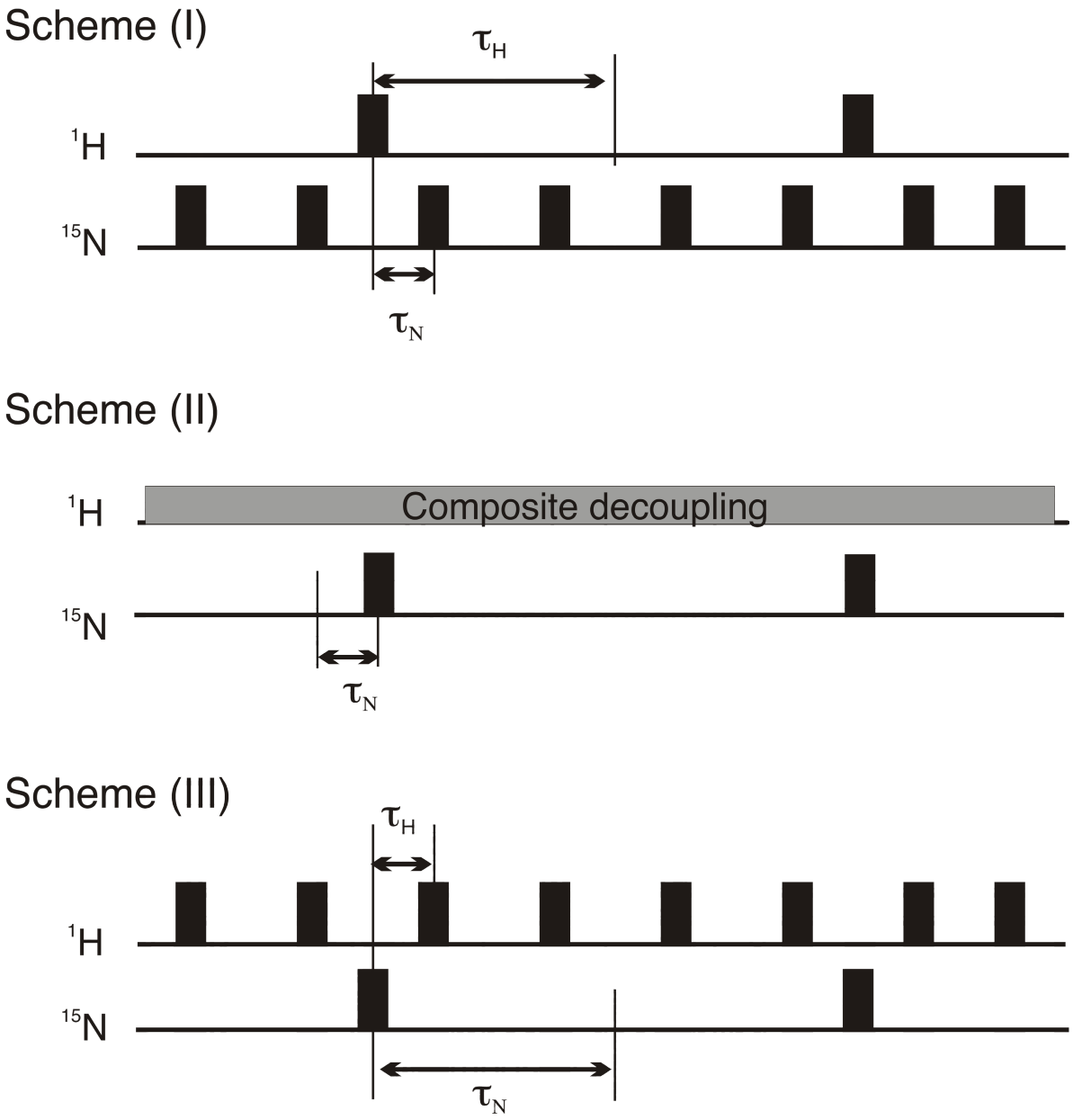

Figure 2.1 Three CPMG pulse trains for application during a relaxation period in the ^{15}N R_2 experiment. Scheme I is a standard ^{15}N CPMG sequence in which the dipolar/CSA cross correlation effect is suppressed by ^{1}H 180° pulses (158; 98; 155). Scheme II is a ^{15}N CPMG sequence with ^{1}H composite decoupling to suppress dipolar/CSA cross correlation and antiphase generation effects. Scheme III is a ^{15}N CPMG sequence with frequent ^{1}H 180° pulses to suppress dipolar/CSA cross correlation and antiphase generation effects. Note in (a) and (c), the relative number of ^{1}H and ^{15}N pulses is reversed.

Table 2.1 Simulation and experiment parameters.

Name Sequence	CPMG	τ_N (ms)	τ_H (ms)	^{1}H Decoupling	^{15}N B_1 (KHz)	^{1}H B_1 (KHz)
Simulation						
SI-1	I	0.6	2.4	—	5	25
SII-1	II	2.4	—	WALTZ4 (×2)	5	5
SII-2	II	2.4	—	WALTZ8 (×1)	5	5
SII-3	II	2.4	—	WALTZ16 (×1/2)	5	5
SII-4	II	1.2	—	WALTZ16 (×1/4)	5	5
SIII-1	III	2.4	0.6	—	5	25
SIII-2	III	2.4	0.6	—	5	12.5
Experiments (^{2}H/^{15}N ubiquitin)						
EI-1	I	0.5	2.0	—	5	20
EII-1	II	1.0	—	WALTZ16	5	5
EII-2	II	2.0	—	WALTZ16	5	5
EII-3	II	1.2	—	WALTZ16 (×1/4)	5	5
EII-4	II	2.4	—	WALTZ16 (×1/2)	5	5
EIII-1	III	2.0	1.0	—	5	20
EIII-2	III	2.0	0.5	—	5	10
Experiments(^{1}H/^{15}N ubiquitin)						
HEI-1	I	0.5	2.5	—	5	20
HEII-2	II	1.2	—	WALTZ16 (×1/4)	5	5

Parenthesis indicates the length of τ_N against one supercycle of the composite pulses. For example, "×1" indicates that one super-cycle of the composite pulse matches to τ_N.

The resultant magnetization decay was fit using a single exponential decay function, $I(t) = I_0 exp(R_2^{sim} t)$. R_2^{sim} values obtained by the simulations were compared with the theoretical R_2 value, R_2^{auto}, using fractional R_2 difference defined in equation (2.2). Here, R_2^{auto} was calculated assuming only auto-relaxation. To evaluate deviation of the magnetization from the theoretical single exponential function, root mean square deviation (rmsd) of the intensity, I^{rmsd}, in each magnetization decay was calculated as described in equation (2.3). Here, I_0 was assumed to be 1.0.

$$R_2^{diff} = (R_2^{sim} - R_2^{auto})/ R_2^{auto} \quad (2.2)$$

$$I^{rmsd} = [\Sigma(I(t)^{sim} - I(t)^{theo})^2/n]^{1/2} \quad (2.3)$$

2.2.2 Experiments

Two proteins samples, 0.8 mM [u-^{15}N, u-^{2}H]- and [u-^{15}N]-ubiquitin (Spectra Stable Isotope), were used in collecting experimental relaxation data. Both samples were dissolved in 95% H_2O/5% $^{2}H_2O$ containing 20 mM acetate buffer at pH 5.0. NMR spectra were recorded at 17 ºC on a Bruker DRX 600 MHz spectrometer operating at a ^{1}H frequency of 600.57 MHz using a triple-resonance ambient-temperature probe with xyz-gradient coil, and on a DRX800 spectrometer operating at a ^{1}H frequency of 800.13 MHz using a triple-resonance cryogenic temperature probe with a shielded z-gradient coil. The [u-^{15}N, u-^{2}H]-ubiquitin (but not and [u-^{15}N]-ubiquitin) contained several extra

sharp residues that do not exist in the native ubiquitin sequence, but these peaks were also included in the analysis.

The ^{15}N transverse relaxation was recorded using a refocused HSQC-based sequence (98) with 16 and 8 accumulations with the 600 MHz and 800 MHz NMR spectrometers, respectively. Transverse relaxation data (**Figure 2.1**) were collected from each of the three Schemes with seven relaxation delays: 0, 16, 32, 48, 64, 80, and 96 ms for Schemes I and III, and 0, 9.6, 19.2, 38.4, 57.6, 76.8, and 96 ms for Scheme II. In all Schemes, ^{15}N CPMG 180° pulses were applied at 5 kHz B_1 field strength. In Scheme I, ^{1}H 180° pulses were applied at 20 kHz B_1 field strength with τ_H = 2.5 ms and τ_N = 0.5ms. In Scheme II, ^{1}H composite pulses were applied at 5 kHz B_1 field strength with τ_N = 1.2 ms or 2.4 ms. In Scheme III, ^{1}H 180° pulses were applied at 20 kHz B_1 field strength with τ_H = 1 ms or at 10 kHz B_1 field strength with τ_H = 0.5 m. In both cases, τ_N = 2.0 ms was used. The ^{15}N and ^{1}H 180° pulses during the CPMG period were applied from x-direction unless otherwise noted. The [u-^{15}N, u-^{2}H] sample was examined for all three Schemes. The [u-^{15}N]-ubiquitin sample was examined using Schemes I and II with WALTZ16. The root-mean-square-deviation (rmsd) of ^{15}N R_2 values and the average difference, $<\delta R_2>$, in the ^{15}N R_2 values determined using Scheme II or III from those determined using Scheme I are described in each graph. Delays and pulse widths are summarized as EI-EIII and HEI-HEII in **Table 2.1**.

To check sample heating, one dimensional proton spectra were recorded after pulsing of ^{15}N (τ_N = 0.5ms and a total duration of 64 ms, repeated with 2s delay for 2 min) using a 99.8% D_2O sample containing 60 mM sodium 3-(trimethylsilyl) propionate-2,2,3,3,-d4 (TSP). The experiment was repeated using the TSP sample containing 50

mM NaCl. Chemical shift difference between the methyl proton signal and water HDO signal was recorded to estimate temperature qualitatively.(70)

2.3 RESULTS AND DISCUSSIONS

2.3.1 Study Aim

The purposes of this study were to identify systematic errors involved in various CPMG experiments (**Figure 2.1**) and to determine a method for measuring accurate ^{15}N transverse relaxation rates without causing probe damage. As described in the introduction, to prevent probe damage in a ^{15}N CPMG experiment, it may be necessary to shorten the total CPMG period or to increase τ_N. The degree of heating during a ^{15}N CPMG experiment varies depending on the specific design on an NMR probe. Therefore, general comments regarding the extent of probe heating can not be made. In particular, coil configurations and sizes depend on the type of probe and its manufacture. In addition to the probe itself, the degree of heating can be influenced by sample salt concentration, for example, if the inductance loss is significant (52; 76; 100; 72).

To examine the degree of heating in our system qualitatively, we measured the changes in the ^{1}H chemical shifts of TSP sample in D_2O resulting from a train of ^{15}N pulses that are equivalent to those used in the CPMG experiments. The experiments were carried out at 800 MHz using a cryogenic probe containing a double tuned $^{2}H/^{15}N$ coil. Although the deuterium lock level changed upon pulsing, the TSP signal did not

exhibit a significant change in temperature, indicating that there must be multiple factors that affect to the deuterium lock level. The experiment that was performed using the TSP sample containing 50 mM NaCl exhibited more significant changes in the deuterium lock level, but did not indicate significant changes in chemical shifts either.

In Schemes II and III, we applied ^{15}N CPMG pulses with a delay time, τ_N, 2-4 times longer (> 1 ms) than those (~ 0.5 ms) used in the traditional method, Scheme I (**Figure 2.1**). Although such an increase in the τ_N period could in theory amplify the chemical exchange contribution to R_2 and lead to a slight extra loss of magnetization by molecular diffusion, we expected that such effects would be minimal if τ_N was increased only by a factor of 2-3. Generally, a significant change in the measured relaxation rate occurs at $4\tau_N k_{ex} \approx 1$ (here, $4\tau_N$ approximately corresponds to the effective field strength, and k_{ex} is an exchange rate). In other time regimes, the measured relaxation rate does not significantly change upon increasing in the τ_N value. At $4\tau_N k_{ex} \approx 1$, chemical exchange contribution to R_2 increases almost linearly as a function of the effective field strength. Thus, if the effective field strength is 500 Hz at τ_N = 0.5 ms, a three-fold increase of τ_N reduces the effective field strength to 167 Hz, and results in an approximately 3-fold increase in the chemical exchange contribution. The magnitude of τ_N used in this study is clearly different from those achieved in Hahn-type experiments. As $1/2J_{NH}$ = 5.4 ms, a significant ^{15}N-^{1}H component is generated once the τ_N increases 2-4 times.

2.3.2 Simulation of ^{15}N transverse relaxation using a standard pulse scheme (Scheme I)

In the first stage of our study, we simulated the time course of ^{15}N transverse magnetization in a standard CPMG experiment (Scheme I in **Table 2.1**) using the spin system described in equation (2.1). The magnetization decay depends on the off-resonance frequency (169; 107). Thus, as shown in **Figure 2.2(a)**, the accuracy of the ^{15}N magnetization decay was evaluated by the difference of the simulated R_2 value and the R_2^{auto} (R_2^{diff}, equation (2.2)) and also evaluated by rmsd of the simulated intensities against the intensities of the auto-relaxation (I^{rmsd}, equation (2.3)). R_2^{auto} calculated assuming an auto-relaxation was 14.2 s^{-1}. The R_2 values obtained from the simulation were the same or slightly smaller than R_2^{auto} because longitudinal relaxation contributed to the simulated rate. As expected, I^{rmsd} and R_2^{diff} increased as a function of off-resonance frequency, with an oscillation frequency of $1/\tau_{CP}$. The off-resonance frequency range that provided a reasonable error (< 4%) was less than 1 kHz in our simulation conditions (B_1 = 5 kHz, τ_{CP} = 0.6 ms). This simulation did not contain any error due to noise. The 3% error was solely due to off-resonance and accompanying relaxation effects.

2.3.3 Simulation of ^{15}N transverse relaxation in the presence of ^{1}H composite decoupling (Scheme II)

Next, the time course of ^{15}N transverse magnetization was calculated in the presence of ^{1}H composite decoupling. The composite pulses of WALTZ sequences were applied as previously examined (155) by the following reasoning: (A) a short unit

of the composite pulse can be accommodated in each τ_N period, and (B) a composite pulse is composed of 0° (including combinations of +90° and -90° pulses) or 180° pulses so that a ^{15}N-^{1}H antiphase component is always flipped up or down. The latter effect was particularly important in our study because net inversion of ^{1}H pulses at each τ_N period serves to cancel the antiphase component. For these reasons, GARP (176) or adiabatic decoupling such as WURST (110) were not applied.

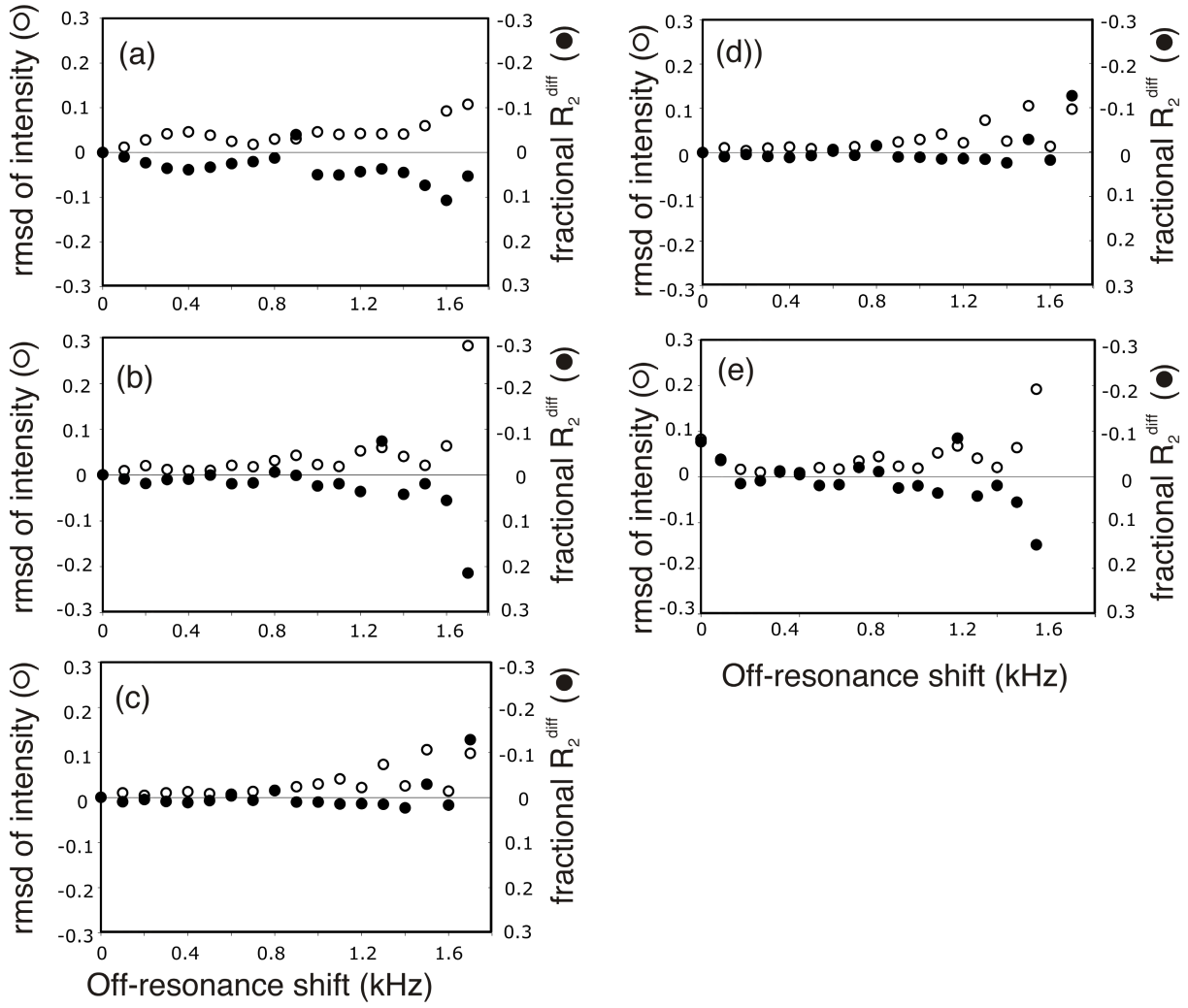

Figure 2.2 Fractional R_2 difference (R_2^{diff}, filled circles) and rmsd of intensities (I^{rmsd}, open circles) calculated for the simulated ^{15}N transverse magnetization decay using (a) Scheme I, (b) Scheme II with WALTZ 4 sequence, (c) Scheme II with WALTZ8 sequence, (d) Scheme II with WALTZ16 sequence (1/2 synchronization), and (e) Scheme

II with WALTZ16 sequence (1/4 synchronization). Detailed conditions are described in Table 1: see lines SI-1 for (a), SII-1 for (b), SII-2 for (c), SII-3 for (d), and SIII-4 for (e).

The ^{15}N magnetization simulated in the presence of WALTZ4 decoupling exhibited smaller fluctuations of R_2 values (R_2^{diff} < 2%) for ^{15}N off-resonance frequencies of < 1 kHz compared to that calculated using Scheme I (**Figure 2.2a and 2.2b**). This was most likely because ^{1}H pulses flipped the signs of small N_ZH_Z components that were generated by off-resonance pulses. Significant increases in R_2^{diff} and I^{rmsd} at > 1 kHz off-resonance frequencies were observed in both Scheme I (**Figure 2.2a**) and Scheme II (WALTZ4) (**Figure 2.2b**), showing the off-resonance error.

Compared to WALTZ4, the WALTZ8 sequence provided similar but more uniform intensities of the ^{15}N transverse magnetization simulated using Scheme II at ^{15}N off-resonance frequency < 1 kHz (**Figure 2.2c**). This difference may be explained by an imperfection in the WALTZ4 super-cycle causing a small-angle rotation about an axis close to the Z axis (177). This explanation is supported by our observation that R_2^{diff} of the simulations using the WALTZ16 was also smaller than that obtained using the WALTZ4 as described below. Almost uniform R_2^{diff} and increased I^{rmsd} as a function of off-resonance frequency (**Figure 2.2c)** indicate that R_2 obtained by the Scheme II simulation using the WALTZ8 sequence had less systematic oscillation at off-resonance frequency than that using WALTZ4.

The profiles of R_2^{diff} and of I^{rmsd} calculated using the WALTZ16 sequence were also similar to those calculated using WALTZ8 (**Figure 2.2d)**. The R_2^{diff} at < 1 kHz off-resonance frequency was less than 1.5%, which was slightly better than the case for Scheme I (**Figure 2.2a)**. In this simulation, τ_N corresponded to 1/2 of the super-cycle of

the WALTZ16. In contrast, abrupt changes in R_2^{diff} when τ_N corresponded to 1/4 of the super-cycle of WALTZ16 (synchronized to an *R* element) were evident (**Figure 2.2e**). Upon counting the time average of ^1H z-magnetization, it was obvious that cancellation of the antiphase component was sufficient when τ_N was set to 1/2 of the WALTZ16 super-cycle but not 1/4. These simulation results were consistent with previous results (155).

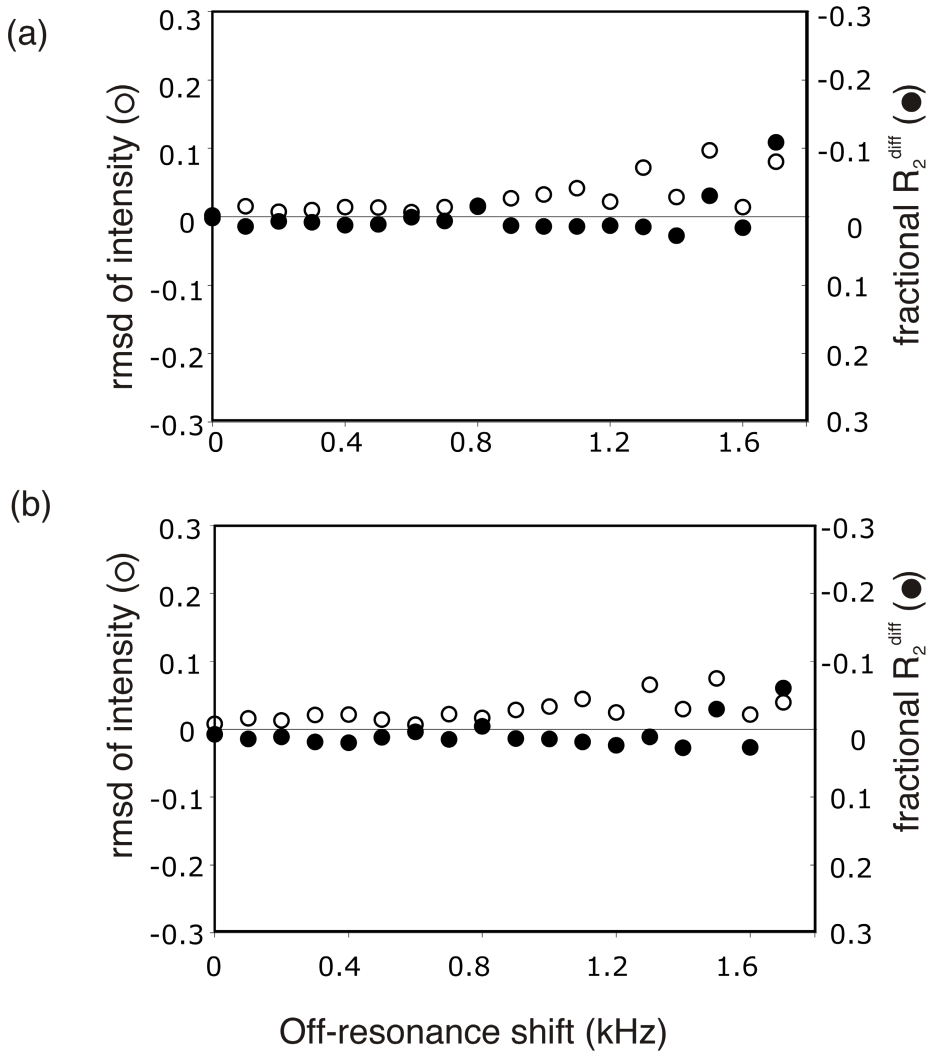

Figure 2.3 Fractional R_2 difference (R_2^{diff}, filled circles) and rmsd of intensities (I^{rmsd}, open circles) for the simulated ^{15}N transverse magnetization decay calculated using Scheme III with ^1H B_1 field strength of (a) 25 kHz

and (b) 11.4 kHz. In (b) simulation, ^{1}H pulses were applied only for the length that corresponded to 12.5 kHz B_1 filed strength. Detailed conditions are described in Table 1: see lines SIII-1 for (a) and SIII-2 for (b).

2.3.4 Simulation of ^{15}N transverse relaxation in the presence of frequent ^{1}H 180° pulses (Scheme III)

Next, we performed simulation using the Scheme III sequence and obtained R_2^{diff} and I^{rmsd} as a function of off-resonance frequency. **Figure 2.3a** clearly shows that use of frequent ^{1}H 180° pulses (at 25 kHz B_1 field strength) resulted in an off-resonance profile of the ^{15}N intensities similar to that of the reference CPMG experiment. The R_2^{diff} was less than 1.6% for off-resonance frequencies < 1 kHz, and therefore smaller than that of Scheme I, which was consistent with the results obtained from the Scheme II simulation. Thus, it is most likely that frequent ^{1}H pulses (either rectangular pulses or composite decoupling pulses) flipped the signs of small N_ZH_Z components that were generated for off-resonance signals, thereby reducing the off-resonance effects.

A two-fold reduction in the ^{1}H pulse strength (12.5 kHz B_1 field strength, 20 μs 90° pulse) did not significantly change the intensity profile (data not shown). In addition, even when the B_1 field strength was further reduced by 10% (11.37 kHz B_1 field strength) and was applied for 20 μs (simulating a miscalibrated 90° pulse), there was no significant difference in the off-resonance profile from that was calculated using 12.5 kHz B_1 field strength at < 1 kHz off-resonance frequency (**Figure 2.3b**). This insensitivity to pulse calibration error was presumably because ^{1}H was not the observed nucleus. A drawback of using frequent ^{1}H pulses is sample heating in high-salt solution

(52; 76; 100; 72). Overall, the use of frequent ^{1}H 180° pulses is expected to be advantageous for low-salt samples.

2.3.5 ^{15}N transverse relaxation experiments recorded using a 600 MHz NMR instrument equipped with an ambient temperature probe.

To complement these simulation results, we performed ^{15}N CPMG transverse relaxation experiments on a 600 MHz NMR spectrometer equipped with an ambient temperature probe using each Scheme (**Table 2.1**) for [u-^{15}N, u-^{2}H]-ubiquitin. Relaxation rates obtained using Schemes II and III, R_2(Schemes II and III), were compared with those obtained using Scheme I, R_2(Scheme I). When τ_N was 1.0 ms, not synchronized to the *R* element of the super cycle of WALTZ16, R_2(Scheme II) values were slightly larger than the R_2(Scheme I) values (**Figure 2.4a**). This systematic increase reduced when τ_N was 2.0 ms (**Figure 2.4b**), probably because the ^{1}H magnetization was more decoupled within one CPMG delay at τ_N = 2.0 ms than at τ_N = 1.0 ms. Nevertheless, overall correlations between R_2(Scheme I) and R_2(Scheme II) were lower than 0.99 (**Figure 2.4b)**. The correlation increased to more than 0.995 when τ_N was synchronized to a one half or one quarter of WALTZ16 supercycle (**Figures 2.4c and 2.4d**). Similarly high correlation of R_2 values (> 0.995) was obtained when Scheme III was compared to Scheme I (**Figures 2.4e and 2.4f**). Overall, except for R_2(Scheme II) at τ_N = 1.0 ms, the rmsds of R_2 values against those from the reference (Scheme I) were less than 0.37 s^{-1}, that is < 5% error.

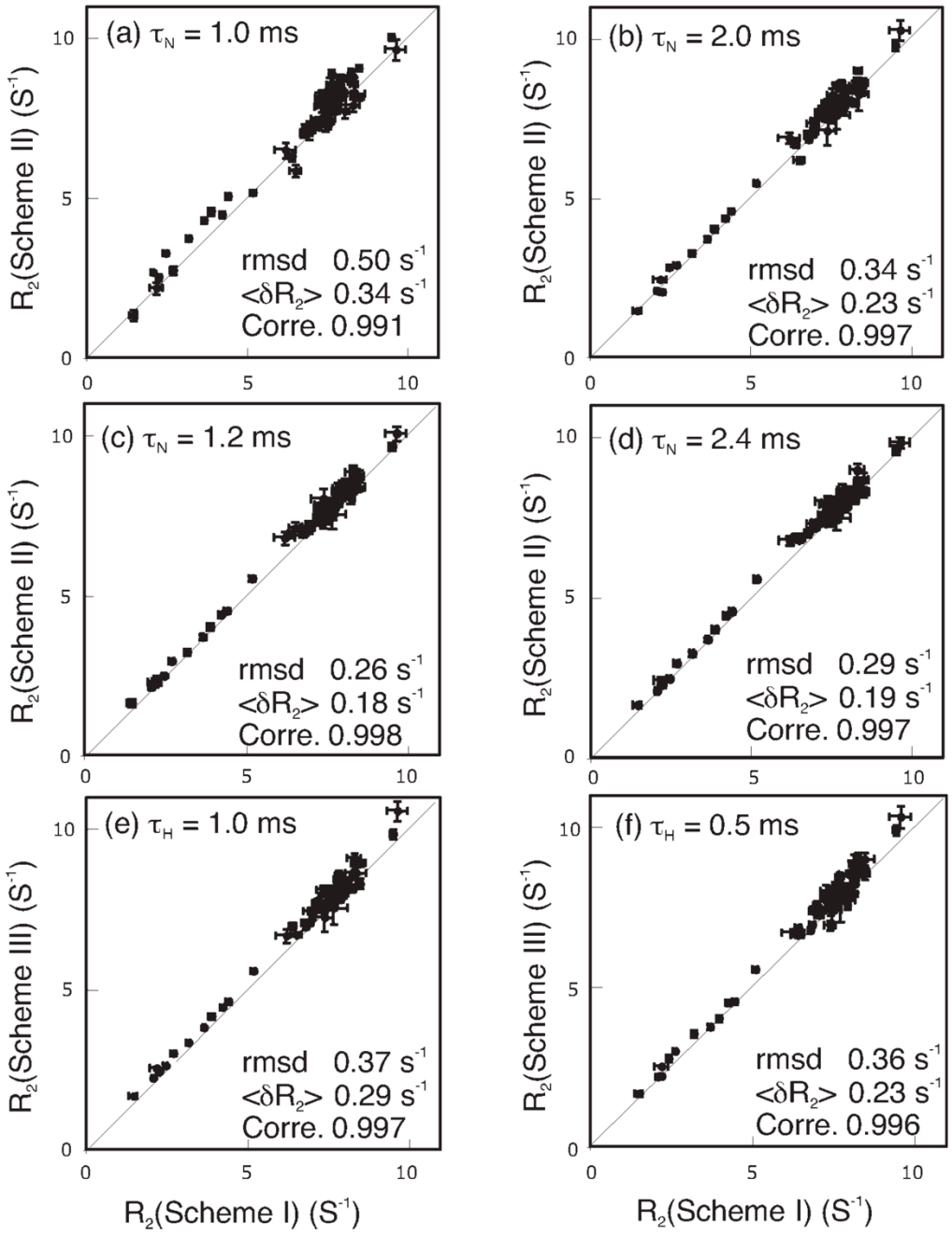

Figure 2.4 Correlation of experimental ^{15}N R_2 values for [u-^{15}N, u-^{2}H]-ubiquitin recorded using a 600 MHz NMR instrument equipped with an ambient temperature probe: (a) Scheme I vs. Scheme II with WALTZ16 and τ_N = 1.0 ms (EII-1 in Table 2.1); (b) Scheme I vs. Scheme II with WALTZ16 and τ_N = 2.0 ms (EII-2 in Table 2.1); (c) Scheme I vs. Scheme II with WALTZ16 and τ_N = 1.2 ms (EII-3 in Table 2.1); (d) Scheme I vs. Scheme II with WALTZ16 and τ_N = 2.4 ms (EII-4 in Table 2.1); (e) Scheme I vs. Scheme III with τ_H = 1.0 ms (EIII-1 in Table 2.1); (f) Scheme I vs. Scheme III with t_H = 0.5 ms (EIII-1 in Table 2.1). One super-cycle of the WALTZ16 was 4.8 ms.

In (a) and (b), the τ_N durations are not synchronized to the WALTZ pulse cycle. In (c) and (d), τ_N durations are synchronized at a 1/2 and 1/4 of the super-cycle, respectively. Each graph shows root-mean-square-deviation (rmsd) of R_2 value, the average difference in the R_2 value, $<\delta R_2>$, and the correlation values.

2.3.6 ^{15}N transverse relaxation experiments recorded using a 800 MHz NMR instrument equipped with a cryogenic probe.

The same sets of experiments were repeated using a 800 MHz instrument equipped with a cryogenic probe. The overall results were similar to those obtained with the 600 MHz spectrometer: some of the R_2(Scheme II) values were significantly different from R_2(Scheme I) values (correlation 0.979) when τ_N was not synchronized to the *R* element of the super cycle of WALTZ16 (τ_N = 1.0 ms) (**Figure 2.5a**). R_2(Scheme II) values at τ_N = 2.0 ms exhibited better correlation to R_2(Scheme I) values (a correlation 0.990). Similar, but not better correlations were observed for R_2(Scheme II) values obtained using a 1/2 or 1/4 synchronized WALTZ sequences (correlation 0.990 and 0.985, respectively, **Figures 2.5c and 2.5d**). R_2(Scheme III) values also provided similar correlation (~0.987) with R_2(Scheme I) values (**Figures 2.5e and 2.5f**). No apparent difference was observed in the signal-to-noise ratios (S/N ca. 400 – 420 for the first 2D spectra). However, the phase of the water was more uniform with frequent ^{1}H 180°pulses than with ^{1}H composite decoupling even at 800 MHz. Because the WALTZ composite pulses used 90° pulses, the orientation of residual water signals may have been more scattered in Scheme II than in Scheme III.

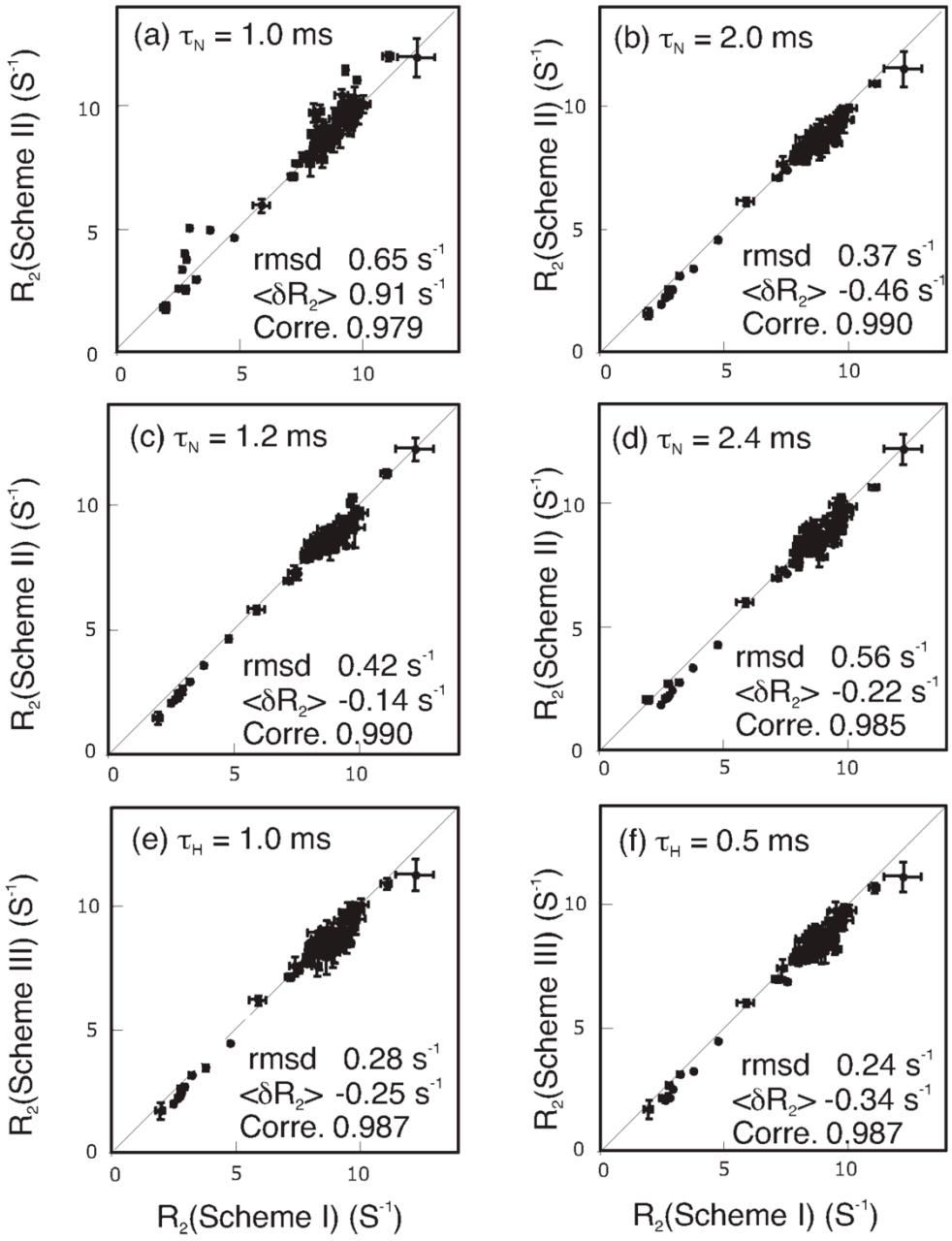

Figure 2.5 Correlation of experimental ^{15}N R_2 values for [u-^{15}N, u-^{2}H]-ubiquitin recorded using a 800 MHz NMR instrument equipped with a cryogenic temperature probe. The same parameters as described in Figure 2.4 were applied.

2.3.7 Comparison of ^{15}N R_2 values recorded with the 600 MHz and 800 MHz instruments

At both 600 MHz and 800 MHz spectrometers, the R_2 values obtained for [u-^{15}N, u-^{2}H]- ubiquitin using Schemes II and III, except for τ_N = 1.0 ms in WALTZ16, exhibited good correlation with those obtained using Scheme I: rmsd differences of these R_2 values (0.4 s^{-1} that corresponds to 5% at R_2 = 8 s^{-1}) were close to the experimental error (ca. 2%). However, at 600 MHz, R_2 values recorded using Schemes II and III were slightly larger than those recorded using Scheme I, showing positive $<\delta R_2>$ values (**Figure 2.4**). A small bias in the opposite direction was observed at 800 MHz, where R_2(Schemes II and III) values were mostly smaller than R_2(Scheme I) values when R_2 < 5 s^{-1}, resulting in negative $<\delta R_2>$ values (**Figure 2.5**).

It is not known which Scheme(s) has (have) a systematic bias. For example, a systematic elevation of R_2(Schemes II and III) values at 600 MHz may be due to contamination of ^{1}H R_1 relaxation by the antiphase term caused by frequent ^{1}H pulses. This idea is supported by the fact that this bias was more significant in the 600 MHz data than the 800 MHz data because proton R_1 values are generally larger at 600 MHz than 800 MHz in deuterated proteins. However, the observed systematic bias in the 600 MHz data did not depend on either the number or the strength of the ^{1}H pulses (**Figures 2.4e and 2.4f**). Furthermore, an ^{1}H R_1 effect cannot explain the reduced R_2(Schemes II and III) values at 800 MHz. On the other hand, the fact that systematic bias was observed in both comparisons between R_2(Scheme I) and R_2(Scheme II), and between R_2(Scheme I) and R_2(Scheme III) at 600 MHz may suggest that the systematic bias exists in R_2(Scheme I) values. Presumably, frequent application of ^{15}N pulses in

Scheme I may have introduced ^{15}N R_1 effects in the observed R_2 values, resulting in reduction of R_2(Scheme I) in the 600 MHz data. Similarly, frequent application of ^{15}N pulses in Scheme I may have caused loss of magnetization by B_1 inhomogeneity, resulting in an increase of R_2(Scheme I) in the 800 MHz data. Overall, based on the observation of opposite systematic biases in 600 MHz and 800 MHz data, the systematic biases likely are due to multiple mechanisms.

2.3.8 ^{15}N transverse relaxation experiments results with [u-^{15}N]-ubiquitin (Scheme II)

The ^{15}N CPMG experiments using Scheme I and II were repeated with [u-^{15}N]-ubiquitin. In the Scheme II experiments, significant TOCSY transfers from amide proton to aliphatic protons were observed (**Figure 2.6a**). These signals in the aliphatic region were not observed in the spectra acquired with Scheme I. The TOCSY transfer was due to Hartmann-Hahn matching during the ^1H composite decoupling. Nevertheless, we found that the R_2 values recorded using ^1H composite decoupling did not significantly differ from the standard CPMG R_2 values (**Figure 2.6b**). Based on orientation changes of ^1H z-magnetization during one composite pulse cycle, TOCSY transfer did not influence the ^{15}N relaxation rates presumably because cancellation of the cross-correlation effects was accomplished within a short composite cycle.

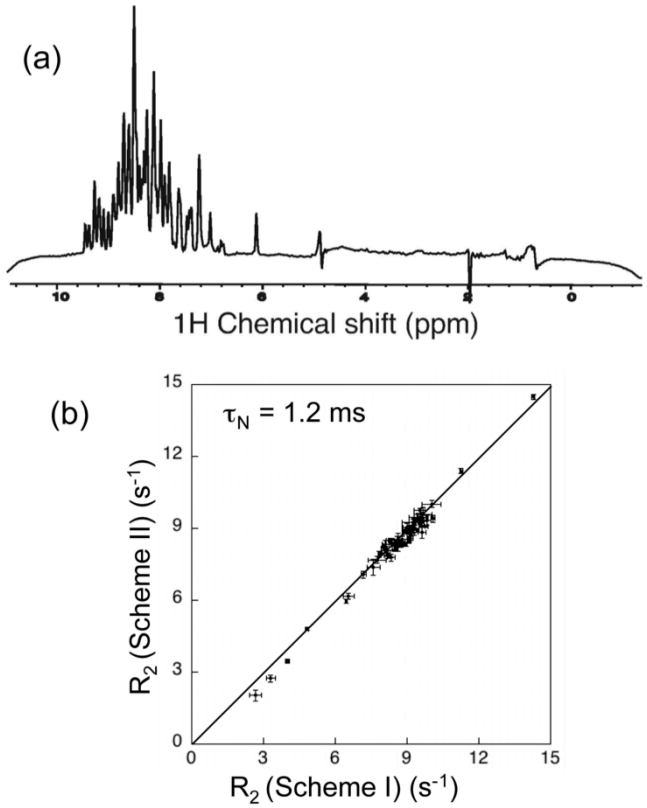

Figure 2.6 (a) One dimensional spectrum of the first t_1 point of ^{15} N transverse relaxation acquired with ^{1}H composite decoupling (Scheme II) during the CPMG relaxation period for [u-^{15}N]-ubiquitin, demonstrating significant TOCSY transfer from amide to aliphatic protons. WALTZ16 (one super-cycle is 4.8 ms) was used such that τ_N was placed at a 1/4 of the supercycle (HEII-2 in Table 2.1). (b) Correlation of the ^{15}N R_2 values acquired in Scheme II with those acquired with the standard ^{15}N CPMG R_2 values (τ_H = 2.5 ms) in Scheme I (HEI-1 in Table 2.1).

2.3.9 Application to the determination of small R_2 values

In this manuscript, the total CPMG delay was set to 96 ms to determine R_2 values varying from 2 to 11 s^{-1}. For an exponential decay function with R_2 = 2 s^{-1}, the optimized CPMG delay is ca. 500 ms. However, a 500 ms CPMG delay is not required to determine R_2 values on the order of 2 s^{-1} with a fractional error similar to those

obtained for R_2 values of 10 s^{-1}. We will discuss below the reason why the fractional errors are similar. Generally, experimental noise is almost uniform in a series of 2D spectra that encode the time course of peak intensities. Assuming uniform noise in a series of spectra, we now consider a two-point exponential fitting that uses two data points at time zero and a certain time, T, to determine a relaxation rate, R. Total error of the relaxation rate, ΔR, is determined by the experimental noise (δ) and a relative ratio of the relaxation time and the data point (RT). As described previously, (87) the fractional error, $\Delta R/R$, in the two-point exponential fitting is described as

$$\Delta R/R = (\delta/I_0)[1+\exp(2\ RT)]^{1/2}/(RT) \qquad (2.4)$$

Here, I_0 is the initial intensity at time zero. According to this equation, when RT=0.25, $\Delta R/R$ will be 2.3 times larger compared to that at RT = 1. Note a simple simulation of a 10-point exponential fitting (in which data points are linearly distributed from 0 to T) shows similar results: when RT= 0.25, $\Delta R/RT$ will be 2.6 times larger than those at RT = 1, respectively. Thus, when RT becomes smaller (at RT < 1), fractional error increases.

Now, this error estimation can be applied to the case of transverse relaxation. Assuming a Lorentzian line shape of observed peaks, the peak height increases 4-fold when R_2 is reduced by a factor of 4. This corresponds to a four-fold reduction of the (δ/I_0) term. Thus, in the exponential fitting in the transverse relaxation, reduction of R_2 decreases (δ/I_0) term but increases $[1+\exp(2\ RT)]^{1/2}/(RT)$ term in equation (2.4). As a result, there is no significant increase in fractional error of R_2.

2.4 CONCLUSIONS

We compared ^{15}N CPMG relaxation rates determined using Scheme I with those determined using Schemes II and III that have a smaller number of ^{15}N CPMG 180° pulses. We tested the relaxation experiments in simulation and experiments using a 96 ms CPMG delay and a 100 μs ^{15}N 180° pulse width. These were conditions under which Scheme I worked safely with our instruments. The number of CPMG pulses may be reduced when a long CPMG delay is used for smaller proteins or unfolded proteins at low protein concentrations to minimize the fitting errors in the determination of R_2 values. However, as described above, one may not need a CPMG delay that corresponds to an exact inverse of the estimated R_2 values. In addition, the number of CPMG pulses may be reduced when shorter ^{15}N 180° pulses, which require high power, are applied to reduce off-resonance errors in R_2 data at a higher static magnetic field strength (169; 107).

Overall, R_2 values determined using Schemes II and III showed good correlation with those determined using Scheme I except for a slight systematic bias stemming from either Schemes II and III or Scheme I itself. Schemes II and III can be useful to reduce the number of ^{15}N CPMG pulses, and therefore reduce possible probe heating. However, since the employment of frequent ^{1}H pulses may cause sample heating by dielectric or inductive losses particularly in high salt NMR samples (52; 76; 100; 72), Scheme I may perform better than Schemes II or III for protein samples in aqueous solution at high ionic strength at very high magnetic field strength. In this case, to minimize the total CPMG duration, one may determine the proper CPMG duration

based on both signal-to-noise ratio and uncertainty caused by an exponential fitting. On the other hand, between Scheme II and III that may perform better than Scheme I for protein samples at low ionic strength to reduce heating, Scheme III has an advantage of uniform water phase than Scheme II. From an experimental view point, Scheme III has also more flexibility in setting τ_N values than Scheme II, because there is no need to synchronize a τ_N period to a supercycle of ^1H composite pulses.

3.0 CHEMICAL EXCHANGE EFFECTS DURING REFOCUSING PULSES IN CONSTANT-TIME CPMG RELAXATION DISPERSION EXPERIMENTS

In the analysis of the constant-time Carr-Purcell-Meiboom-Gill (CT-CPMG) relaxation dispersion experiment, chemical exchange parameters, such as rate of exchange and population of the exchanging species, are typically optimized using equations that predict experimental relaxation rates recorded as a function of effective field strength. In this process, the effect of chemical exchange during the CPMG pulses is typically assumed to be the same as during the free-precession. This approximation may introduce systematic errors into the analysis of data because the number of CPMG pulses is incremented during the constant-time relaxation period, and the total pulse duration therefore varies as a function of the effective field strength. In order to estimate the size of such errors, we simulate the time-dependence of magnetization during the entire constant time period, explicitly taking into account the effect of the CPMG pulses on the spin relaxation rate. We show that in general the difference in the relaxation dispersion profile calculated using a practical pulse width from that calculated using an extremely short pulse width is small, but under certain circumstances can exceed 1 s^{-1}. The difference increases significantly when CPMG pulses are miscalibrated. The results presented in this chapter have been published in *Journal of*

Biomolecular NMR, 2009, 45:207-216. In this chapter, my main contributions were for the whole chapter.

3.1 INTRODUCTION

Conformational exchange among two or more environments with distinct chemical shifts occurring on the milli-microsecond time scale can be detected based on the constant-time Carr-Purcell-Meiboom-Gill (CT-CPMG) relaxation dispersion experiment. This method has been applied to characterize biologically important processes such as protein folding and enzyme kinetics, which involve local conformational fluctuations (120; 191; 200; 134; 179; 190; 15; 37; 195; 18; 105; 108; 112; 187; 119; 67). In the CT-CPMG relaxation dispersion experiment, the nuclear spin transverse relaxation rate, R_2, is measured as a function of the effective field strength, ν_{CP}, that is related to the half-duration between CPMG pulses, τ_{CPMG}, according to $\tau_{CPMG} = 1/(4\nu_{CP})$. The total relaxation period (T_{CP}) for transverse relaxation is fixed while ν_{CP} is increased by the decreasing τ_{CPMG}. Chemical exchange parameters, such as the exchange rate, populations of the exchanging species, and difference in off-resonance frequencies between the exchanging species, are optimized by fitting the experimental R_2 dispersion profile using a two-site exchange or a multiple-site exchange equation.

The equation that is applied to optimize the parameters is either a numerical solution of Bloch-McConnell equation or its approximate analytical solution (130; 123; 25). In both approaches, the calculations typically neglect effects of chemical exchange during CPMG pulses (i.e. the calculations assume free precession, except for an

instantaneous 180° rotation, during each CPMG pulse) (**Figure 3.1**). Although some studies take into account effects associated with off-resonance frequency (169; 87), the impact of neglecting the effect of the finite CPMG pulse duration on the calculated R_2 values is not known. Since the total duration of the CPMG pulses varies as a function of ν_{CP}, the total CPMG pulse duration ranges from as little as 0.45% up to 18% of the entire T_{CP} in typical ^{15}N CT-CPMG dispersion experiments (180° degree pulse, τ_{180} = 90 μs; ν_{CP} = 25 ~1000 Hz). Therefore, it is possible that the free-precession approximation during the pulse duration may introduce systematic error in the analysis of dispersion profiles.

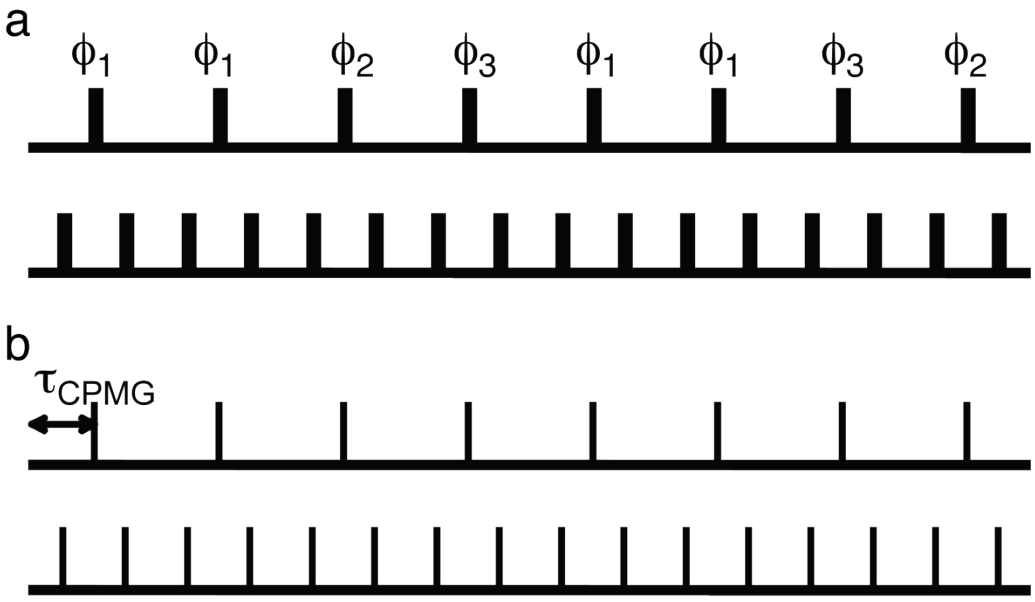

Figure 3.1 Pulse schemes of the CT-CPMG relaxation experiments that are compared in this study: (a) includes pulse widths (wide bars) and (b) neglects pulse widths (lines). The CPMG pulse sequence utilizes the pulse phases $\phi_1 = \phi_2 = \phi_3$ = X (131) while an alternative sequence utilizes pulse phases of ϕ_1 = X, ϕ_2 = Y, ϕ_3 = -Y (209; 118). In the following, these pulse schemes are denoted as the $[00000000]^{\pm}$ and the $[00130031]^{\pm}$ schemes, respectively. Entire phase cycles that were employed to calculate magnetization intensities in the following simulations are described in the Methods section.

The aim of this study is to determine whether the assumptions used in the analysis of ^{15}N CT-CPMG relaxation dispersion data with regards to the negligible width of pulses results in systematic error in the estimation of the chemical exchange parameters. For this purpose, the time-dependence of magnetization during the CT-CPMG period is calculated using the master equation for a two-state system, which accounts for chemical shift, radio-frequency pulse effects, relaxation, and chemical exchange (6; 7; 139). To determine the extent of systematic errors due to chemical exchange during CPMG pulses, the R_2 rates obtained with and without significant pulse widths, as illustrated in **Figure 3.1**, are compared. Simulations are also performed using an alternative pulse scheme that was initially developed to reduce off-resonance effects on R_2 by Zuiderweg's group and subsequently applied for relaxation dispersion experiments by Yang's group (209; 118), to determine whether systematic error exists in this alternative pulse sequence.

3.2 METHODS

3.2.1 Master Equation

The time evolution of bulk nuclear magnetization exchanging between two conformational sites, A and B, was calculated to determine the effect of pulse duration on the CT-CPMG relaxation dispersion experiment. The magnetization was

represented by a state vector in which 7 Cartesian product operators were prepared as described previously (7)

$$\sigma(t) = \left[E/2 \quad M_X^A \quad M_Y^A \quad M_Z^A \quad M_X^B \quad M_Y^B \quad M_Z^B \right]^T \tag{3.1}$$

with the $M_\gamma^{A/B}$ being the projection of the bulk magnetization vector of the site A or B along the γ = X, Y, or Z axis. The state vector is similar to the one used in the Bloch-McConnell equation (130) but includes a unity term E/2 that corresponds to the correction for equilibrium magnetization. The time evolution of σ(t) through the pulse sequence was calculated by solving the master equation

$$\sigma(t + \Delta t) = Exp(R \cdot \Delta t) \cdot \sigma(t) \tag{3.2}$$

with the relaxation matrix, **R**, and an initial condition $\sigma(0)$ given by

$$R = -\begin{bmatrix} 0 & 0 & 0 & 0 & 0 & 0 & 0 \\ 0 & R_2^{0A} + k_{AB} & \Omega_A & \omega_Y^{B1} & -k_{BA} & 0 & 0 \\ 0 & -\Omega_A & R_2^{0A} + k_{AB} & -\omega_X^{B1} & 0 & -k_{BA} & 0 \\ -2R_1^{0A} M_{Z0}^A & -\omega_Y^{B1} & \omega_X^{B1} & R_1^{0A} + k_{AB} & 0 & 0 & -k_{BA} \\ 0 & -k_{AB} & 0 & 0 & R_2^{0B} + k_{BA} & \Omega_B & \omega_Y^{B1} \\ 0 & 0 & -k_{AB} & 0 & -\Omega_B & R_2^{0B} + k_{BA} & -\omega_X^{B1} \\ -2R_1^{0B} M_{Z0}^B & 0 & 0 & -k_{AB} & -\omega_Y^{B1} & \omega_X^{B1} & R_1^{0B} + k_{BA} \end{bmatrix} \tag{3.3}$$

$$\sigma(0) = \left[1/2 \quad p_A \quad 0 \quad 0 \quad p_B \quad 0 \quad 0 \right]^T \tag{3.4}$$

R accounts for: the resonance frequencies of the two exchanging sites, Ω_A and Ω_B; the radio-frequency field, B_1, from the Y or X axis, ω_X^{B1} or ω_Y^{B1}; the intrinsic longitudinal relaxation rates for sites A and B, R_1^{A0} and R_1^{B0}, respectively; the intrinsic transverse relaxation rates for sites A and B, R_2^{A0} and R_2^{B0}, respectively; and the exchange rates

from site A to site B, and from site B to site A, k_{AB} and k_{BA}, respectively. The $M_{Z0}^{A/B}$ is the equilibrium magnetization along the Z-axis for site A or B. The ω_X^{B1} and ω_Y^{B1} are related to the duration of an ideal 180° pulse width, τ_{180}, by the relation $\omega_{X/Y}^{B1} = \pi / \tau_{180}$. The fractional populations of sites A and B are given by p_A and p_B, respectively, with $p_A + p_B = 1$. The exchange rate, k_{ex}, is given by $k_{ex} = k_{AB}/p_B = k_{BA}/p_A$. The difference in chemical shifts, $(\delta\omega)/2\pi$, is defined by $(\Omega_A - \Omega_B)/2\pi$. The equation used here is different from the relaxation matrix that is often used for the optimization of chemical exchange parameters in CT-CPMG dispersion experiments in which longitudinal magnetization terms and effects of pulse duration are not taken into account (104). Calculations were performed using the MATLAB software (The Mathworks Inc., Natick, MA).

3.2.2 Schemes for the CT-CPMG simulation

Simulations were conducted using the original CPMG pulse sequence in the following manner (denoted as a $[00000000]^{\pm}$ scheme). Transverse magnetization was generated initially along the X-axis as given by $\sigma(0)$, and the CPMG pulses were applied along the X-axis. Next, magnetization was again generated along the X-axis, and the CPMG pulses were applied along the -X-axis. The average of the magnetization intensities calculated these two ways at time T_{CP}, $M^i_X(T_{CP})$, was then used to calculate R_2 value according to

$$R_2^i = \ln\left(M_X^i(0) / M_X^i(T_{CP})\right) / T_{CP} \qquad (3.5)$$

Here, i = A or B site. R_2 values for individual sites were calculated in the slow exchange case. The summation of A and B site magnetization was used for the calculation of R_2

in the fast exchange case. The superscript *i* to indicate site *i* is neglected to simplify the description hereafter. Superscript *i* in the intrinsic relaxation rates is also neglected hereafter by using conditions of $R_1^{A0} = R_1^{B0} = R_1^0$ and $R_2^{A0} = R_2^{B0} = R_2^0$. This condition will avoid additional systematic errors caused by differences in the intrinsic relaxation rates of the two sites (85).

Simulations were also conducted using an alternative sequence that was proposed previously (209; 118)(denoted as $[00130031]^{\pm}$). In this scheme, transverse magnetization was generated along the X-axis, and the 180º pulses were applied along the X, X, Y, -Y, X, X, -Y, Y axes with a minimum eight pulses in one cycle. Magnetization intensity after T_{CP} was stored in the memory. Next, magnetization was again generated in the X-axis, and the 180º pulses were applied from the -X, -X, -Y, Y, -X, -X, Y, -Y axes with a minimum eight pulses in one cycle. Transverse magnetization at time T_{CP}, $M_X(T_{CP})$, was calculated as the average of the two magnetization intensities. Apparent relaxation rates for the $[00130031]^{\pm}$ scheme, R_{Alt}, were determined by equation (3.5), and corrected using equation (3.6) to yield R_2 values for R_2 dispersion plot (118):

$$R_2 = R_{Alt} + \frac{(R_2^0 - R_1^0)\,\tau_{180}}{8\,\tau_{CPMG}} \qquad (3.6)$$

When there is no chemical exchange (i.e., $R_2 = R_2^0$), the equation (3.6) is identical to that proposed by Zuiderweg for general transverse relaxation experiments (209).

3.2.3 Parameters applied for CT-CPMG simulations

The following three sets of R_2 dispersion profiles were generated in this study using the $[00000000]^{\pm}$ and $[00130031]^{\pm}$ schemes described above. In all the simulations, R_1^0 and R_2^0 were set equal to 1.86 s^{-1} and 10.84 s^{-1}, respectively. This corresponds to amide nitrogens in a protein with a rotational correlation time of 7 ns at 60.8 MHz ^{15}N resonance frequency. Fractional populations, p_A and p_B, were set equal to 0.8 and 0.2, respectively. R_2 values were calculated for pulse sequences of T_{CP} = 40 ms and ν_{CP} ranging from 100 Hz to 3000 Hz, with R_2 values calculated for every ν_{CP} = 100 Hz. Pulse width for CPMG was assumed to be either τ_{180} = 90 μs or 2 ns in all the simulations as described below.

The first set of R_2 dispersion profiles was calculated without any chemical exchange to determine the effects of off-resonance errors quantitatively. The simulations were conducted assuming accurate CPMG pulses that rotate on-resonance magnetization by 180º. The simulations were repeated assuming that the CPMG pulses were applied at a 20% lower B_1 field strength (that corresponds to 144º rotation of on-resonance magnetization). R_2 dispersion profiles were calculated for the resonances that are located at 0, 200 Hz, 400 Hz, and 800 Hz off-resonance from the carrier.

The second set of simulations was calculated allowing chemical exchange using the following parameters: (a) $k_{ex} = 5 \times 10^3$ s^{-1} and $\delta\omega/2\pi$ = 150 Hz; (b) $k_{ex} = 20 \times 10^3$ s^{-1} and $\delta\omega/2\pi$ = 300 Hz; (c) k_{ex} = 100 s^{-1} and $\delta\omega/2\pi$ = 500 Hz; (d) k_{ex} = 100 s^{-1} and $\delta\omega/2\pi$ = 1500 Hz. Here, (a) and (b) satisfy the fast exchange condition ($k_{ex} >> \delta\omega/2\pi$), and (c)

and (d) satisfy the slow exchange condition (k_{ex} << $\delta\omega/2\pi$). Accurate 180º pulses were assumed in the simulations, and site A was set at the on-resonance frequency.

The third set of simulations was calculated allowing chemical exchange assuming the CPMG pulses at 20% lower and 20% higher B_1 field strengths (corresponding to 144º and 216º rotations, respectively). In these simulations, following parameters were used: k_{ex} = 20 × 10^3 s^{-1} and $\delta\omega/2\pi$ = 300 Hz, and k_{ex} = 100 s^{-1} and $\delta\omega/2\pi$ = 1500 Hz, which correspond to (b) and (d) in the above paragraph, respectively.

In the first and the second sets of simulations, R_2 dispersion profiles for the $[00000000]^{\pm}$ scheme were also calculated using an extremely short pulse width, τ_{180} = 2 ns, to obtain an ideal CPMG R_2 profile. Additionally, $R_{1\rho}$ values were calculated as a function of the radio-frequency field, B_{SL} (=$\omega_{SL}/2\pi$), using the Palmer and Massi's equation 31 (156):

$$R_{1\rho} = R_1^{\,0}\cos^2\theta + R_2^{\,0}\sin^2\theta + \frac{p_A p_B \delta\omega^2 k_{ex}\omega_{SL}^2/\omega_e^2}{\omega_{eA}^2\omega_{eB}^2/\omega_e^2 + k_{ex}^2 - 2p_A p_B\delta\omega^2\gamma\omega_{SL}^2/\omega_e^2 + (1-\gamma)\omega_{SL}^2} \quad (3.7)$$

With

$$\gamma = 1 + p_A p_B \delta\omega^2\left(\frac{(p_A\Omega_B + p_B\Omega_A)^2 + \omega_{SL}^2 - k_{ex}^2}{\left((p_A\Omega_B + p_B\Omega_A)^2 + \omega_{SL}^2 + k_{ex}^2\right)^2}\right); \overline{\Omega} = p_A\Omega_A + p_B\Omega_B;$$

$\theta = \arctan\left(\omega_{SL}/\overline{\Omega}\right)$; $\omega_e = \left(\overline{\Omega}^2 + \gamma\omega_{SL}^2\right)^{1/2}$; and $\omega_{ei} = \left(\Omega_i^2 + \gamma\omega_{SL}^2\right)^{1/2}$ (with i = A, B for effective field at site A or site B).

To evaluate differences of the calculated R_2 profiles from the ideal CPMG R_2 profile, the calculated R_2 profiles were fit by using the Bloch-McConnell equation with

instantaneous 180° rotation (**Figure 3.1b**). In the fitting, k_{ex} and p_A were optimized while R_2^0 and $\delta\omega/2\pi$ were fixed. The optimizations of the parameters were verified by grid searches to minimize ΔR_2 that was defined as r. m. s. d. between the calculated and the fit R_2 profiles. The uncertainties of the optimized parameters were given as the ranges in which $\Delta R_2 < 0.5$ s^{-1}. Since the simulations were conducted in the skewed population case (p_A:p_B = 0.8:0.2), the calculated R_2 profiles were plotted only for site A in slow exchange and for the weighted average magnetization in fast exchange.

3.3 RESULTS AND DISCUSSION

3.3.1 CPMG Simulations in the absence of chemical exchange

The aim of this study is to identify systematic error caused by the chemical exchange effects during pulses in the CT-CPMG R_2 dispersion experiments. Prior to conducting this research, we calculated time dependence of magnetization by solving equation (3.2) and determined R_2 based on equation (3.5) to quantitatively estimate off-resonance effects in the R_2 dispersion profile in the absence of chemical exchange (169). When the simulation was conducted by applying CPMG pulses at 5.56 kHz B_1 field strength (90 μs as 180º pulses), the observed R_2 values differed from the intrinsic relaxation rate, R_2^0, by up to 2%, 4%, and 7% at 200 Hz, 400 Hz, and 800 Hz off-resonance frequencies, respectively (**Figure 3.2a**). However, these differences were still less than 1 s^{-1}. Off-resonance error was further reduced when the alternative

CPMG experiment (209; 118) ([00130031]$^{\pm}$ scheme) was applied. The maximum deviation of R_2 values from R_2^0 was less than 1% even at 800 Hz off-resonance frequency, providing uniform inversion over a significantly wider band width than the [00000000]$^{\pm}$ scheme (**Figure 3.2c**).

We also simulated an extreme case when 144º pulses were applied instead of 180º rotation pulses for CPMG (20% miscalibration of the B_1 field strength). Although R_2 differed from R_2^0 by more than 5 s^{-1} at 800 Hz off-resonance frequency, the difference was less than 2 s^{-1} at < 400 Hz off-resonance frequency (**Figure 3.2b**). Such large difference of R_2 values from R_2^0 was not observed using the [00130031]$^{\pm}$ scheme, even when 144º pulse rotations were applied instead of 180º rotations (**Figure 3.2d**). However, the calculated R_2 values were systematically ca. 1 s^{-1} smaller than R_2^0. This is because imperfect signal inversion pulse produces significant Z-magnetization that remains during the free-precession period between the pulses and results in contamination of R_1 component in the observed R_2 (see section 3.3.3). Although the effect of R_1 during the pulses in [00130031]$^{\pm}$ scheme is taken into account in the calculation of R_2 values from R_{Alt} in equation (3.6), the effect of R_1 during free precession caused by the pulse imperfection remains.

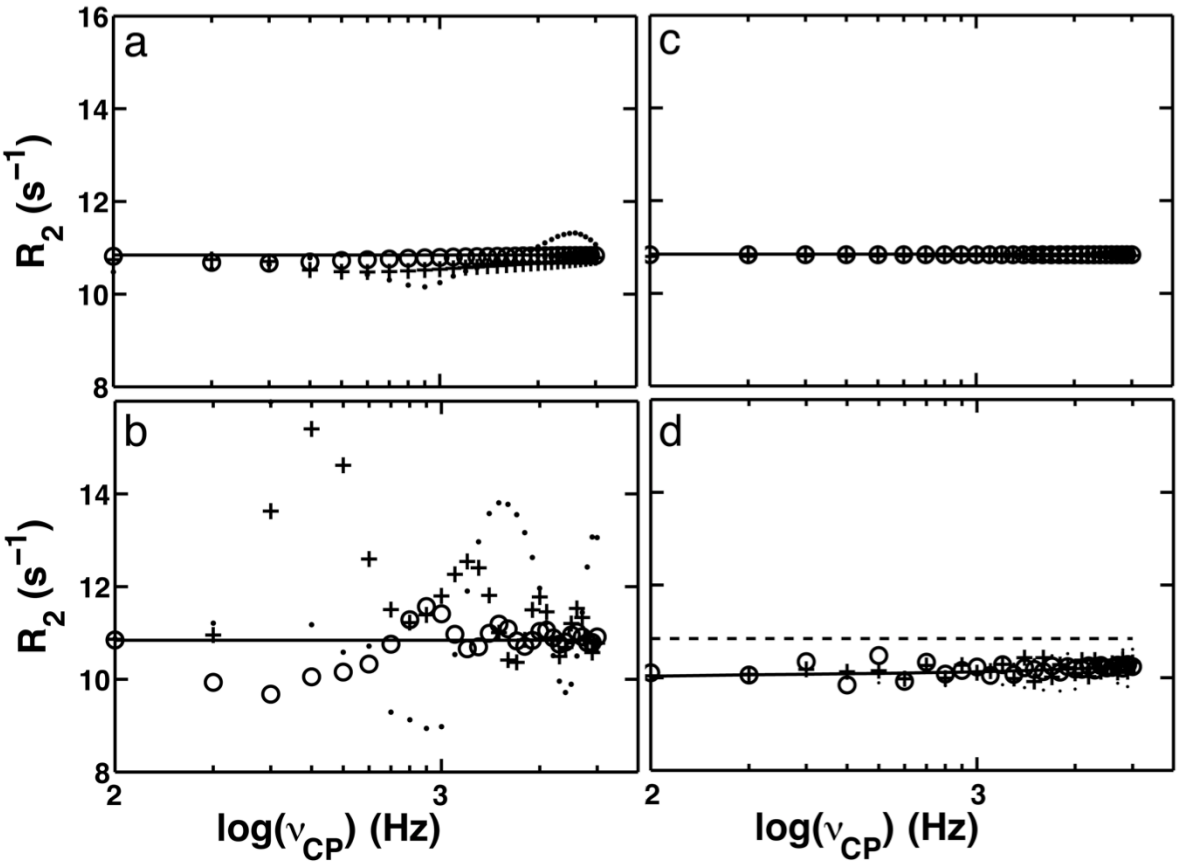

Figure 3.2 R_2 values calculated as a function of effective field strength, ν_{CP}, in the absence of chemical exchange for (a, b) $[00000000]^{\pm}$ and (c, d) $[00130031]^{\pm}$ schemes. Figures in (a) and (c) were calculated using ideal 180º rotation pulses, while Figures in (b) and (d) were calculated using 144º pulses instead of the 180º rotation pulses (assuming -20% B_1 miscalibration). In each figure, solid line (-), circles (○), crosses (+), and dots (•) indicate R_2 values calculated at 0, 200 Hz, 400 Hz, and 800 Hz from the radio-frequency carrier, respectively. In (a)-(c), the solid lines are consistent with the intrinsic transverse relaxation rate, R_2^0, used in the simulation. In (d), the solid line (i.e., R_2 at the carrier frequency) is significantly different from the R_2^0 that is shown by the dashed line (--). All the simulations were conducted using the following parameters: $\tau_{180} = 90$ μs, $R_1^0 = 1.86$ s^{-1}, and $R_2^0 = 10.84$ s^{-1}.

Overall, the above simulations in the absence of chemical exchange demonstrate that the off-resonance error is less than 1 s^{-1} at < 400 Hz off-resonance frequency when 180º pulse rotation is applied, and is less than 2 s^{-1} at < 200 Hz off-resonance

frequency even when 144º pulse rotation is applied. The errors are similar in magnitude to experimental noise in NMR experiments. Thus, in the following simulations, we assumed a two-site exchange with site A at the carrier frequency in both slow and fast exchange cases. In the fast exchange simulation, $\delta\omega/2\pi$ was set to be either 150 or 300 Hz so that the weighted average resonance was located at 60 or 100 Hz, respectively. Such a narrow region was used to minimize off-resonance effect and to allow thereby the determination of systematic error caused by chemical exchange occurring during pulsing.

3.3.2 Effect of an additional 180º phase cycle on the calculation of CPMG R_2 dispersion profiles.

In the CPMG experiments, 180° (X and -X) phase cycle (i.e., averaging of intensities that are calculated using the $[00000000]^+$ and the $[00000000]^-$ schemes) is applied to reduce the off-resonance error because magnetization intensity that travels through the +Z axis during a 180° pulse with one phase is increased by R_1 relaxation while magnetization that travels through the -Z axis during a 180° pulse by the other phase is decreased by the same R_1 process. Thus, this 180° phase cycle was included in all the simulations conducted in the manuscript. In this paragraph, to demonstrate errors that are introduced if the 180° phase cycle is not included, relaxation dispersion profiles in the absence of the 180° phase cycle are shown for magnetization that are located at +500 Hz and -500 Hz off resonance frequencies (**Figure 3.3a**). These simulations were conducted by employing the $[00000000]^+$ scheme in the absence of chemical exchange using τ_{180} = 90 μs and T_{cp} = 40 ms. Influence by the R_1 process was

confirmed by simulating the R_2 profiles assuming $R_1^0 = R_2^0 = 10.84\ s^{-1}$, in which more amplified modulation of the R_2 values were observed (**Figure 3.3b**).

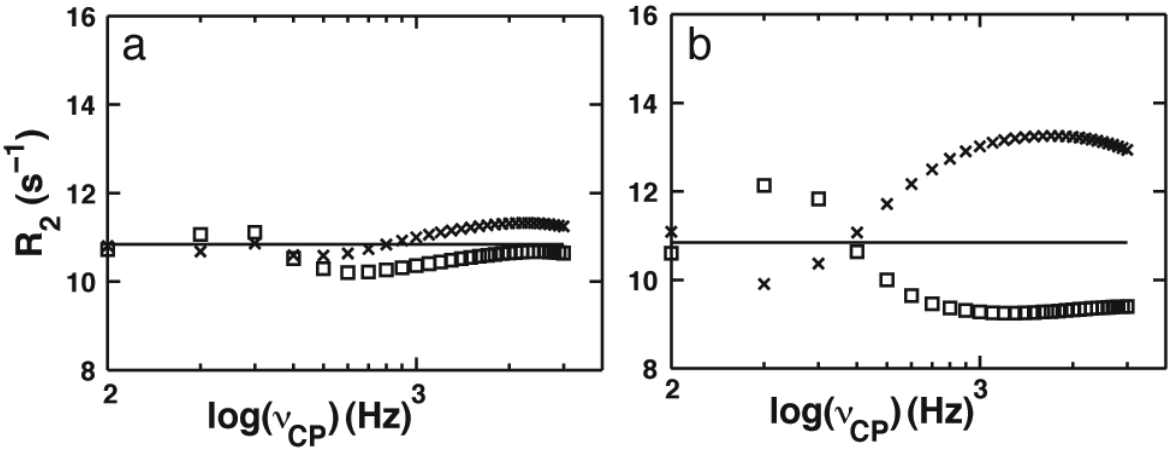

Figure 3.3 R_2 profile calculated as a function of effective field strength, ν_{CP}, in the absence of chemical exchange at (a) $R_1^0 = 1.86\ s^{-1}$ and $R_2^0 = 10.84\ s^{-1}$ and at (b) $R_1^0 = R_2^0 = 10.84\ s^{-1}$. In each graph, □ and × indicates data points calculated assuming, +500 Hz and -500 Hz off-resonance frequency, respectively. The R_2 profile calculated with the magnetization at the carrier frequency is shown as a line. All the R_2 values shown in these figures were calculated using the $[0000000]^{\pm}$ scheme without X and -X phase cycle.

3.3.3 Effect of R_1 on the calculation of R_2 dispersion profiles using the $[00130031]^{\pm}$ scheme

When 144º pulses were applied instead of 180º inversion pulses for CPMG, the R_2 values calculated using the $[00130031]^{\pm}$ scheme were systematically ca. 1 s^{-1} smaller than R_2^0 even in the absence of chemical exchange (**Figure 3.2d**). To determine the cause of the systematic reduction, an additional calculation of the R_2 dispersion profile was conducted with $R_1^0 = R_2^0$ while keeping other exchange parameters the same as those employed to generate the dispersion profile in **Figure 3.2d**. The calculated profile, **Figure 3.4a**, shows no significant systematic reduction of the R_2 values, indicating that

the reduction was due to the Z-magnetization that remained during the free-precession period. More direct evidence was obtained by calculating the time course of the Z-magnetization using the $[00130031]^{\pm}$ scheme (**Figure 3.4b**) at ν_{CP} = 1 kHz for a signal at the carrier frequency. The time course demonstrates significant residence of the Z-magnetization between the third and fourth pulses of the (X, X, Y, -Y) or (X, X, -Y, Y) cycle.

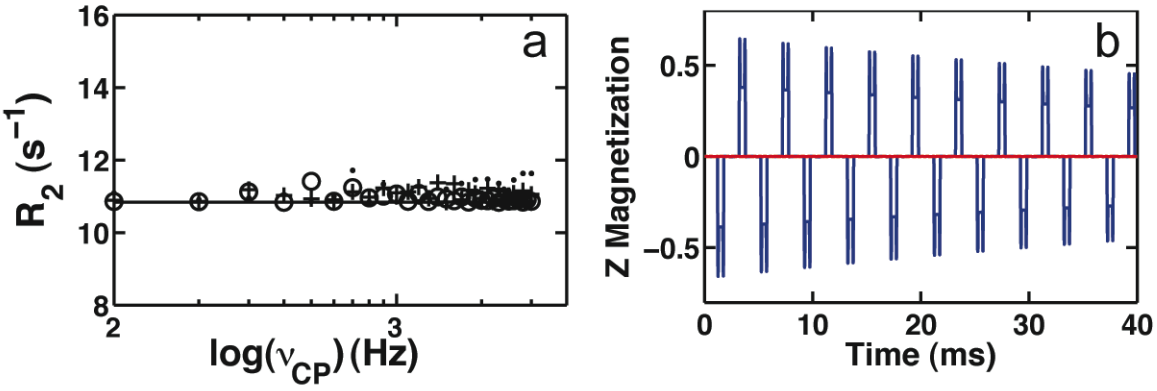

Figure 3.4 (a) R_2 profile and (b) a time course of the Z-magnetization calculated using the $[00130031]^{\pm}$ scheme (blue) with 144º rotation pulses instead of the 180º rotation pulses. Both simulations were conducted in the absence of chemical exchange. In (a), $R_1^0 = R_2^0 = 10.84\ s^{-1}$, and a solid line (-), circles (○), crosses (+), and dots (•) indicate R_2 values calculated at 0, 200 Hz, 400 Hz, and 800 Hz from the radio-frequency carrier, respectively. In (b), intensity at the carrier frequency was calculated in the following parameters: ν_{CP} = 1000 Hz, $R_2^0 = 10.84\ s^{-1}$, and $R_1^0 = 1.86\ s^{-1}$. The spikes before and after the high Z intensity are effects of pulsing.

3.3.4 Effects on pulse width in the $[00000000]^{\pm}$ scheme

Based on the above results associated with the off-resonance effects, we simulated CPMG R_2 dispersion profiles assuming a two-site exchange with sites A (p_A = 0.8, $\omega_A/2\pi$ = 0 Hz) and B (p_B = 0.2, $\omega_B/2\pi$ = 150 Hz) in the fast exchange condition, k_{ex} =

5×10^3 s^{-1} and $\delta\omega/2\pi$ = 150 Hz. To obtain R_2 dispersion profile, we generated time-dependent magnetization by solving equation (3.2), with the chemical exchange term given by equation (3.3). R_2 was calculated from the final magnetization intensities using equation (3.5) at each effective field. To identify effects of chemical exchange during pulsing, the simulation was conducted twice: first with a practical pulse width, τ_{180} = 90 μs, and second with an extremely short pulse width for an ideal case, τ_{180} = 2 ns. The R_2 dispersion profiles obtained by these simulations were almost identical to each other: the discrepancy in R_2 was ca. < 0.5 s^{-1} even at ν_{CP} = 3 kHz, indicating there is no systematic error caused by the pulse width (**Figure 3.5a**).

Simulation of the R_2 dispersion profile was also conducted in another exchange condition in which k_{ex} is much larger than that described above, k_{ex} = 20×10^3 s^{-1} and $\delta\omega/2\pi$ = 300 Hz (**Figure 3.5b**). Compared with **Figure 3.5a**, the R_2 dispersion profile at larger k_{ex} (**Figure 3.5b**) is shifted towards higher ν_{CP} values, with significant R_{ex} remaining at high ν_{CP} that is recorded after frequent CPMG pulses. In this case, R_2 calculated using τ_{180} = 90 μs exhibited small but significant difference from the CPMG R_2 values calculated using τ_{90} = 2 ns: discrepancy between the R_2 values at ν_{CP} = 1 kHz was ca. 0.5 s^{-1}, and that at ν_{CP} = 3 kHz was ca. 1.5 s^{-1} (6% reduction in R_2). Comparison of the R_2 dispersion profile with the relaxation rates calculated using a spin-lock demonstrate that the R_2 values calculated using τ_{180} = 90 μs approach a spin lock profile at increasing ν_{CP} (**Figure 3.5b**). This is because the fraction of the magnetization that remains along the X-axis under the applied radio-frequency field strength increases as ν_{CP} increases. When the R_2 profile simulated using τ_{180} = 90 μs was fit using the Bloch-McConnell equation with instantaneous 180° rotation (and the fixed R_2^0 = 10.84 s^{-}

[1] and $\delta\omega/2\pi$ = 300 Hz), p_A and k_{ex} were optimized to be 0.765 $\pm$ 0.005 and 22.5 $\pm$ 0.5 $\times$ 10^3 s^{-1}, respectively. These values correspond to changes of 0.035 and 2.5 $\times$ 10^3 s^{-1} from those originally used (0.80 and 20 $\times$ 10^3 s^{-1}) to generate the profile, respectively.

We next simulated CPMG R_2 dispersion profiles in slow exchange, k_{ex} = 100 s^{-1} and $\delta\omega/2\pi$ = 500 Hz, assuming a two-site exchange with site A (p_A = 0.8, $\omega_A/2\pi$ = 0 Hz) and B (p_B = 0.2, $\omega_B/2\pi$ = 500 Hz). The R_2 dispersion profile simulated using τ_{180} = 90 μs did not exhibit significant discrepancy from the ideal CPMG R_2 values (simulated using τ_{180} = 2 ns) (**Figure 3.5c**).

Even when the R_2 dispersion profile was calculated using a larger $\delta\omega/2\pi$ value, 1500 Hz, at k_{ex} = 100 s^{-1}, no significant discrepancy was obtained (**Figure 3.5d**). As described above, this is also because chemical exchange contribution in R_2 becomes small (< 5 s^{-1}) at large ν_{CP} (> 1 kHz). Since an increase in $\delta\omega/2\pi$ increases the R_2 values at large ν_{CP}, systematic errors caused by chemical exchange during the pulses may become significant when $\delta\omega/2\pi$ exceeds 1500 Hz. However, such large $\delta\omega/2\pi$ values are expected to be rare in the spectra of diamagnetic proteins. Similarly, an R_2 dispersion profile calculated using a pulse width longer than τ_{180} = 90 μs amplifies systematic error caused by the chemical exchange (see section 3.3.6).

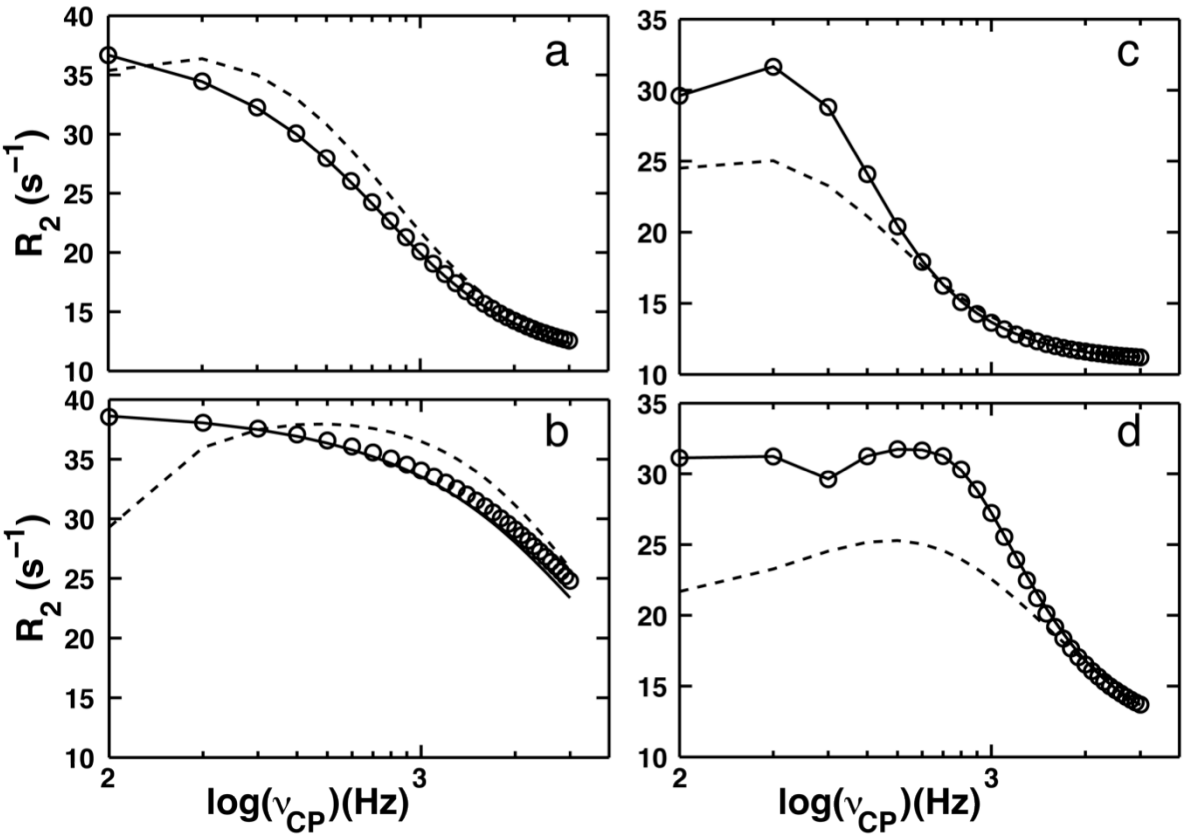

Figure 3.5 R_2 dispersion profiles calculated in the presence of chemical exchange for (a, b) fast exchange and (c, d) slow exchange, using the $[00000000]^{\pm}$ scheme. In each figure, circles (○) and line (-) indicate R_2 profile calculated using a practical 180º pulse width (τ_{180} = 90 μs) and the ideal CPMG R_2 profile calculated without significant pulse duration (τ_{180} = 2 ns), respectively. Both of these profiles were generated assuming two-site exchange with p_A = 0.8, p_B = 0.2, R_1^0 =1.86 s^{-1}, and R_2^0 = 10.84 s^{-1}, and with site A at the carrier frequency. Other parameters were: (a) k_{ex} = 5 × 10^3 s^{-1} and $\delta\omega/2\pi$ = 150 Hz; (b) k_{ex} = 20 × 10^3 s^{-1} and $\delta\omega/2\pi$ = 300 Hz; (c) k_{ex} = 100 s^{-1} and $\delta\omega/2\pi$ = 500 Hz; (d) k_{ex} = 100 s^{-1} and $\delta\omega/2\pi$ = 1500 Hz. For comparison, relaxation rates in the rotating frame (spin-lock condition) were also plotted as a function of ν_{CP} (assuming $\nu_{CP} = B_{SL}$) by the dashed line.

3.3.5 Effects on pulse width in the $[00130031]^{\pm}$ scheme

Using the same chemical exchange parameters as those applied to generate **Figure 3.5b** (k_{ex} = 20 × 10^3 s^{-1} and $\delta\omega/2\pi$ = 300 Hz) and **Figure 3.5d** (k_{ex} = 100 s^{-1} and

$\delta\omega/2\pi$ = 1500 Hz), R_2 dispersion profiles were simulated using the [00130031]$^{\pm}$ scheme by solving equation (3.2) (**Figures 3.6a and 3.6b**, respectively). The apparent relaxation rate, R_{Alt}, was determined from the final magnetization intensities using equation (3.5), and finally R_2 value was calculated using equation (3.6) at each effective field.

R_2 dispersion profiles simulated using the [00130031]$^{\pm}$ scheme were almost the same as the ideal CPMG R_2 profiles calculated using the [00000000]$^{\pm}$ scheme with τ_{180} = 2 ns (**Figures 3.6a and 3.6b**). Especially, it is noteworthy that the dispersion profile calculated using the [00130031]$^{\pm}$ scheme does not approach the calculated $R_{1\rho}$ at increasing ν_{CP}. The agreement of the dispersion profile calculated using τ_{180} = 90 μs to the ideal CPMG R_2 profiles calculated using the τ_{180} = 2 ns can be explained by the assumptions used in the correction equation (3.6) for the [00130031]$^{\pm}$ scheme. By defining a duration for free precession as $2\tau_{FP} = 2\tau_{CPMG} - \tau_{180}$, the correction equation for the time average of R_{Alt} for the four echo periods of the [0013] phase cycle (X, X, Y, -Y) is recast as,

$$8\tau_{CPMG}R_{Alt} = 8\tau_{FP}R_2 + (3R_2 + R_1^0)\tau_{180} + (R_2 - R_2^0)\tau_{180}$$
$$= 8\tau_{FP}R_2 + (3R_2^0 + R_1^0)\tau_{180} + 4R_{ex}\tau_{180} \qquad (3.8)$$

Here, $R_2 = R_2^0 + R_{ex}$. Equation (3.8) indicates that chemical exchange is described by a unique R_{ex} term even during the pulse duration (the third term) as well as the free precession period. Thus, the dispersion profile is "reconstructed" using R_1^0, R_2^0, and R_{Alt} in equation (3.6) such that chemical exchange during pulsing is assumed to be the same as that in free-precession. Based on equation (3.8), the correction equation (3.6) is not sufficient to describe R_{Alt} that is calculated using a practical pulse

width. However, significant error was not observed in R_2 calculated using the [00130031]$^{\pm}$ scheme in **Figure 3.6**. This insignificance of the error is most likely due to cancellation of the increase in R_{ex} during X pulses by the decrease in R_{ex} during Y or -Y pulses. In addition, when R_2 is used instead of R_2^0 in equation (3.6), resultant R_2 is overestimated. A question remains of how R_2^0 values can be measured accurately. Methods have been proposed to yield R_2^0 from the measurements of auto-relaxation rates (56), cross-correlated relaxation values (200) or a combination of longitudinal, single, and double quantum coherence relaxation values (66). However, these approaches require many additional measurements.

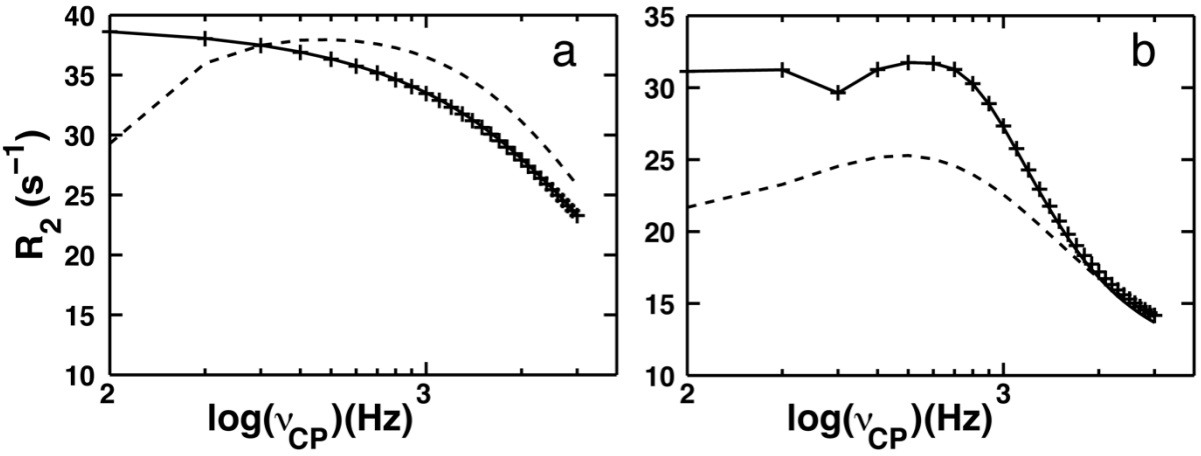

Figure 3.6 R_2 dispersion profiles calculated in the presence of chemical exchange for (a) fast exchange and (b) slow exchange using the (+) [00130031]$^{\pm}$ scheme. The same values of the parameters used in Figures 3.5b and 3.5d were employed to generate the profiles in figures (a) and (b), respectively. In each figure, solid line indicates the ideal CPMG R_2 profile calculated using the [00000000]$^{\pm}$ scheme with τ_{180} = 2 ns, and the dashed line indicates relaxation rates in the rotating frame (spin-lock condition).

3.3.6 Effects of chemical exchange during pulsing when a long pulse is employed for CPMG R_2 dispersion

To verify the effects of chemical exchange during pulsing, CPMG R_2 profile was calculated assuming the pulse width of τ_{180} = 120 μs, instead of 90 μs. In the R_2 profile calculated using the $[00000000]^{\pm}$ scheme in fast exchange (indicated by ○ in **Figure S3a**), elevation of R_2 values, due to spin-lock effect, became significant at high ν_{CP} (> 1 kHz), because of the increase in the fraction of τ_{180} versus τ_{CPMG}. In contrast, the R_2 profile calculated using the $[00130031]^{\pm}$ scheme (indicated by +) was almost identical to the ideal CPMG R_2 profile, as discussed in the text in the main manuscript (**Figure S3a**). In slow exchange, the dispersion profiles calculated assuming the pulse width of τ_{180} = 120 μs did not exhibit significant difference from that of the ideal CPMG R_2 profile (**Figure S3b**). These results support interpretation of the data presented in **Figures 3 and 4** in the manuscript.

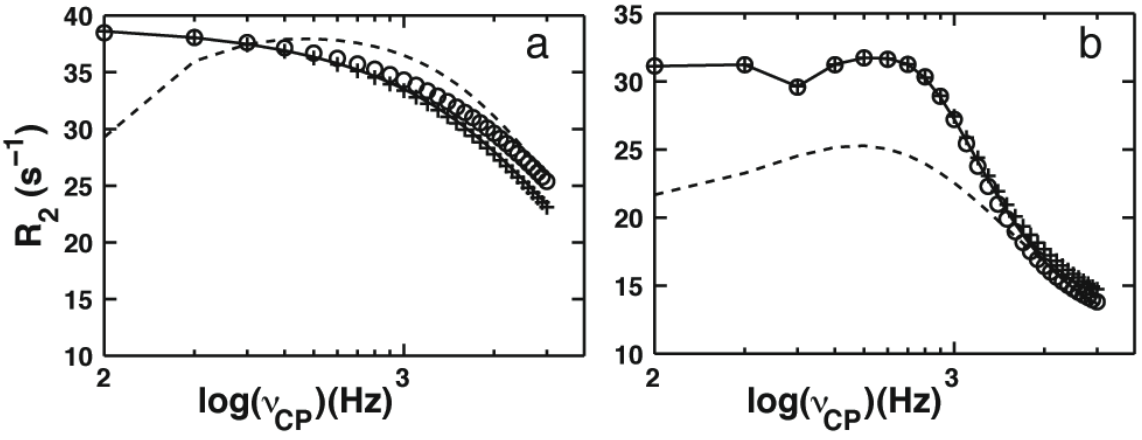

Figure 3.7 R_2 dispersion profiles calculated with τ_{180} = 120 μs for (a) the fast exchange (k_{ex} = 20 × 10^3 s^{-1} and $\delta\omega/2\pi$ = 300 Hz) and (b) the slow exchange (k_{ex} = 100 s^{-1} and $\delta\omega/2\pi$ = 1500 Hz). Except for the pulse width, the same sets of the parameters generate Figures 3.5b and 3.6a for (a), and Figures 3.5d and 3.6b for (b) were applied. In each

figure, ○ and + indicate R_2 values calculated using the $[00000000]^{\pm}$ and the $[00130031]^{\pm}$ schemes, respectively. Line indicates the ideal CPMG R_2 values calculated using the $[00000000]^{\pm}$ scheme with an extremely short pulse width (τ_{180} = 2 ns), and dashed line indicates relaxation rates calculated for spin-lock.

3.3.7 Effects on pulse width in the case of large pulse miscalibration

To estimate the magnitude of systematic errors that are introduced by miscalibration of the 180º pulse, R_2 dispersion profiles were also calculated using 144º and 216º pulses, representing -20% and +20% errors in the B_1 field strength. In the fast exchange (equivalent to that used in **Figure 3.5b**, k_{ex} = 20 × 10^3 s^{-1} and $\delta\omega/2\pi$ = 300 Hz) using the $[00000000]^{\pm}$ scheme, R_2 dispersion profile generated for τ_{180} = 90 μs at 20% lower B_1 field strength (shown by ○ in **Figure 3.8a**) showed larger values than the ideal CPMG R_2 values (by the solid line in **Figure 3.8a** assuming the correct 180º rotation and τ_{180} = 2 ns). This difference in R_2 values was more significant than that in **Figure 3.5b** because of the 20% weaker B_1 field strength. When this R_2 profile (shown by ○ in **Figure 3.8a**) was fit using the Bloch-McConnell equation with instantaneous 180° rotation (with the fixed k_{ex} = 20 × 10^3 s^{-1} and $\delta\omega/2\pi$ = 300 Hz), p_A and k_{ex} were optimized to be 0.635 ± 0.015 and 28.9 ± 0.6 × 10^3 s^{-1}, respectively (corresponding to the 0.165 and 8.9 × 10^3 s^{-1} differences from the values used to generate the profile, 0.8 and 20 × 10^3 s^{-1}). At +20% higher B_1 field strength, the R_2 dispersion profile generated using the $[00000000]^{\pm}$ scheme (shown by ○ in **Figure 3.8b**) was similar to that at -20% higher B_1 field strength but approached the spin-lock values of the +20% higher B_1 field strength.

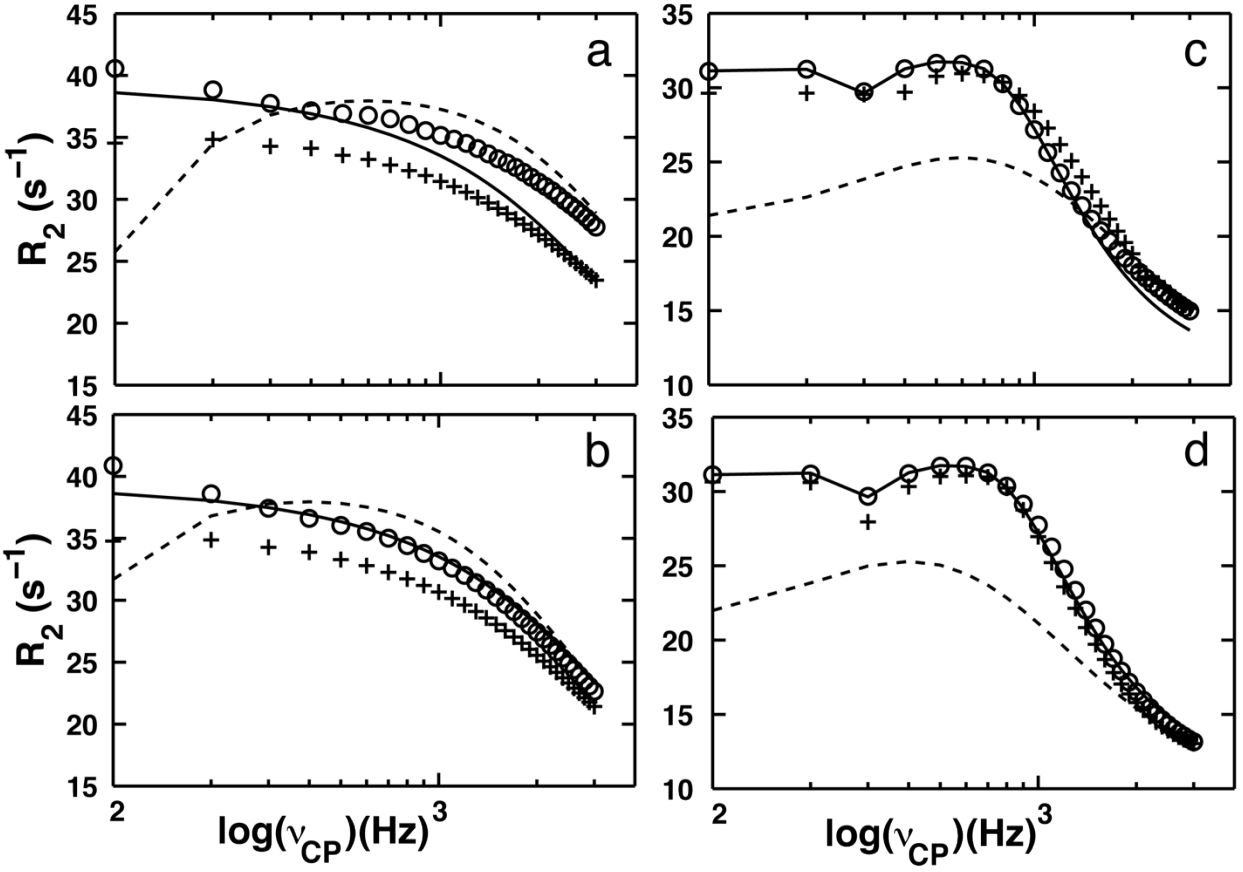

Figure 3.8 R_2 dispersion profiles calculated for (a, b) fast exchange and (c, d) slow exchange by employing (a, c) 144º pulses (-20% B_1 miscalibration) or (b, d) 216º pulses (+20% B_1 miscalibration). In each figure, circles (○), and crosses (+) indicate R_2 values calculated using the $[00000000]^{\pm}$ and $[00130031]^{\pm}$ schemes, respectively. Other parameter values used for the simulations for the (a, b) fast exchange and (c, d) slow exchange were the same as those employed to generate the profiles in Figures 3.3b and 3.3d, respectively. In each figure, an ideal CPMG R_2 profile calculated with extremely short pulse duration using the $[00000000]^{\pm}$ scheme is shown by the solid line, and the profile calculated using the spin-lock condition at (a, c) -20% lower or (b, d) +20% higher B_1 field strength is shown by the dashed line.

In the slow exchange (k_{ex} = 100 s^{-1} and $\delta\omega/2\pi$ = 1500 Hz, which are equivalent to those in **Figure 3.5d**) using the $[00000000]^{\pm}$ scheme, R_2 dispersion profiles generated for τ_{180} = 90 μs at 20% lower or higher B_1 field strength (shown by ○ in **Figures 3.8c** or

3.8d, respectively) were almost identical to the ideal CPMG R_2 profile calculated using the correct B_1 field strength for τ_{180} = 2 ns. This is because the A site magnetization is located at on-resonance along the X-axis, and is not affected by the pulse effects. However, at higher ν_{CP} (> 1 kHz), the R_2 profiles generated at 20% lower/higher B_1 field strength start to have discrepancy from the ideal CPMG R_2 profile and approach the spin-lock profile.

In contrast to the profiles calculated using the $[00000000]^{\pm}$ scheme, R_2 dispersion profiles calculated using the $[00130031]^{\pm}$ scheme for fast exchange at -20% and +20% errors in the B_1 field strength (described by + in **Figures 3.8a** and **3.8b**, respectively) mostly exhibited smaller R_2 values than those of the ideal CPMG R_2 profile calculated using the $[00000000]^{\pm}$ scheme at τ_{180} = 2 ns (described by solid lines in **Figures 3.8a** and **3.8b**). Discrepancy in R_2 value calculated using the using the $[00130031]^{\pm}$ scheme at 20% weaker/stronger B_1 field strength from that of the ideal CPMG R_2 profile was ca. 4 s^{-1} at ν_{CP} = 100 Hz in **Figures 3.8a** and **3.8b**, and was significantly larger than that observed in the absence of chemical exchange in **Figure 3.2d**. This is because equation (3.6) does not include the effects of the residual Z-magnetization during the free-precession period (as shown in section 3.3.3). When the R_2 profile calculated with 20% weaker B_1 field in (indicated by + in **Figure 3.8a**) was fit using the Bloch-McConnell equation for the $[00000000]^{\pm}$ scheme with instantaneous 180° rotation at a correct B_1 field strength (and the fixed k_{ex} = 20 $\times$ 10^3 s^{-1} and $\delta\omega/2\pi$ = 300 Hz), p_A and k_{ex} were optimized to be 0.794 ± 0.007 and 23.4 ± 0.8 $\times$ 10^3 s^{-1} (0.006 and 3.4 $\times$ 10^3 s^{-1} changes from those originally used to generate the profiles, 0.80 and 20 $\times$ 10^3 s^{-1}, respectively).

R_2 dispersion profiles were calculated for slow exchange assuming -20% and +20% errors in the B_1 field strength using the $[00130031]^{\pm}$ scheme (described by + in **Figures 3.8c and 3.8d**, respectively). Other simulation conditions for these were the same as those applied to calculate the profiles shown in **Figure 3.5d.** In both -20% and +20% B_1 error cases, most of the R_2 profiles were slightly smaller that the ideal CPMG R_2 profile calculated using the correct B_1 field strength for τ_{180} = 2 ns. (described by the solid line in **Figures 3.8c** and **3.8d**). The discrepancy was almost equivalent to that observed in the profile calculated without chemical exchange in **Figure 3.2d**. At high ν_{CP} > 1 kHz, the R_2 values approaches the spin-lock profile (**Figure 3.8c**). For these slow exchange profiles calculated using miscalibrated pulses, optimized parameters using the Bloch-McConnell equation with instantaneous 180° rotation are not shown because they were not fit satisfactorily ($\Delta R_2 > 0.5\ s^{-1}$).

3.3.8 Effects of chemical exchange during pulsing when site A is not located at the carrier frequency

To generate **Figures 3.5** to **3.8**, simulations were conducted with the carrier frequency for site A, $\Omega_A/2\pi$ = 0, to minimize off-resonance error. In this paragraph, R_2 profiles calculated at $\Omega_A/2\pi$ = 400 Hz are shown to clarify whether they become similar to those at $\Omega_A/2\pi$ = 0. Although the R_2 profile calculated using the $[00000000]^{\pm}$ scheme at $\Omega_A/2\pi$ = 400 Hz shows additional increase in R_2 at ν_{CP} = 300 Hz in **Figure 3.9a**, overall R_2 profile for the fast exchange was almost identical to that in **Figure 3.5b**. Other

R_2 profiles calculated using either the [00000000]$^{\pm}$ or [00130031]$^{\pm}$ scheme in **Figure 3.9** were also almost identical to those shown in **Figures 3.5** and **3.6**.

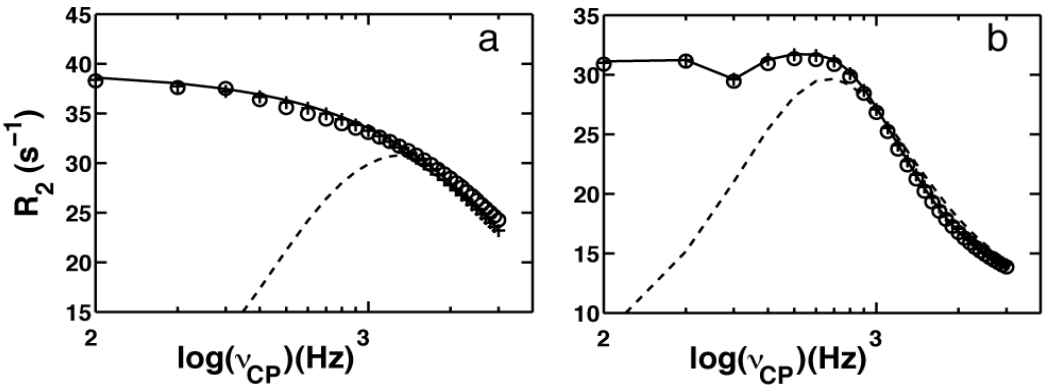

Figure 3.9 R_2 dispersion profiles for site A (p_A = 0.8) at 400 Hz off-resonance frequency in (a) fast exchange ($\Omega_A/2\pi$ = 400 Hz, $\Omega_B/2\pi$ = 700 Hz, and k_{ex} = 20 × 10^3 s^{-1}) and (b) slow exchange ($\Omega_A/2\pi$ = 400 Hz, $\Omega_B/2\pi$ = -1100 Hz, and k_{ex} = 100 s^{-1}) conditions. R_2 profiles were calculated using the (○) [00000000]$^{\pm}$ and the (+) [00130031]$^{\pm}$ schemes with pulse width of τ_{180} = 90 μs. Solid line indicates the ideal CPMG R_2 profiles calculated using the [00000000]$^{\pm}$ scheme with an extremely short pulse width (τ_{180} = 2 ns), and dashed lines indicate relaxation rates calculated in the spin-lock condition.

3.3.9 Effects of pulse width in the case of pulse miscalibration

In this section, R_2 dispersion profiles that were calculated assuming -10% (**Figure 3.10a** and **3.10c**) and +10% (**Figure 3.10b** and **3.10d**) error in the B_1 field strength are shown. R_2 profile calculated using the [00000000]$^{\pm}$ scheme for fast exchange at -10% B_1 field strength (shown by ○ in **Figure 3.10a**) was fit using the Bloch-McConnell equation without pulse duration, with the optimized p_A = 0.707 ± 0.038 and k_{ex} = 26.05 ± 2.55 × 10^3 s^{-1} (0.093 and 6.05 × 10^3 s^{-1}changes, respectively). R_2 profile calculated using the [00130031]$^{\pm}$ scheme for fast exchange at 10% higher or

lower the B_1 field strength was overall ca. 1 s^{-1} smaller than the ideal *CPMG* R_2 profile (**Figures 3.10a and 3.10b**). This R_2 profile at the 10% weaker B_1 field strength (shown by + in **Figure 3.10a**) could be fit using the Bloch-McConnell equation with only one variable parameter, k_{ex}, that was optimized to 20.68 ± 0.70 × 10^3 s^{-1} (0.68 × 10^3 s^{-1} increase). These changes in the optimized parameters for the $[00130031]^{\pm}$ scheme shown here are small, but are more pronounced at higher R_2^0 values, such as for proteins with large molecular mass.

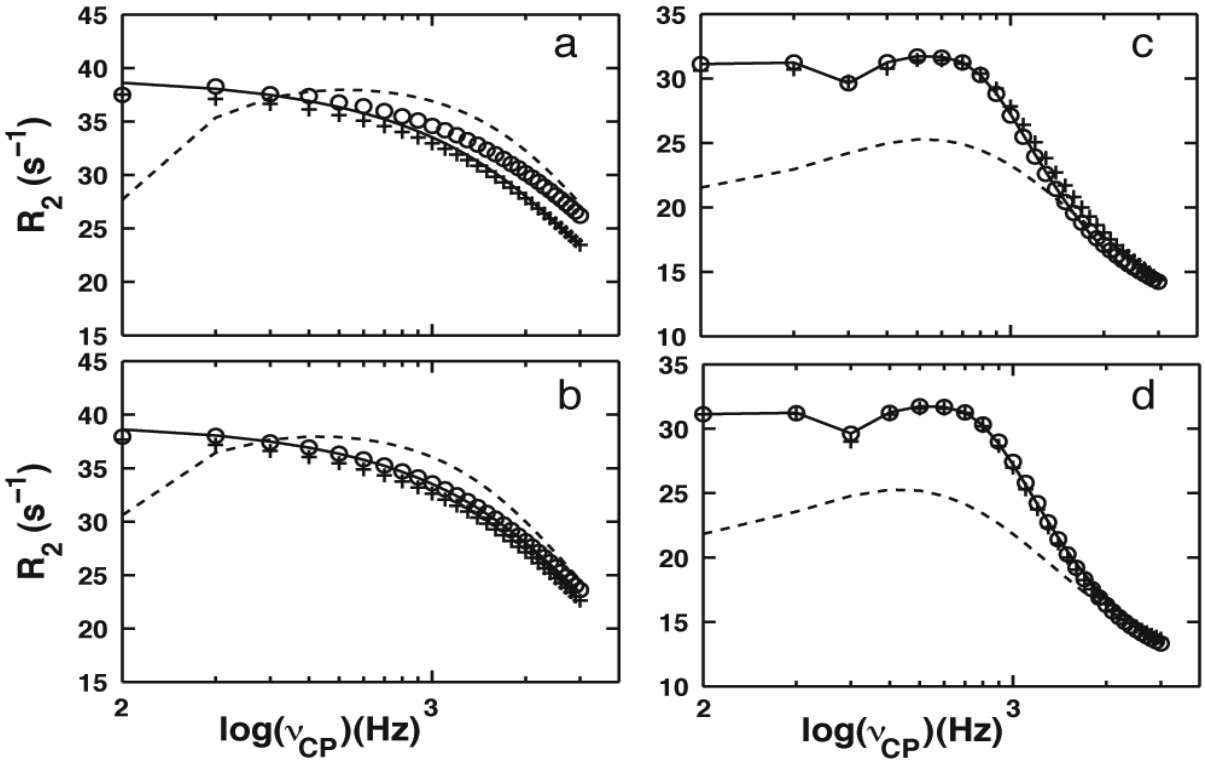

Figure 3.10 R_2 dispersion profiles calculated for (a, b) fast exchange and (c, d) slow exchange by employing (a, c) 162º pulses (-10% B_1 miscalibration) or 198º pulses (+10% B_1 miscalibration). In each figure, circles (○), and crosses (+) indicate R_2 values calculated using the $[00000000]^{\pm}$ and $[00130031]^{\pm}$ schemes, respectively. Other parameter values used for the simulations were the same as those employed to generate the profiles in Figure 3.8.

3.4 CONCLUSIONS

In this study, we have compared effect of chemical exchange contribution during pulsing in the CT-CPMG experiments by computer simulation. Exchanging signals were located close to the radio-frequency carrier in order to estimate the errors that arise by chemical exchange during the CPMG pulses, without introducing errors from the off-resonance effects. R_2 profiles that were simulated in different conditions from those described above, such as the case that signal is not close to the carrier frequency, are shown in the Supplementary material.

R_2 dispersion profile that was calculated using the standard CPMG $[00000000]^{\pm}$ scheme with a practical pulse width was shown to approach spin-lock equation in fast exchange, particularly when k_{ex} is large (> 10×10^3 s^{-1}). Although this error in the R_2 profile is small (~1 s^{-1}, **Figure 3.5b**), such error that is caused by chemical exchange during pulsing is systematically associated with the effective field strength. Consequently, when the pulse duration effect is not taken into account in the fitting of the data, this systematic error shifts the optimized exchange parameters from those originally used to generate the profile (for example, changes in p_A and k_{ex} were 3.5% and 12.5%, respectively, in **Figure 3.5b**). To avoid misinterpretation of the exchange parameters, it will be necessary to collect dispersion data of other nuclei, such as ^1H, that can be recorded using a short pulse width. When an alternative pulse scheme, $[00130031]^{\pm}$ (209; 118), was employed, chemical exchange during pulsing did not introduce significant systematic errors in the R_2 profiles. Nevertheless, when the inversion pulse is miscalibrated, R_2 values calculated using the $[00130031]^{\pm}$ scheme

with a practical pulse width is systematically reduced because of significant R_1 relaxation effects during the free-precession period.

4.0 QUANTITATIVE COMPARISON OF ERRORS IN ^{15}N TRANSVERSE RELAXATION RATES MEASURED USING VARIOUS CPMG PHASING SCHEMES.

Nitrogen-15 Carr-Purcell-Meiboom-Gill (CPMG) transverse relaxation experiment are widely used to characterize protein backbone dynamics and chemical exchange parameters. Although an accurate value of the transverse relaxation rate, R_2, is needed for accurate characterization of dynamics, the uncertainty in the R_2 value depends on the experimental settings and the details of the data analysis itself. Here, we present an analysis of the impact of CPMG pulse phase alternation on the accuracy of the ^{15}N CPMG R_2. Our simulations show that R_2 can be obtained accurately for a relatively wide spectral width, either using the conventional phase cycle or using phase alternation when the r.f. pulse power is accurately calibrated. However, when the r.f. pulse is miscalibrated, the conventional CPMG experiment exhibits more significant uncertainties in R_2 caused by the off-resonance effect than does the phase alternation experiment. Our experiments show that this effect becomes manifest under the circumstance that the systematic error exceeds that arising from experimental noise. Furthermore, our results provide the means to estimate practical parameter settings that yield accurate values of ^{15}N transverse relaxation rates in the both CPMG experiments. The results presented in this chapter have been published in *Journal of Biomolecular*

NMR, 2012, 53:13-23. In this chapter, my major contributions are in the experimental portion.

4.1 INTRODUCTION

NMR relaxation is one of powerful methods to characterize internal motion of individual sites of proteins (41; 159; 34; 86; 51; 153; 21; 166; 96; 79; 93). Several relaxation rates, including the transverse relaxation rate (R_2), are typically used to characterize the degree of internal motion in biomolecules (116; 117; 146; 99). R_2 is also used to detect slow conformational changes in biomolecules (25; 33; 150; 90; 120; 135). In biomolecular relaxation experiments, accurate error estimation is important in order to compare with NMR-derived dynamics parameters with those obtained by other methods, such as Gibbs free energy estimated from chemical exchange (188; 41; 77), molecular dynamics simulation data (28; 38; 180; 207; 71; 206), and conformational entropy estimated from generalized order parameters (4; 115; 208). The accuracy and precision of R_2 measurements, have been carefully analyzed (154; 178; 31; 169; 91; 107; 198; 209; 19; 88; 118; 139; 9; 10). However, some of the R_2 measurements remain unclear, yet.

One approach to improve the accuracy of R_2 measurements, by reducing cumulative pulse error, is an alternative phase scheme that applies pairs of orthogonal 180° pulses ($XX\bar{Y}Y$) rather than the conventional CPMG ($XXXX$) (65; 209; 118; 9; 10). The alternative phase scheme with a correction factor given to account for longitudinal relaxation during the pulsing was found to provide more accurate transverse relaxation

rates covering a wider off-resonance frequency range than the conventional scheme (209; 10). This conclusion was supported by simulation results as well as experimental results. However, the studies assumed relatively low power radio-frequency (r.f.) pulses (~2.5 kHz), which is far smaller than in typical applications (209; 10). Although we and others have studied off-resonance errors (31; 169; 107; 88; 139; 10), quantitative analysis of the uncertainty of R_2 determine using the alternative CPMG phase scheme has not been studied. Most ^{15}N CPMG relaxation experiments applied to protein backbone dynamics studies have been performed using the conventional CPMG sequence (131), and the practical advantage of the alternative phase scheme method has not yet been established.

The purpose of this chapter is to establish the condition under which the alternative phase scheme provides a practical advantage to the conventional CPMG scheme in measuring accurate R_2 values. In particular, we aim to identify whether it is advantageous or not when a relatively strong r.f. is employed for CPMG pulse train. In order to achieve this goal, we simulated ^{15}N CPMG relaxation data using three different phase schemes, and determined R_2 and its uncertainty for each as a function of off-resonance frequencies. The R_2 uncertainty was estimated by Monte Carlo error estimations in which a Gaussian distribution was assumed to generate synthetic datasets for the samplings. We generated the synthetic dataset by employing two different standard deviations (a) given by a rmsd deviation of the noise of the NMR spectra and (b) by a rmsd deviation of the residuals (I_i - I^{fit}) in the fit. Both have been used for ^{15}N relaxation data analysis (154; 144; 178). The former sampling reflects only the statistical noise uncertainties of R_2 but not any additional error. The later reflects

overall fit-uncertainties that include both experimental statistical noise and systematic errors. By comparing the R_2 uncertainties, magnitudes of the uncertainties other than those due to the experimental noise are estimated (88). Our results show that in CPMG experiments performed by employing a radio-frequency of B_1 > 5 kHz, R_2 obtained using the conventional CPMG ($XXXX$) phase scheme is close to the one obtained using the alternative phase scheme ($XXY\bar{Y}$) at the off-resonance frequency, $\omega_{off}/2\pi$, up to 1400 Hz. However, the conventional CPMG is expected to introduce higher systematic error even with $\omega_{off}/2\pi$ < 1400 Hz presumably due to non-exponential behavior of magnetization decay. We conducted ^{15}N CPMG relaxation experiments to verify the results of the calculations. Experimental results further showed that the differences in R_2 uncertainties in the two schemes are manifest only when the noise-to-signal ratio is significantly smaller than the fractional systematic error on R_2.

4.2 METHODS

4.2.1 NMR Experiments

^{15}N transverse relaxation experiments were conducted using a 0.8 mM ^{15}N labeled ubiquitin at pH 4.5 on a Bruker Avance 900 NMR instrument. Ubiquitin sample was purchased and prepared as described previously (139). Three transverse relaxation experiments were performed with a conventional CPMG phase scheme ($XX-XX$, here noted 00-00), an alternative phase scheme ($XX-Y\bar{Y}$, here noted as 00-13), and a long alternative phase scheme ($XXY\bar{Y}-XXY\bar{Y}$, here noted as 0013-0013).

Here, X and Y indicate pulse phases, and a hyphen indicates the timing applied to the ^{1}H 180° pulses to suppress cross-correlation by ^{1}H-^{15}N dipolar interaction and ^{15}N chemical shift anisotropy (CSA) (98; 155). We used the same CPMG pulse sequence that was applied previously ((46), except for an additional semi-constant time for the t_1 evolution, not in the original sequence (98). The total phase cycle is 8 with a phase inversion for the CPMG period. All the ^{15}N pulses are applied even number of times at each pulse scheme. Delays for the 00-00 and 00-13 experiments were varied: 0, 8, 16, 24, 32, 40, and 48 ms for the 00-00 and 00-13. Delays for the 0013-0013 experiments were varied: 0, 16, 32, and 48 ms. The maximum delay is set shorter than the expected $1/R_2$ because of the high sensitivity of an instrument equipped with a cryogenic probe and to avoid significant sample heating (139). Radio-frequency power for the ^{15}N pulses was 5.56 kHz (90 μs as a 180° pulse), and a half duration between ^{15}N CPMG pulses, τ_{CP}, was 0.5 ms. Here, $2\tau_{CP}$ is the time between the centers of two adjacent CPMG pulses. ^{15}N pulses were applied at 130 ppm as a carrier frequency to investigate off-resonance effects. The number of scans was 8. Using the same pulse powers, ^{15}N longitudinal relaxation was recorded for the analysis of the 00-13 type relaxation data. The delays applied for the longitudinal relaxation measurements were: 0, 0.05, 0.1, 0.25, and 0.5 s.

^{15}N transverse relaxation experiments were also performed using a 250 μM Human Immunodeficiency virus-1 (HIV-1) protease at pH 5.8 on a Bruker Avance 600 MHz NMR instrument. The protease was over-expressed and purified mainly using the previous protocol (142). Data was recorded using a conventional CPMG phase scheme ($XX-XX$) with delays of 0, 8, 16, 24, 32, 48, and 64 ms. Data were recorded by

employing the same r.f. field strength for the ^{15}N pulses, 5.56 kHz, as the same that of 900 MHz. However, the carrier frequency of the pulse was placed at 117 ppm that is approximately the center of the amide ^{15}N chemical shifts of the protease sample. 64 scans were accumulated for each free induction decay.

4.2.2 Data Analysis

Free induction decay signals were zero-filled four times, apodized with a sine window function with 40% offset, and Fourier transformed in both dimensions using NMRpipe software (35). Signal intensities at individual positions were taken instead of peak volumes using the NMRdraw software (35). Line-shape fitting algorithm was not used to estimate peak heights. Experimental noise was obtained for each two-dimensional spectrum, but assumed to be the same in each CPMG experiments.

For each time-course of magnetization decay, a transverse relaxation rate, R_2, was optimized assuming a mono-exponential decay function, $I(t) = I_0 exp(-t \cdot R_2)$. In theory, if the initial intensity is correct, there is only one unknown parameter in this equation. However, since there is small loss of intensity at time zero, both I_0 and R_2 are typically optimized. Note that the same equation is used for R_1 determination as well as R_2 in protein ^{15}N NMR relaxation since the Freeman-Hill method is used (48).

Once R_2 values were optimized, Monte Carlo error estimation was performed to estimate uncertainty of R_2. In this method, first unknown parameters, R_2 and the initial intensity, were optimized using the experimental data, and the set of the fit “ideal” intensities were back-calculated using the optimized parameters. Second, a hundred number of sets of synthetic intensity data were generated to allow a Gaussian

distribution with the ideal intensities as the mean. Finally, optimization was repeated for these synthesized data sets to calculate the standard deviation of R_2 and the initial intensity. The Gaussian distribution to generate synthetic intensities was defined in two ways:

(1) a root-mean-square deviation (rmsd) of the NMR spectral noise (154; 178)

(2) a standard deviation of the residual (I_i - I^{fit}) of the fit (144). In this article, R_2 errors that were calculated using the experimental noise are denoted $R_2^{noise\_err}$, and those were calculated using the residual of the fit are denoted $R_2^{fit\_err}$. The former reflects only experimental noise error and the later reflects overall fit-uncertainties that include both experimental statistic noise and systematic noise. By comparing the two types of R_2 uncertainties the uncertainties other than those due the experimental noise are estimated (88).

The error in the R_2 value, measured using the 00-13 and 0013-0013 sequences, caused by R_1 relaxation during the r.f. pulses is recommended to be corrected using the equation introduced by Zuiderweg's group (209):

$$R_2^{obs} = R_2 + d(R_1-R_2)/4 = R_2(1-d/4) + dR_1/4 \quad (4.1)$$

Here, *d* indicates a duty cycle of the r.f. pulse: total duration of the r.f. pulses divided by the entire CPMG delay. However, in the following analysis, no correction was made because the correction factor is calculated to be small. When pulse power $\gamma_N B_1/2\pi$ = 5.6 kHz is applied with a reasonable delay (τ_{CP} = 0.45 ms and 0.5 ms for simulation and experiments, respectively), the observed R_2 will be only 2.5% and 2.25% smaller than the correct R_2, respectively when R_1 = 0 (equation (4.1)). When 0 < R_1 < R_2, the difference becomes less than 2.5% and 2.25%, respectively. This is in contrast

to the condition that was used by Yip and Zuiderweg in which ca. 8% correction of R_2 was needed (209) . Note that since this equation does not contain any off-resonance frequency, some of the error caused by the combination of the effects of pulse imperfection and off-resonance is not corrected by this equation. We did not use the 00130031 sequence (209) because the minimum cycle, each CPMG loop (n=1) of $(00130031\text{-}00130031)_2$, needed to suppress cross correlation between ^{15}N CSA and ^{1}H-^{15}N dipolar interactions is long, i.e., 32 ms when τ_{CP} = 0.5 ms.

4.2.3 Simulation

The time evolution of bulk nuclear magnetization of a scalar-coupled ^{15}N-^{1}H spin system was calculated to determine transverse relaxation rates. For this, we used a relaxation matrix that contains 16 Cartesian product operators as the base set, as described previously (6; 7; 139; 140).

E/2 N_X N_Y N_Z H_X H_Y H_Z $2N_XH_X$

$2N_YH_X$ $2N_ZH_X$ $2N_XH_Y$ $2N_YH_Y$ $2N_ZH_Y$ $2N_XH_Z$ $2N_YH_Z$ $2N_ZH_Z$

Time dependence of the relaxation was calculated step by step for each time increment, t_1, by solving the $M(t_0+ t_1)=\exp(R_2*t_1)M(t_0)$. τ_{CP} is 0.45 ms, and each CPMG loop of $(\tau'_{CP}\text{ -}180_N\text{ - }\tau'_{CP}\text{ - }\tau'_{CP}\text{ -}180_N\text{ - }\tau''_{CP}\text{ -}180_H\text{ - }\tau''_{CP}\text{ -}180_N\text{ - }\tau'_{CP}\text{ - }\tau'_{CP}\text{ -}180_N\text{ - }\tau'_{CP})_2$ was set to be a 7.2 ms, and incremented to a total 72 ms. Here, τ'_{CP} and τ''_{CP} satisfy $\tau_{CP} = \tau'_{CP} + 90_N$ and $\tau_{CP} = \tau''_{CP} + 90_N + 90_H$. Simulation was done twice with the starting ^{15}N transverse magnetization at X and –X and detection at X and –X, respectively, for the phase cycle. The output is the average time course of the two phase cycles. In the relaxation matrix, ^{1}H and ^{15}N chemical shift and the 90-Hz ^{1}H-^{15}N J-coupling evolution, r.f. pulse effects, auto and cross relaxation

terms, and cross-correlation terms were included (6; 7; 139; 140). In the calculation, ^{15}N and ^{1}H r.f. pulses were applied at field strengths of 5.56 kHz and 25 kHz, respectively, and ^{15}N signal off-resonance frequency, $\omega_{off}/2\pi$, was varied from -3000 to 3000 Hz in 200 Hz steps. Off-resonance frequency of the ^{1}H signal was set at 2250 Hz, which corresponds to 7.5 ppm at 900 MHz NMR. Relaxation terms in the matrix were calculated assuming a simple Lorentzen spectral density function with a 5 ns rotational correlation time, 170 ppm ^{15}N CSA, and 1.02 Å N-H distance. Additional ^{1}H longitudinal and transverse relaxation rates of 10 s^{-1} and 20 s^{-1} were added, in addition to the ^{1}H-^{15}N dipolar term, to the ^{1}H relaxation (139).

Once the time dependence was calculated, R_2 and its uncertainty, $R_2^{fit\_err}$, were determined by Monte-Carlo error estimation using the standard deviation of the residual (I_i - I^{fit}) of the fit as the uncertainty in I_i (144). However, $R_2^{noise\_err}$ was not calculated because experimental noise itself was not assumed in the simulation. The effect of the inhomogeneity of the B_1 field was simulated by assuming that relative magnetization intensities of 0.375, 0.5, and 0.125 experienced respective r,f, field strengths of $1.0B_1$, $1.05B_1$ and $1.1B_1$, respectively, where B_1 is the correctly calibrated field strength. Then, R_2 and $R_2^{fit\_err}$ were determined from simulations of the weighted time course of the average magnetization. The simulation analysis for B_1 inhomogeneity was performed for the [00-00] and the [00-13] schemes individually. Calculations were performed using MATLAB software (The Mathworks Inc., Natick, MA).

4.3 RESULTS AND DISCUSSION

The purposes of this study are to further identify systematic errors, that persist even when experiments are repeated (16; 69), in ^{15}N transverse relaxation rates, which are used to characterize protein backbone dynamics. In particular, uncertainties in CPMG R_2 values caused by systematic errors present when using phase schemes, [00-00], [00-13], and [0013-0013] are compared. For this purpose, we will firstly compare values of R_2 and $R_2^{fit\_err}$ derived from simulations of measurements obtained using phase-schemes, [00-00] and [00-13]. Next, we will compare experimental results obtained using the [00-00], [00-13], and [0013-0013] schemes. In the evaluation of the experimental results, R_2 errors estimated from two sets of Monte-Carlo methods, $R_2^{fit\_err}$ and $R_2^{noise\_err}$, are compared as well as the R_2 values to idenity systematic errors.

4.3.1 Simulated off-resonance frequency dependence of [00-00] and [00-13] at a practical r.f. power level

The time course of magnetization in a scalar-coupled two-spin system was calculated for the conventional phase [00-00] and the alternative phase [00-13], using r.f. pulse power of $\gamma_N B_1/2\pi$ = 5.6 kHz (i.e., 90 μs, 180° pulse) at varying off-resonance frequency, $\omega_{off}/2\pi$. Time courses of magnetization obtained by employing the [00-00] scheme at $\omega_{off}/2\pi$ = ±2400 Hz exhibit non single-exponential decay profiles (**Figure 4.1A**). The profiles are basically consistent to the previous results (For example, Fig. 4 of the reference, (209)). In contrast, the time course of magnetization obtained by employing the [00-13] scheme under the same conditions exhibited profiles that are

closer to a single-exponential decay (**Figure 4.1B**). This result is consistent with previous observations (209; 10). Note that our simulation shows slightly different profiles at positive and negative $\omega_{off}/2\pi$. Such a different is not observed in the simulation for a single spin system, or when ^{1}H signal is located at the r.f. carrier frequency in the two-spin system (data not shown). Thus, although an even number of ^{1}H pulses is applied in each CPMG cycle, the difference in profiles is most likely due to an asymmetry caused by an ^{1}H off-resonance effect. The effect of the coupled spin was not taken into account in the previous CPMG simulations for the alternative phase schemes (209; 10).

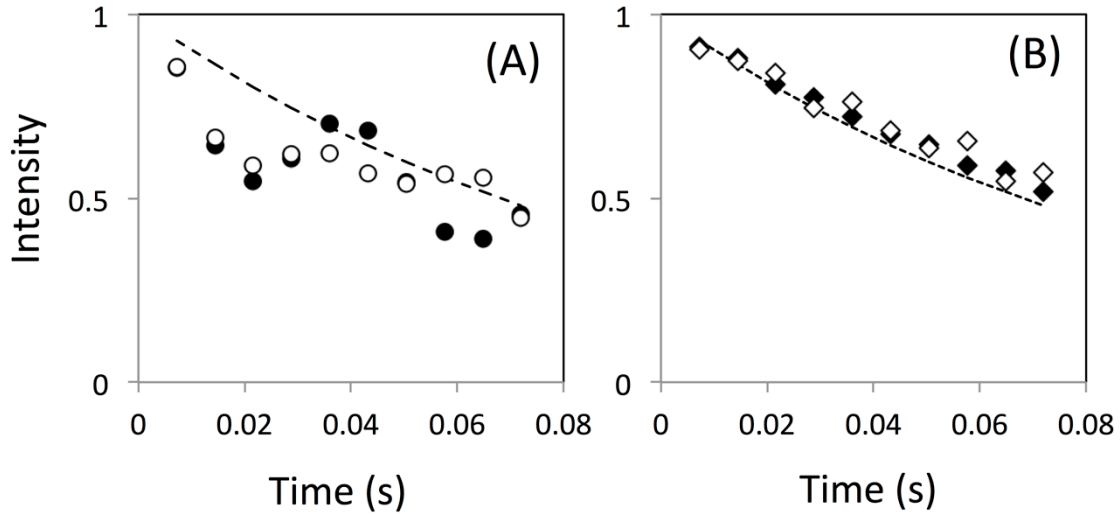

Figure 4.1 Simulated time course of transverse magnetization simulated using (A) the [00-00] sequence (circles) and (B) the [00-13] sequences (diamonds). In each figure, calculations were performed with $\omega_{off}/2\pi$ set equal to +2400 Hz (open circles) and -2400 Hz (closed circles).

Once the time course of magnetization was simulated, R_2 was determined by assuming that each time course decayed as a single-exponential function. The resultant R_2 values are shown as a function of the absolute value of $\omega_{off}/2\pi$ in **Figure 4.2A**. R_2 values were determined using both [00-00] and [00-13] schemes and are

denoted as $R_2^{00\text{-}00}$ and $R_2^{00\text{-}13}$, respectively. Both R_2 values were quite similar up to an off-resonance frequency, $\omega_{off}/2\pi$ = 1400 Hz (i.e., $\omega_{off}/(\gamma_N B_1)$ = 0.25), with average difference in R_2 1.2% and with the maximum difference in R_2 of 2.2% (**Figure 4.2A**). Within each individual scheme, the fractional root-mean square deviations of R_2 values in the range from $\omega_{off}/2\pi$ 0 to 1400 Hz were 0.20% and 0.17% for $R_2^{00\text{-}00}$ and $R_2^{00\text{-}13}$, respectively. These results were obtained including all data except for the $R_2^{00\text{-}00}$ point at 1200 Hz. As shown by an arrow in **Figure 4.2A**, the $R_2^{00\text{-}00}$ at 1200 Hz was significantly higher than others. When the magnetization along X-axis starts CPMG duration and the pulses are applied from the X-axis, the Y-component of the transverse magnetization vector rotates through the Y-Z plane during the pulsing whereas the X-component stays mostly in the transverse plane. Thus, pulse imperfection effect caused by chemical shift precession during the pulsing becomes largest when a magnetization vector undergoes almost 360° precession between the adjacent CPMG pulses, as has been shown in other simulation and experimental results (209; 10).

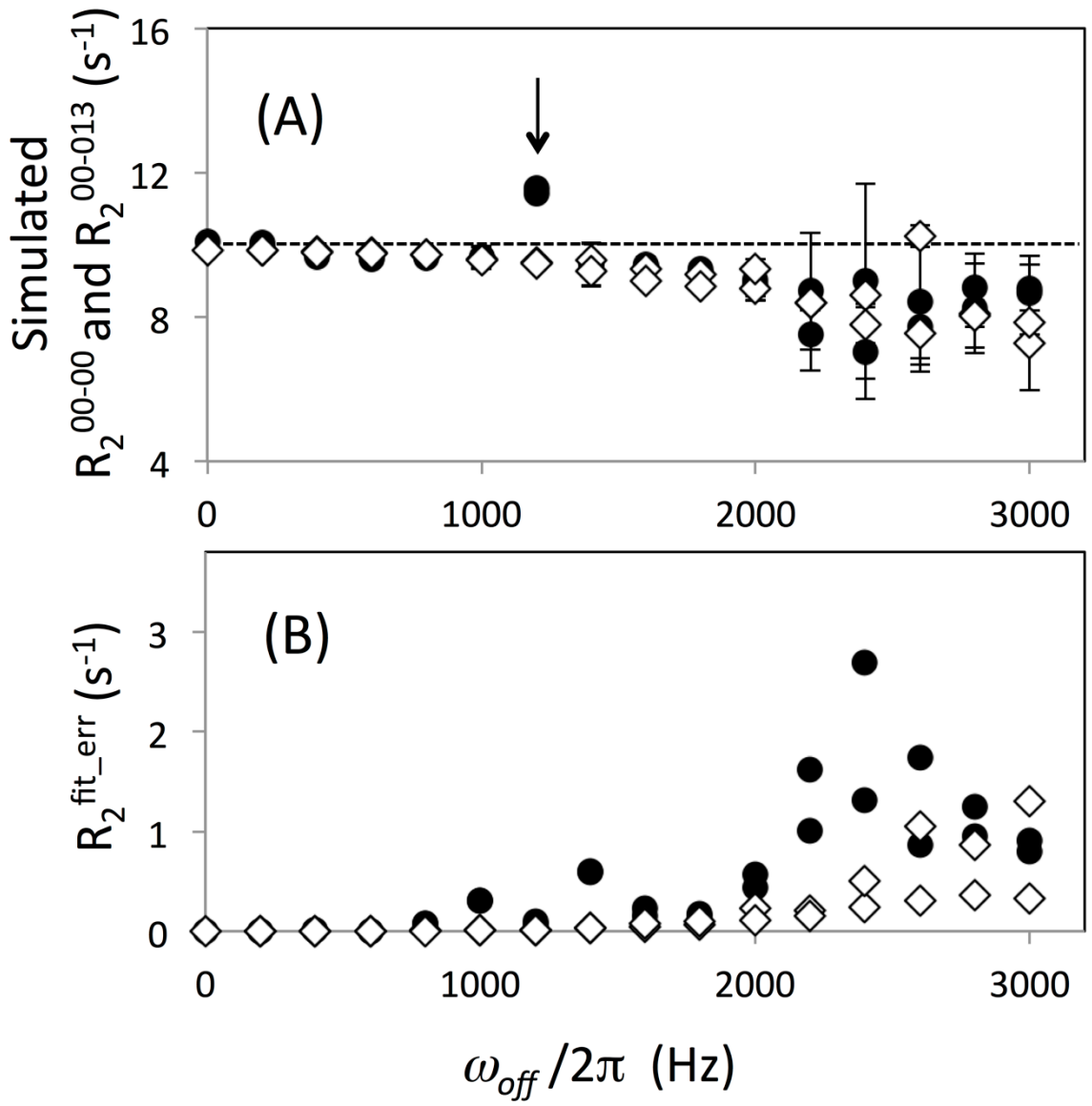

Figure 4.2 (A) Transverse relaxation rate, R_2, and (B) its error, $R_2^{fit\_err}$, determined by simulation using the [00-00] (filled circles) and the [00-13] (open diamonds) sequences, plotted as a function of the absolute off-resonance frequency, $\omega_{off}/2\pi$. Simulation of the time dependence of magnetization was performed varying $\omega_{off}/2\pi$ from -3000 to 3000 Hz at a 200 Hz step. Note that there are two data points determined using each pulse scheme at each $\omega_{off}/2\pi$ point, i.e., at the positive and the negative frequencies (Here, the two data points are shown by the same symbols). The arrow in (A) indicates a data point at a frequency that is close to the inverse of the CPMG pulse duration, a condition in which magnetization undergoes almost 360° precession during the period between the two adjacent CPMG pulses (see text). In (A), the dashed line indicates the original R_2 determined only by the auto relaxation. R_2

values are all plotted with $R_2^{fit\_err}$ as the error bars, while some of the error bars may not be notably large. $R_2^{fit_err}$s were estimated from the residual of the fits (see Methods section).

At $\omega_{off}/2\pi$ > 1400 Hz, deviations of R_2 by the off-resonance effects are observable in both $R_2^{00\text{-}00}$ and $R_2^{00\text{-}13}$ (**Figure 4.2**). In previous results, $R_2^{00\text{-}13}$ profiles were reported to exhibit a smaller and smoother change than those of $R_2^{00\text{-}00}$ (209; 10). This discrepancy between these results and ours is mostly caused by differences in experimental and simulation parameter: their applied B_1 field strength ($\gamma_N B_1/2\pi \leq 2.5$ kHz) was smaller than that of ours ($\gamma_N B_1/2\pi$ = 5.6 kHz), and their τ_{CP} (0.35 ms) was shorter than ours (0.45 ms and 0.5 ms). The latter set of the parameters make the [00-00] profile unfavorable. In addition, even in the previous experimental results, reduced but clear deviations of R_2 caused by off-resonance effects were shown even in $R_2^{00\text{-}13}$ (209; 10). Errors in $R_2^{00\text{-}13}$ found at a large $\omega_{off}/2\pi$ values are not corrected by equation (4.1) because equation (4.1) does not contain off-resonance frequency as one of calibration parameters. Overall, using our practical conditions for ^{15}N relaxation measurements, $R_2^{00\text{-}00}$ and $R_2^{00\text{-}13}$ exhibit similar profiles almost within the entire experimentally required $\omega_{off}/2\pi$ range.

Uncertainty of each R_2 value, $R_2^{fit\_err}$, was estimated from the Monte-Carlo method by assuming an average residual of the simulated intensities from the fit-intensities as a standard deviation for the normal distribution (**Figure 4.2B**). This $R_2^{fit\_err}$ solely reflects a discrepancy from a single-exponential decay model. $R_2^{fit\_err}$ for $R_2^{00\text{-}13}$ exhibits very small uncertainties (<0.1 s^{-1} that correspond to <1% of $R_2^{00\text{-}13}$) in the entire $\omega_{off}/2\pi$ range. In contrast, $R_2^{fit\_err}$ obtained for $R_2^{00\text{-}00}$ exhibited large uncertainties at ω_{off}

/2π > 1800 Hz, reflecting non-exponential behavior of magnetization simulated using the [00-00] scheme (**Figure 4.2B**). Nevertheless, $R_2^{fit\_err}$ values for $R_2^{00\text{-}00}$ (< 2%) remained small for $\omega_{off}/2\pi$ < 1800 Hz. Again this frequency range covers nearly all ^{15}N signals of backbone amides in diamagnetic proteins up to 20 ppm at a 91 MHz ^{15}N resonance frequency (**Figure 4.2B**). Overall, application of the practical B_1 field strength ($\gamma_N B_1/2\pi$ = 5.6 kHz) provides similar R_2 values in both $R_2^{00\text{-}00}$ and $R_2^{00\text{-}13}$ schemes, within the spectral range of ±1400 Hz.

4.3.2 Effects of pulse strength miscalibration on R_2 error, determined by simulation

Similar simulations of magnetization and the determinations of R_2 were performed varying the B_1 field strength keeping the pulse width constant (i.e., power miscalibration). At a 5% or 10% increase (miscalibration) of the B_1 field strength, $R_2^{00\text{-}00}$ exhibits more variation of R_2 values at $\omega_{off}/2\pi$ < 1400 Hz (**Figure 4.3A**), which is larger than the variation of $R_2^{00\text{-}13}$ (**Figure 4.3B**). Similar to these observations, but more significantly, $R_2^{fit\_err}$ for $R_2^{00\text{-}00}$ (**Figure 4.3D**) became larger than that of $R_2^{00\text{-}13}$ at the miscalibrated B_1 field strength (**Figure 4.3E**). In particular, the $R_2^{fit\_err}$ for $R_2^{00\text{-}00}$ increased in proportion to the power miscalibration (**Figure 4.3D**). Such differences between $R_2^{00\text{-}00}$ and $R_2^{00\text{-}13}$, and between $R_2^{fit\_err}$ for $R_2^{00\text{-}00}$ and $R_2^{fit\_err}$ for $R_2^{00\text{-}13}$ are reduced when B_1 inhomogeneity is taken into account in the simulations (**Figures 4.3C** and **4.3F**). Overall, the simulations demonstrate that the difference between R_2 obtained using $R_2^{00\text{-}00}$ and $R_2^{00\text{-}13}$ is insignificant for a relatively wide spectral width, provided that r.f. pulses are properly calibrated (**Figure 4.2**). However, the difference becomes

significant when r.f. pulses are miscalibrated (**Figure 4.3**). In particular, the [00-13] scheme is more tolerant to miscalibration errors than the [00-00] scheme.

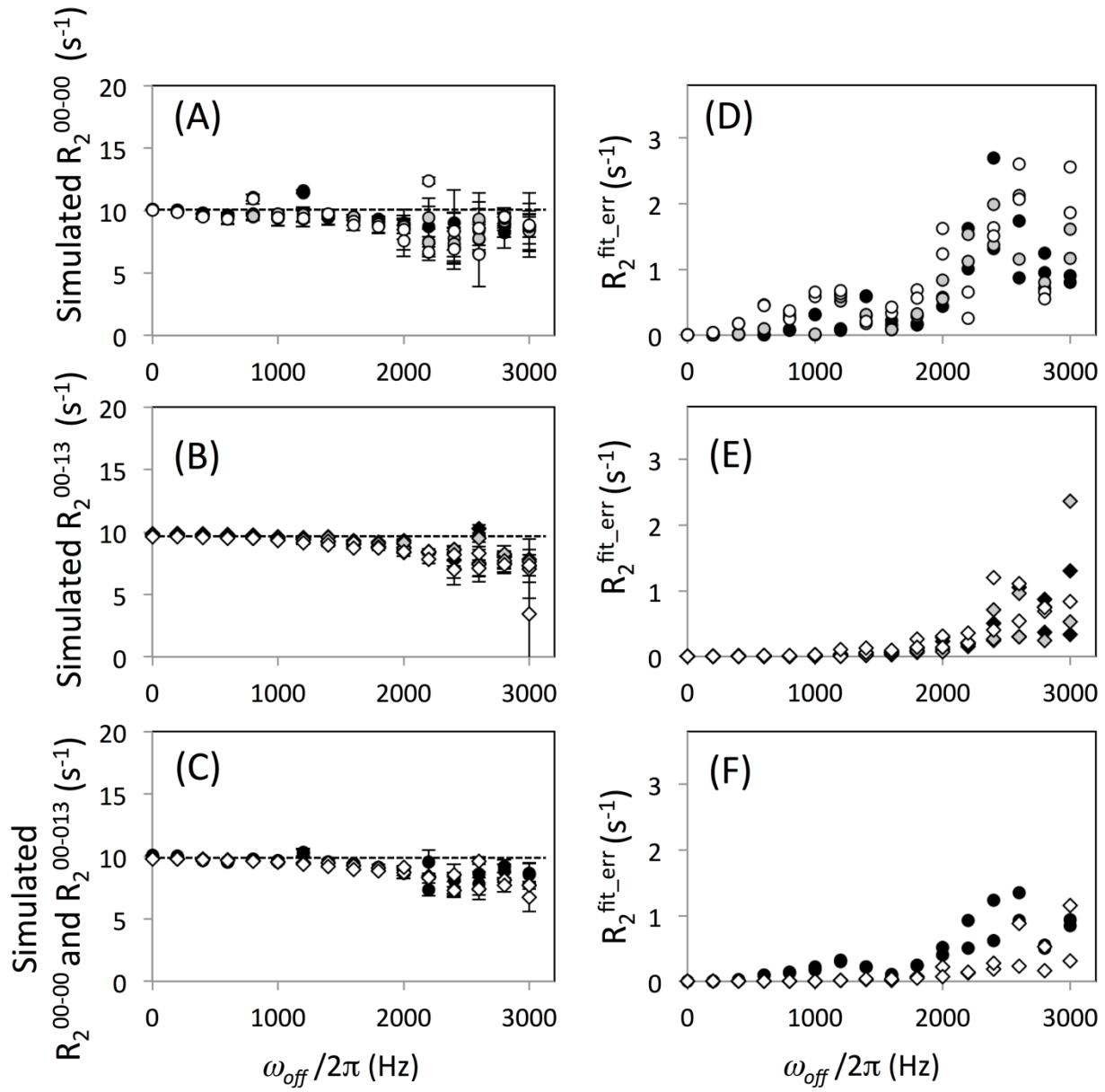

Figure 4.3 (A, B, C) Transverse relaxation rate, R_2, and (D, E, F) its error, $R_2^{fit\_err}$, determined by simulation, plotted as a function of the off-resonance frequency, $\omega_{off}/2\pi$. Simulation was performed (A, D) using the [00-00] scheme, (B, E) using the [00-13] scheme, and (C, F) assuming the B_1 inhomogeneity for both. In all figures, circle and diamond symbols indicate for R_2 obtained using the [00-00] and the [00-13] schemes, respectively. In (A-E), simulation of the time dependence of magnetization was done at a correctly calibrated B_1 field strength of 5.56 kHz

CPMG 180º pulse of 90 μs (filled symbols), at a 5% stronger B_1 field strength (gray symbols), and at a 10% stronger B_1 field strength (open symbols). In (C) and (D), R_2 and $R_2^{fit\_err}$ determination assuming B_1 inhomogeneity was performed for both of the [00-00] and the [00-13] schemes (see Methods section). In the calculation, $\omega_{off}/2\pi$ was varied from -3000 to 3000 Hz at a 200 Hz step. There are two data points determined using each condition at each $\omega_{off}/2\pi$, i.e., at the positive and the negative frequencies. In (A-C), R_2 values are all plotted with $R_2^{fit\_err}$ as the error bars while some of the error bars may not be notably large.

4.3.3 Experimental R_2 determined using [00-00], [00-13], and [0013-0013] sequences.

To verify the predictions of these simulations, we conducted ^{15}N R_2 experiments for ubiquitin using a 900 MHz NMR instrument, and evaluated experimental results only for signals that were fit by an single-exponential decay function with $R_2^{err} < 1\ s^{-1}$ (**Figure 4.4**). Most of the $R_2^{00\text{-}00}$ values were very similar to $R_2^{00\text{-}13}$ values (**Figure 4.4A**). As shown in **Figure 4.4C**, $R_2^{00\text{-}00}$ and $R_2^{00\text{-}13}$ did not exhibit significant difference for signals at $\omega_{off}/2\pi < 500$ Hz, but the R_2 values increasingly differ as $\omega_{off}/2\pi$ (off-resonance) increases. In contrast, although the effect of resonance off-set for $R_2^{0013\text{-}0013}$ is basically similar to that of $R_2^{00\text{-}13}$ (**Figure 4.4B**), $R_2^{0013\text{-}0013}$ exhibits differences from $R_2^{00\text{-}13}$ even when, $\omega_{off}/2\pi < 500$ Hz (**Figure 4.4D**). Since the [0013-0013] scheme is more symmetric with respect to the ^1H 180° pulses than the [00-13] scheme, a possible explanation of the poor performance of the [0013-0013] scheme when $\omega_{off}/2\pi$ is small may be incomplete suppression of CSA-dipolar cross correlation. In the [0013-0013] scheme the period between ^1H 180° pulses is twice that of [00-13] scheme. As shown previously (98; 155), the cross correlation is suppressed in a two-spin system. However,

artifacts in R_2 measurements may become significant because of the interactions with external protons that have been neglected in our simulations.

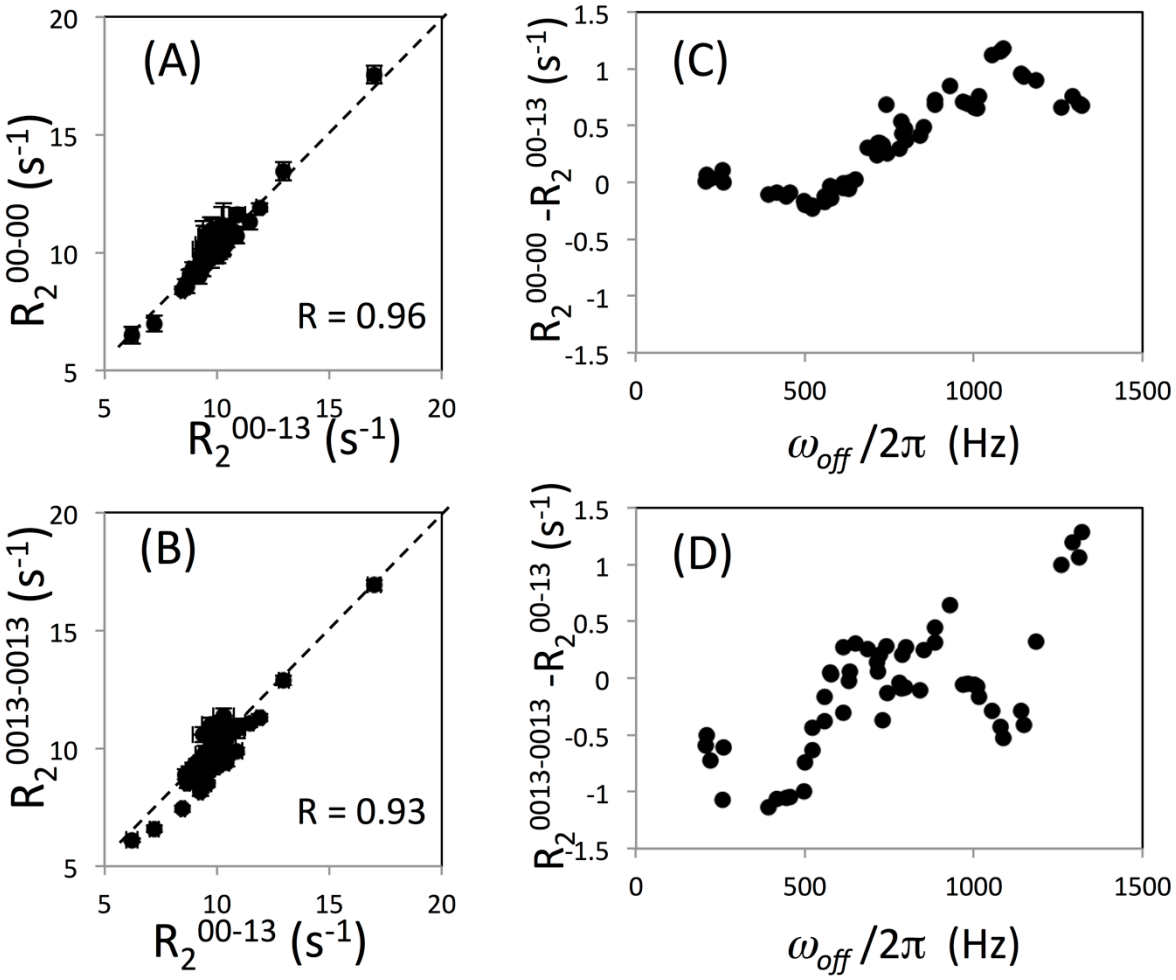

Figure 4.4 Transverse relaxation rate, R_2, for ubiquitin experimentally determined using the [00-13] sequence was compared with (A) those obtained using the conventional [00-00] sequence and (B) those obtained using the [0013-0013] sequence using a 900 MHz NMR instrument. Difference of (C) the rates determined between the [00-00] and the [00-13] schemes, and (D) between the [0013-0013] and the [00-13] schemes are shown as a function of the off-resonance frequency, $\omega_{off}/2\pi$. Note that the number of relaxation data points corrected for the [0013-0013] sequence were smaller than those of [00-00] and [00-13] due to the longer cycle length. For this reason, a [00130031-00130031] sequence (209) was not applied. Only the data points at $\omega_{off}/2\pi < 1500$ Hz were include because large error bars at larger resonance off-sets make it difficult to view the correlation plots. In (A) and (B), R_2 values are all plotted with $R_2^{fit\_err}$ error bars but may not be notable when the errors are small.

Monte-Carlo error estimation was calculated for ubiquitin R_2 values in two ways: using the spectral noise ($R_2^{noise\_err}$) and using the residual of the fits ($R_2^{fit\_err}$), to generate the synthetic data. Since ubiquitin is a rigid, small protein, amide signal heights were quite uniform (except for E24 that undergoes chemical exchange and exhibits severe line broadening at 900 MHz) as is evident in the R_2 correlations plotted in **Figure 4.4**. Therefore, $R_2^{noise\_err}$ was approximately the same for all three datasets (**Figure 4.5**, circles). In contrast, $R_2^{fit\_err}$ exhibits quite different profiles for $R_2^{00\text{-}00}$ (**Figure 4.5A**, ×-symbols) compared with $R_2^{00\text{-}13}$ and $R_2^{0013\text{-}0013}$ (**Figures 4.5B and 4.5C**, ×-symbols). $R_2^{fit\_err}$ for $R_2^{00\text{-}00}$ begins to increase at $\omega_{off}/2\pi$ ca. 1000 Hz, and becomes over 2 s^{-1} at $\omega_{off}/2\pi$ > 1800 Hz (**Figure 4.5A**, ×-symbols). This profile is consistent with the simulations that incorporate the effect of pulse miscalibration, **Figure 4.3F**, demonstrating the excellent performance of the calculations. $R_2^{fit\_err}$ for $R_2^{00\text{-}13}$ and $R_2^{0013\text{-}0013}$ exhibits a more gradual increases as a function of $\omega_{off}/2\pi$, and stays smaller than $R_2^{fit\_err}$ for $R_2^{00\text{-}00}$ even at $\omega_{off}/2\pi$ ~1500 Hz. This small gradual increase of R_2^{err} for the phase alternation experiments is also consistent with the simulation results, **Figure 4.3F**. Overall, in both $R_2^{00\text{-}00}$ and $R_2^{00\text{-}13}$, $R_2^{fit\_err}$ almost equals $R_2^{noise\_err}$ when $\omega_{off}/2\pi$ is small, and increases as $\omega_{off}/2\pi$ increases. This increasing discrepancy between the $R_2^{fit\_err}$ and $R_2^{noise\_err}$ as $\omega_{off}/2\pi$ increases is clear evidence of the off-resonance related systematic error.

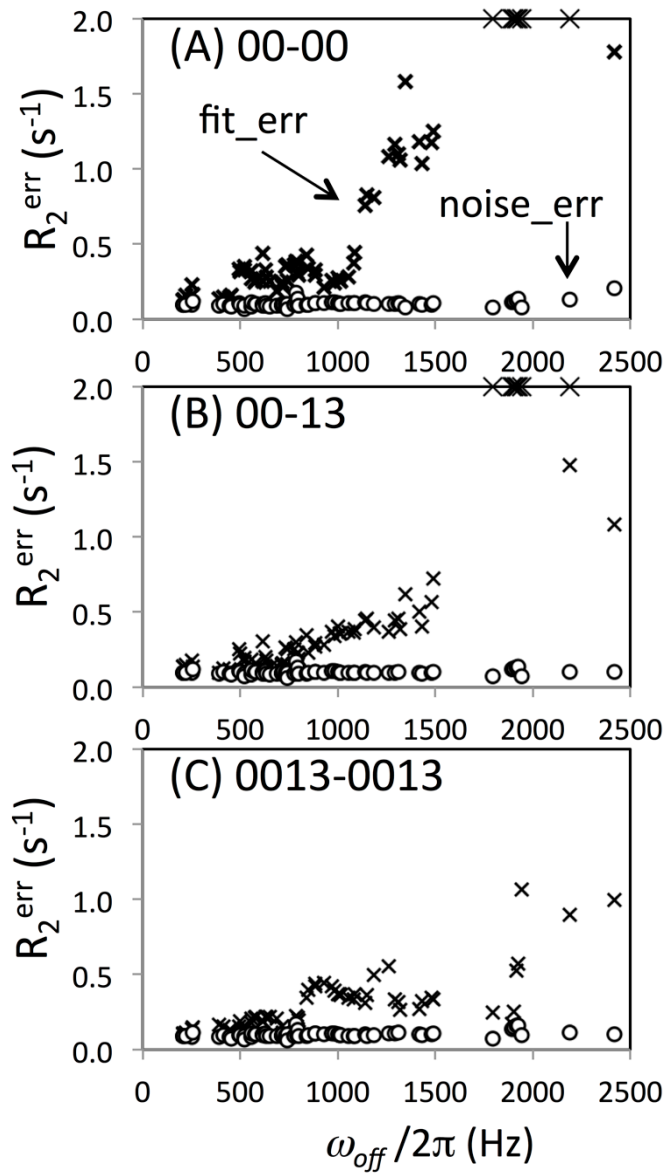

Figure 4.5 Uncertainties, R_2^{err}, of the transverse relaxation rates for ubiquitin experimentally determined using (A) [00-00], (B) [00-13], and (C) [0013-0013] sequences on a 900 MHz NMR instrument, shown as a function of the off-resonance frequency, $\omega_{off}/2\pi$. R_2 values that are shown in Figure 4.4 are used. An additional 16 sets of data that exhibited $R_2^{err} > 1\ s^{-1}$ were also included in the graphs in order to show how the uncertainty increases as a function of $\omega_{off}/2\pi$. R_2^{err} values were determined by two different Monte-Carlo error estimations in which the standard deviations of a Gaussian distribution function that generates synthetic data sets were given by rmsd of spectral noise, $R_2^{noise\_err}$ (circle), and by rmsd of residuals of the initial fit intensities, $R_2^{fit\_err}$ (×-symbols). Difference of the two uncertainties indicates errors other than experimental noise. R_2^{err} values above 2 s^{-1} are shown as the ceiling values.

4.3.4 Off-resonance systematic error is not observed in large proteins

To test if off-resonance effects are observable in the case of a larger protein with less spectra sensitivity than ubiquition, the CPMG experiments were also performed for HIV-1 protease using a 600 MHz instrument. In this experiment, the ^{15}N pulse carrier was placed at 117 ppm which is almost the center of the ^{15}N chemical shifts of the protease backbone amides. $R_2^{00\text{-}00}$ for the 92 residues are on average 15.22 s^{-1} ($\pm$2.1 s^{-1}), which is approximately 1.5 times larger than that of ubiquitin and consistent with previous measurements on HIV-1 protease (46). $R_2^{00\text{-}00}$ values are relatively uniform in this $\omega_{off}/2\pi$ range (**Figure 4.6A**). $R_2^{noise\_err}$ is 0.17 s^{-1} whereas $R_2^{fit\_err}$ is 0.22 s^{-1} (**Figure 4.6B**). The $R_2^{noise\_err}$ values are approximately 2% of $R_2^{00\text{-}00}$. Although some $R_2^{fit\_err}$ are higher at $\omega_{off}/2\pi$ > 500 Hz, the differences between $R_2^{noise\_err}$ and $R_2^{fit\_err}$ are not significant. Thus, differences in R_2^{err} estimated by two methods are not observed because the noise error is larger than the off-resonance error. This result is in contrast to that obtained for ubiquitin.

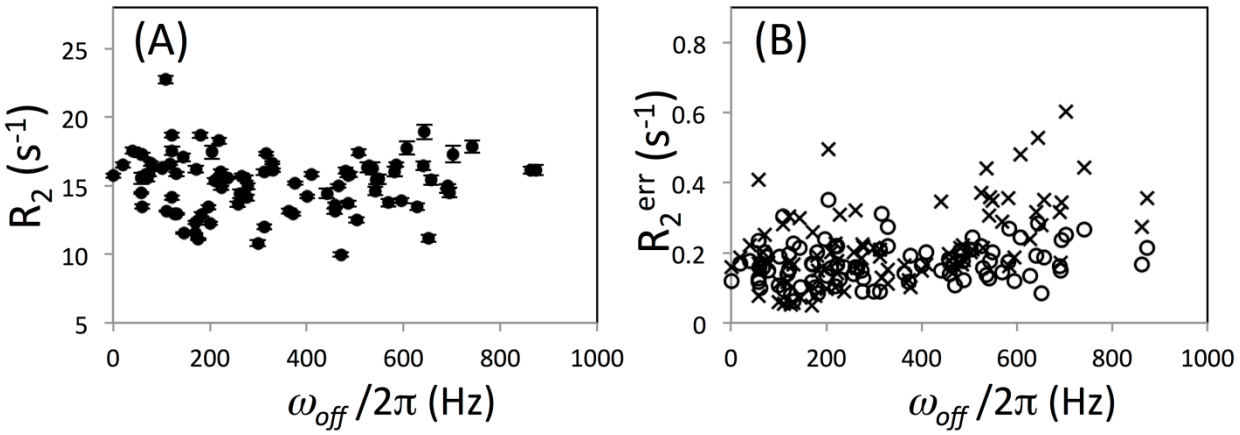

Figure 4.6 (A) Transverse relaxation rate, R_2, and (B) its uncertainty, R_2^{err}, for HIV-1 protease experimentally determined using the [00-00] sequence on a 600 MHz NMR instrument with 117 ppm as ^{15}N pulse carrier

frequency. In (A), R_2 values are all plotted with $R_2^{fit\_err}$ error bars but may not be notable when the errors are small. In (B), R_2^{err} values were determined by two different Monte-Carlo error estimations in which the standard deviations of a Gaussian distribution function that generates synthetic data sets were given by rmsd of spectral noise, $R_2^{noise\_err}$ (circle), and by rmsd of residuals of the initial fit intensities, $R_2^{fit\_err}$ (×-symbols).

4.4 CONCLUSIONS

In this study, ^{15}N CPMG experiments with and without the phase alternation were investigated at the practical high pulse power ($\gamma_N B_1/2\pi$ = 5.6 kHz) and also with ^1H 180° pulses that are applied to suppress dipolar/CSA cross correlation. Since CPMG performance is determined by the field strength of the r.f. pulse ($\gamma_N B_1/2\pi$), the delay between the CPMG pulses (τ_{CP}), the off-resonance frequency ($\omega_{off}/2\pi$), and relaxation rates and scalar couplings, it is important to investigate the performance at optimal parameter settings. First, our results showed that, in the high power condition, both pulse phase schemes yield similar results unless resonance off-sets are very large. Our simulations reproduced the reduction of the measurement accuracy as $\omega_{off}/2\pi$ increases even with the phase alternation method, which is consistent with the experimental results. Second, when the pulse power is miscalibrated, the fit error becomes larger in the conventional CPMG than the phase alternation approach, even when the resonance off-set is small. Third, although the full (longer) phase alternation cycle has a better performance in theory, our experimental results show that the actual performance of the longer cycle was not improved in the ^{15}N experiments with ^1H 180° pulses.

5.0 CHARACTERIZATION OF SARCOPLASMIC RETICULUM CA^{2+} ATPASE NUCLEOTIDE BINDING DOMAIN MUTANTS USING NMR SPECTROSCOPY

Sarcoplasmic reticulum Ca^{2+} ATPase (SERCA) is essential for muscle function by transporting Ca^{2+} from the cytosol into the sarcoplasmic reticulum through ATP hydrolysis. In this report, the effects of substitution mutations on the isolated SERCA-nucleotide binding domain (SERCA-N) were studied using NMR. ^{15}N-^{1}H HSQC spectra of substitution mutants at the nucleotide binding site, T441A, R560V, and C561A, showed chemical shift changes, primarily in residues adjacent to the mutation sites, indicating only local effects. Further, the patterns of chemical shift changes upon AMP-PNP binding to these mutants were similar to that of the wild type SERCA-N (WT). In contrast to these nucleotide binding site mutants, a mutant found in patients with Darier's Disease, E412G, showed small but significant chemical shift changes throughout the protein and rapid precipitation. However, the AMP-PNP dissociation constant (~2.5 mM) was similar to that of WT (~3.8 mM). These results indicate that the E412G mutant retains its catalytic activity but most likely reduces its stability. Our findings provide molecular insight into previous clinical, physiological, and biochemical observations. The results presented in this chapter have been published in *Biochemical and Biophysical Research Communications*, 2011, 405:19-23. In this chapter, my major contributions are in the whole chapter.

5.1 INTRODUCTION

The sarco(endo)plasmic Ca^{2+} ATPase (SERCA) is responsible for transporting cytosolic Ca^{2+} into the lumen of the sarcoplasmic reticulum (SR) upon muscle relaxation, through hydrolysis of ATP (8; 160; 44; 20). SERCA dysfunction has been implicated in heart failure (173; 132; 136) and in a skin disorder known as Darier's disease (170; 172; 167; 36; 133). Thus, it has been an important target for basic and translational research (162; 136; 81). Crystal structures of SERCA at different stages in the Ca^{2+} transport cycle have shown the step-by-step interactions of the three cytosolic domains and the transmembrane domain (193; 149; 182; 148; 114; 192; 203). In the Ca^{2+} pump mechanism, there are two major conformational states, E1 and E2, that allow Ca^{2+} ions to cross from the cytoplasm and luminal sides, respectively (124). One of the cytosolic domains, SERCA-N, is an ATPase and contains an ATP binding site. This domain plays a major role in the conversion from E1 to E2 and interfaces with the other domains, SERCA-A and SERCA-P.

Previous studies on several mutants of SERCA-N suggest that slight changes of domain conformation can influence both Ca^{2+} transport and ATPase activity, but not necessarily to the same degree. For example, while mutation at the ATP binding site, T441A, reduced both Ca^{2+} transport capacity and ATPase activity to about 50% of the WT level, R560V displayed approximately 60% of the WT Ca^{2+} transport capacity and only 30% of WT ATPase activity (29). However, mutation at a residue adjacent to R560, C561A, reduced Ca^{2+} transport rate to ca. 80% of WT without affecting ATP binding affinity (29). Although these apparent discrepancies could be explained by distinct conformational changes in the protein upon mutation of specific residues, an

analysis of the conformational impact of these mutations has not been performed. Furthermore, E412G mutation, which has been found in patients with Darier's Disease but not in those with heart dysfunction (170; 172; 167; 36; 133), has not been analyzed at a structural level. An understanding of the structural consequence of the E412G mutation, which is located in the interior of the N-domain, over 16 Å away from the nucleotide-binding site, may be useful to understand why the mutation does not cause heart dysfunction. Overall, while the structural basis of SERCA phospholylation and its interactions with phospholamban and the membrane (63; 64; 145; 210; 197) have been well characterized, the structural consequences of the N-domain mutations have not been reported.

The isolated SERCA-N domain retains nucleotide binding and its native structure (27; 2; 3), and was, therefore, used in the described Circular Dichroism and NMR studies. Specifically, single substitution mutations of E412G, T441A, R560V, or C561A were created to elucidate the effect of each mutation on the SERCA-N structure. Our findings provide atomic level insight into previous biochemical and clinical observations.

5.2 MATERIALS AND METHODS

5.2.1 Protein Expression and Purification

The WT SERCA-N sequence (residues 357-660) from rabbit SERCA1a was cloned into a pET15b vector, as described by Mitsu Ikura's group (2), and was modified at the N-terminus to incorporate a tobacco etch virus (TEV) cleavable Poly-Histidine

sequence (His_6-tag). The final protein sequence contains an additional three-residue, amino acid sequences of SVD before T357 instead of the GSHM sequence in the previously studied construct (2). The SERCA-N mutants E412G, T441A, R560V, and C561A were constructed by site directed mutagenesis of the WT plasmid following manufacturer's protocol (Stratagene). The vector was transformed into Rosetta 2 (DE3) cells, and protein was expressed in 1 L cultures of minimal M9 medium with 1 g/L [^{15}N]-NH_4Cl at 18ºC for 16 h by addition of isopropyl β-D-1-thiogalactopyranoside (IPTG) at a final concentration of 0.8-1 mM. For the WT and C561A mutant, additional protein sample was prepared with minimal M9 medium supplemented with 1 g/L [^{15}N]-NH_4Cl and 2 g/L [$^{13}C_6$]-glucose at 37ºC. Proteins in cell lysate in a buffer A (50 mM Sodium Phosphate pH 7.5, 500 mM NaCl, 20 mM Imidazole, 0.02% NaN_3, and 5 mM β-mercaptoethanol) were first purified by applying to a 5 mL HisTrap HP column (GE Healthcare) and then eluting with a buffer containing 500 mM Imidazole in A, The aggregate was removed by a Superdex-75 (GE healthcare) Gel Filtration chromatography column, equilibrated in buffer B (25 mM Sodium Phosphate pH 7.5, 50 mM NaCl, and 0.02% NaN_3). The His_6-tag was removed by overnight TEV digestion, and proteins were purified by application to a HisTrap HP column (GE Healthcare) at 4ºC. The buffer was exchanged by dialysis to 25 mM Bis-Tris pH 6.5, 150 mM NaCl, 5 mM TCEP, and 0.02% NaN_3 and the proteins were concentrated using Amicon Ultra Centrifugal Filter Units (Millipore) prior to flash freezing by liquid nitrogen. Samples were stored at -80ºC with or without lyophilization.

5.2.2 Circular Dichroism and UV Spectroscopies

Protein samples for Circular Dichroism (CD) spectroscopy measurements were prepared by exchanging the buffer with 20 mM Tris, pH 7.5, and 100 mM NaCl resulting in final protein concentrations of 5-12 μM. The concentrations were determined from three absorbance measurements at 280 nm using the theoretical Beer-Lambert Law extinction coefficient of 13,200 $M^{-1}cm^{-1}$. Spectra were measured on a J-810 Spectropolarimeter (Jasco Inc., Easton, MD, USA) at 25 ºC and averaged over 10 accumulations with a scanning speed of 100 nm/minute.

The relative aggregation property at higher protein concentrations was estimated by measuring the amount of protein remaining in the soluble fraction after incubation at 50 ºC. Specifically, 30 µl of 100 µM protein in 20 mM Tris, pH 7.5 and 100 mM NaCl were incubated on a 50 ºC heat block from 0 to 16 minute. Samples were subsequently centrifuged at 4ºC in an Eppendorf FA45-30-11 rotor (Eppendorf, Hauppauge, NY, USA) at 4000 RPM for 20 minutes. The level of protein in the soluble fraction was determined from absorbance at 280 nm. These experiments were repeated three times to estimate the average and the standard deviation of the residual protein concentrations.

5.2.3 NMR Experiments

All NMR experiments were performed on a Bruker Avance NMR spectrometer equipped with a cryogenic-probe (Bruker Biospin, Billerica, MA, USA) and operating at a ^{1}H Larmor frequency of 600.23 MHz. Protein samples for NMR experiments were

prepared in 25 mM Bis-Tris pH 6.5, 150 mM NaCl, 5 mM TCEP, and 0.02% $NaN_3$with 5% D_2O at protein concentrations ranging from 242 to 398 μM. ^{15}N-^{1}H heteronuclear single quantum coherence (HSQC) spectra of the WT, E412G, T441A, R560V, and C561A SERCA-N ^{15}N-labeled samples were recorded at 25ºC, unless otherwise noted. The HNCA spectra were recorded for $^{15}N/^{13}C$ isotope enriched WT and C561A SERCA-N for resonance assignment. For the mutants that exhibited ^{15}N-^{1}H HSQC spectra very similar to that of WT protein, the resonance assignments were estimated by placing the residue assignment from the WT spectrum with the closest peak in the mutant spectrum. ^{15}N-^{1}H HSQC spectra of E412G, T441A, R560V, and C561A SERCA-N were also recorded at different concentrations of AMP-PNP (Adenosine 5'-(β, γ-imido) triphosphate), ranging from 0 to 20 mM, at protein concentrations of 242 μM, 297 μM, 309 μM, 398 μM, and 242 μM respectively.

All NMR data sets were processed using NMRPipe (35) and analyzed using CARA (www.nmr.ch) (128) and NMRViewJ (One Moon Scientific Inc.) (95). The weighted net changes in chemical shift between the WT and mutants and those for changes on binding of AMP-PNP were obtained for the ^{15}N and ^{1}H dimensions using the equation: $\Delta\delta = \sqrt{\Delta\delta_H^2 + \left(\frac{\gamma_N}{\gamma_H}\Delta\delta_N\right)^2}$. Residues that showed $\Delta\delta$ values four times greater than the resolution were considered to have significant $\Delta\delta$. Dissociation constants were estimated from the changes in the $\Delta\delta$ as a function of AMP-PNP concentration.

Heteronuclear NMR experiments designed to determine ^{15}N R_2 transverse relaxation rates and $\{^{1}H\}$-^{15}N NOE (nuclear Overhauser effect) parameters were

recorded for the WT, T441A, and C561A SERCA-N mutants at 25ºC. Two-dimensional spectra were recorded for the mutant and WT proteisn at 7 or 8 relaxation-time points : 0, 8, 16, (24), 32, 48, 64, and 80 ms. The NOE values were determined using the ^{15}N peak intensity recorded in the presence and absence of 3 s ^{1}H saturation. Relaxation data were analyzed using in-house computer programs as described previously. (47) Other sample conditions and instrumental parameters were similar to those described in the main text.

5.3 RESULTS

5.3.1 Effect of Mutation on SERCA-N secondary structure

The WT and E412G, T441A, R560V, and C561A proteins could be expressed and purified with reasonable yields, ca. 20 mg/L culture. To confirm that the proteins were folded, CD spectra were recorded for all the mutants as well as for the WT SERCA-N. The spectra in the far-UV region of all the mutants showed an almost identical secondary structural content as the WT (**Figure 5.1**).

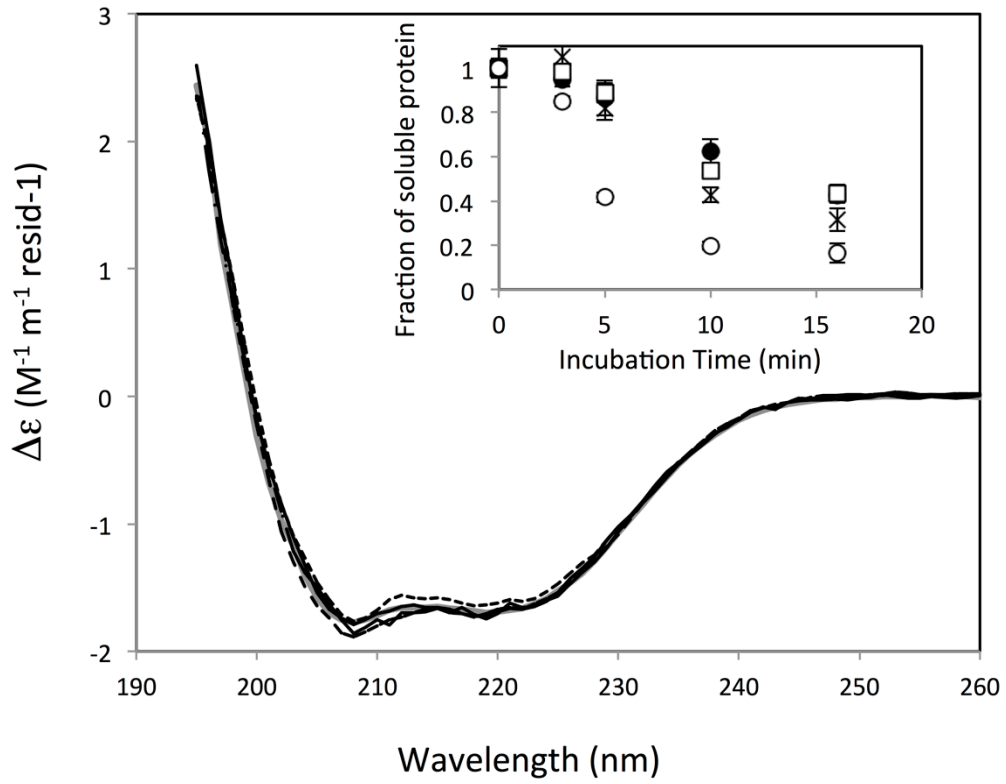

Figure 5.1 The Circular Dichroism spectra of the WT (gray solid line), E412G (dashed line), T441A (dotted line), R560V (dot-dashed line), and C561A (black solid line) SERCA-N in 20 mM Tris pH 7.5 and 100 mM NaCl at 25 ºC. Inset figure indicates qualitative estimate of protein stability recorded at 50 ºC for WT (black circle), T441A (open square), R560V (cross), and C561A (open circle) SERCA-N mutants (see Materials and Methods).

To determine whether the substitution mutations altered the thermal stability of the protein, we attempted differential scanning calorimetry. However, due to the precipitation of the samples at high temperature (data not shown), we were unable to obtain useful data. Therefore, thermal stability at high protein concentration (100 μM) was qualitatively evaluated by measuring the amount of soluble protein after incubation at 50ºC (**Figure 5.1**, inset). All SERCA-N constructs precipitated sooner than the WT. In particular, the C561A mutant had a greater tendency for precipitation despite the fact that the free cysteine residue was substituted to an alanine. The same experiment was

not performed for the E412G mutant, which precipitated even at 25ºC and showed small but significant differences in the signal position in the ^{15}N-^{1}H HSQC spectrum as described later (**Figure 5.2A**).

5.3.2 Effect of Mutation on SERCA-N Chemical Shifts

The WT SERCA-N ^{15}N-^{1}H HSQC spectrum was almost identical to the spectrum in the previous report by Ikura's group (2). The only notable differences were in a few residues located at the N-terminal end of the protein, for example T357 and T358, which could be due to the slightly altered sequence employed in our study (see the Materials and Methods). Assignments of backbone amide ^{1}H and ^{15}N of the 224 residue resonances were made for the WT protein using an HNCA spectrum and were confirmed by the chemical shift information from the previous study (2).

The ^{15}N-^{1}H HSQC spectra of the WT and mutant proteins exhibited similar patterns of resonance peaks (**Figure 5.2** and **5.3**), and are consistent with the similarity observed in the CD spectra, indicating that the basic fold of the protein is not altered by the mutations. This observation was also confirmed by ^{15}N transverse relaxation and $\{^{1}H\}$-^{15}N NOE experiments that provided similar profiles for the WT, T441A and C561A proteins (**Figure 5.4**). Amide signals in the ^{15}N-^{1}H HSQC spectra of T441A and R560V mutants almost completely overlapped with the WT protein, except for the region around the mutation sites; therefore, most of the backbone amide chemical shifts of the two mutants could be estimated based on the WT assignments (**Figures 5.2B** and **5.2C**, respectively). The HSQC spectrum of the C561A mutant also showed signals at similar positions to those of WT (**Figure 5.3**). However, since some of the C561A

signals showed no overlap with the WT (changes in chemical shifts $\Delta\delta$ ~ 0.3 ppm), an HNCA experiment was performed to assign signals (**Figure 5.2D**).

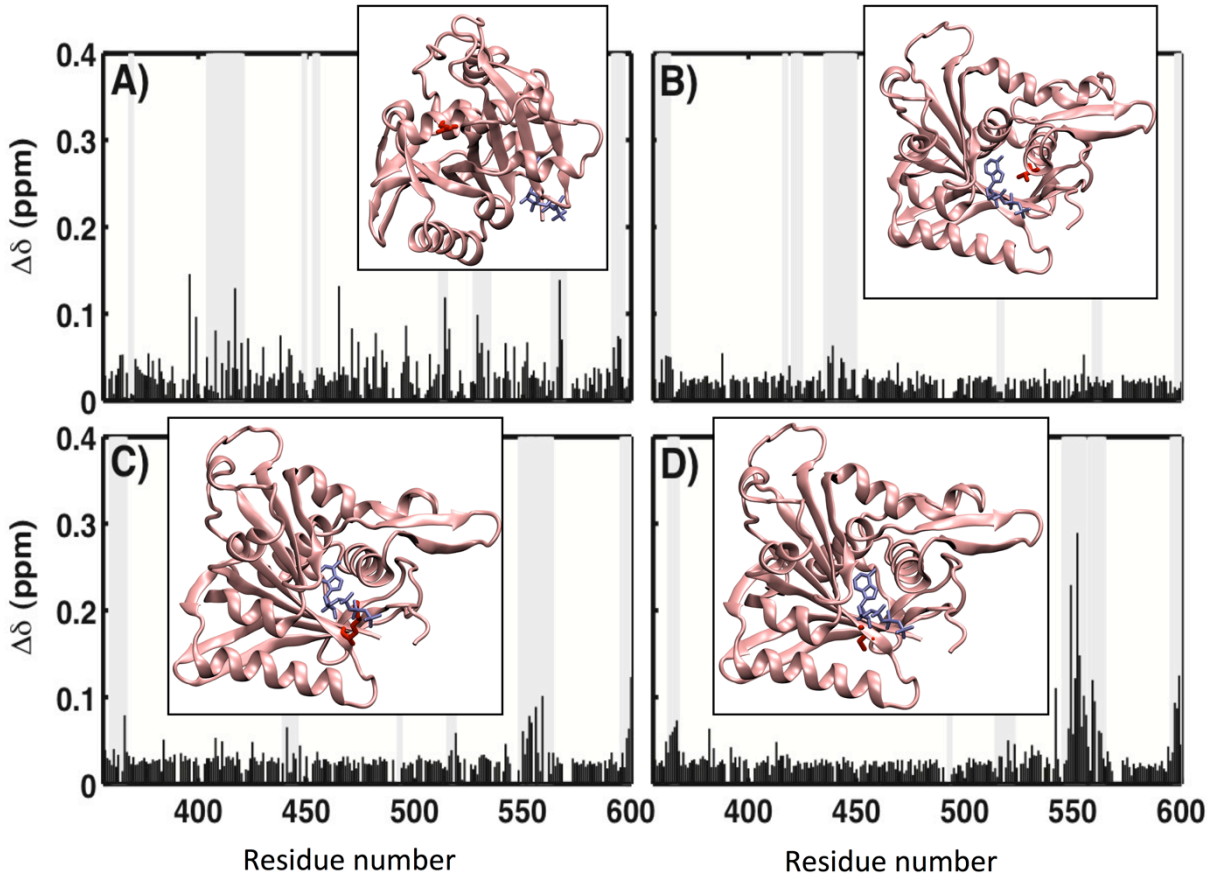

Figure 5.2 Differences in amide backbone chemical shifts, $\Delta\delta$, compared to WT SERCA-N for the (A) E412G, (B) T441A, (C) R560V, and (D) C561A mutants are shown with respect to the SERCA1a sequence numbering. The residues within 10Å of the mutation site are highlighted with gray background bars. Chemical shift changes above 0.0297 ppm are above the resolution of the spectra. In each graph, the mutation site is high-lighted in purple at the ribbon structure generated (Different views were selected for clarification) using PDB code 1IWO.

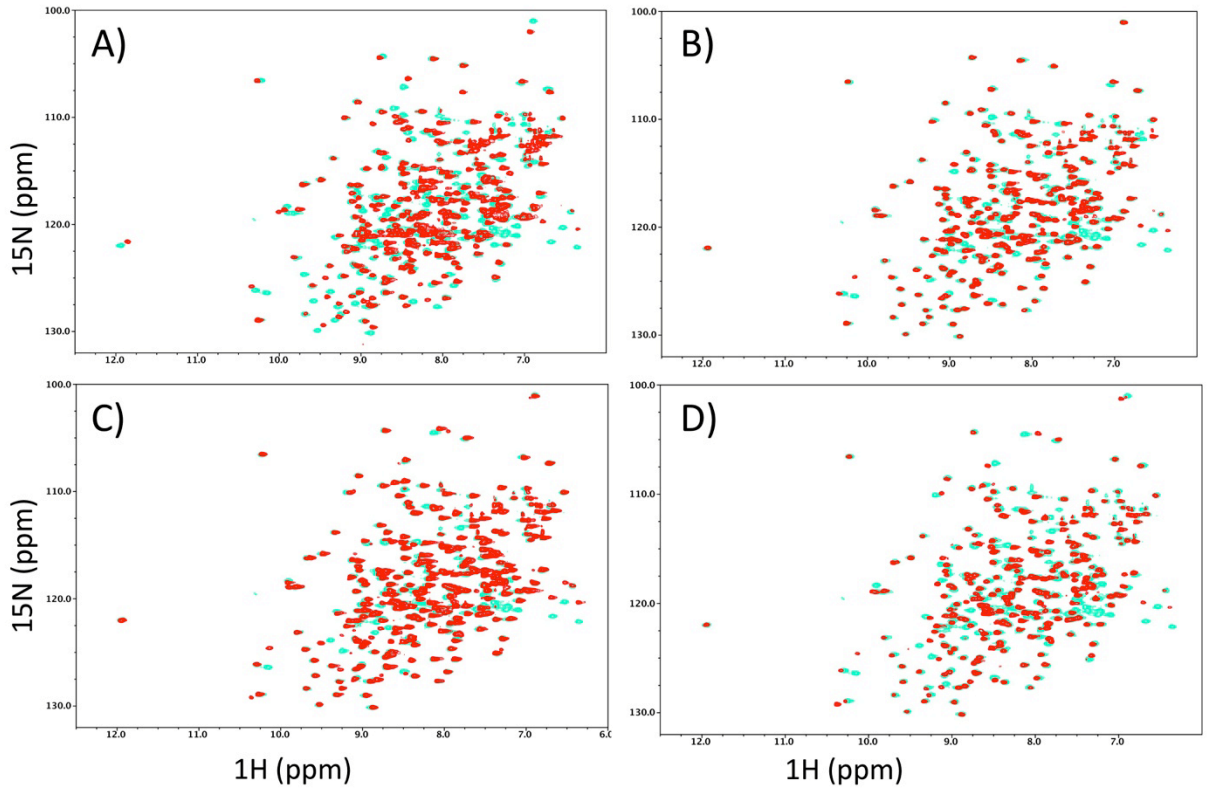

Figure 5.3 ^{15}N-^{1}H HSQC spectra of (A) E412G, (B) T441A, (C) R560V, and (D) C561A SERCA-N mutants (red) overlaid on that of WT (cyan).

E412G mutation caused moderate changes ($\Delta\delta$ < 0.15 ppm) in the ^{15}N-^{1}H HSQC signal positions throughout the protein compared to those of WT (**Figure 5.2A**). The protein sample precipitated significantly after a 2 hour during HSQC experiment at 25ºC. As described above, the CD spectrum of E412G is almost identical to that of WT. Thus, the observed changes in chemical shifts in the entire protein may be explained by a reduction in the thermal stability of the protein. In other words, the changes in chemical shifts are most likely due to the fast exchange between the major, folded form and the minor, unfolded form. Since the folded WT protein is stable and the mutation site is

located within the protein core, the observed precipitation is likely caused by the unfolded form.

5.3.3 Effect of Mutation on the ^{15}N Backbone Dynamics of SERCA-N

The{^{1}H}-^{15}N NOE data basically decreased due to internal motion faster than the molecular rumbling rate (>ns). ^{15}N $R_{2,}$ also decreased by the internal motion,increased when conformational equilibrium in the milli- to microsecond time scale was reached, inducing a chemical exchange phenomenon in the NMR spectra.

^{15}N R_2 and NOE data for SERCA-N WT were consistent with those published previously (3).The data acquired for T441A and C561A were similar to those of the WT (**Figures 5.4 and 5.5**), indicating no significant difference from the WT in terms of nanosecond-picsecond(ns-ps) backbone dynamics. AMP-PNP binding did not induce significant changes in dynamics, as was observed in the previous NMR study (3). In addition, the T441A and the C561A mutants both showed no significant difference from the WT in terms of ns-ps backbone dynamics. These results are consistent to the observation of chemical shift changes upon AMP-PNP interaction and support the results shown in **Figures 5.6** and **5.7**.

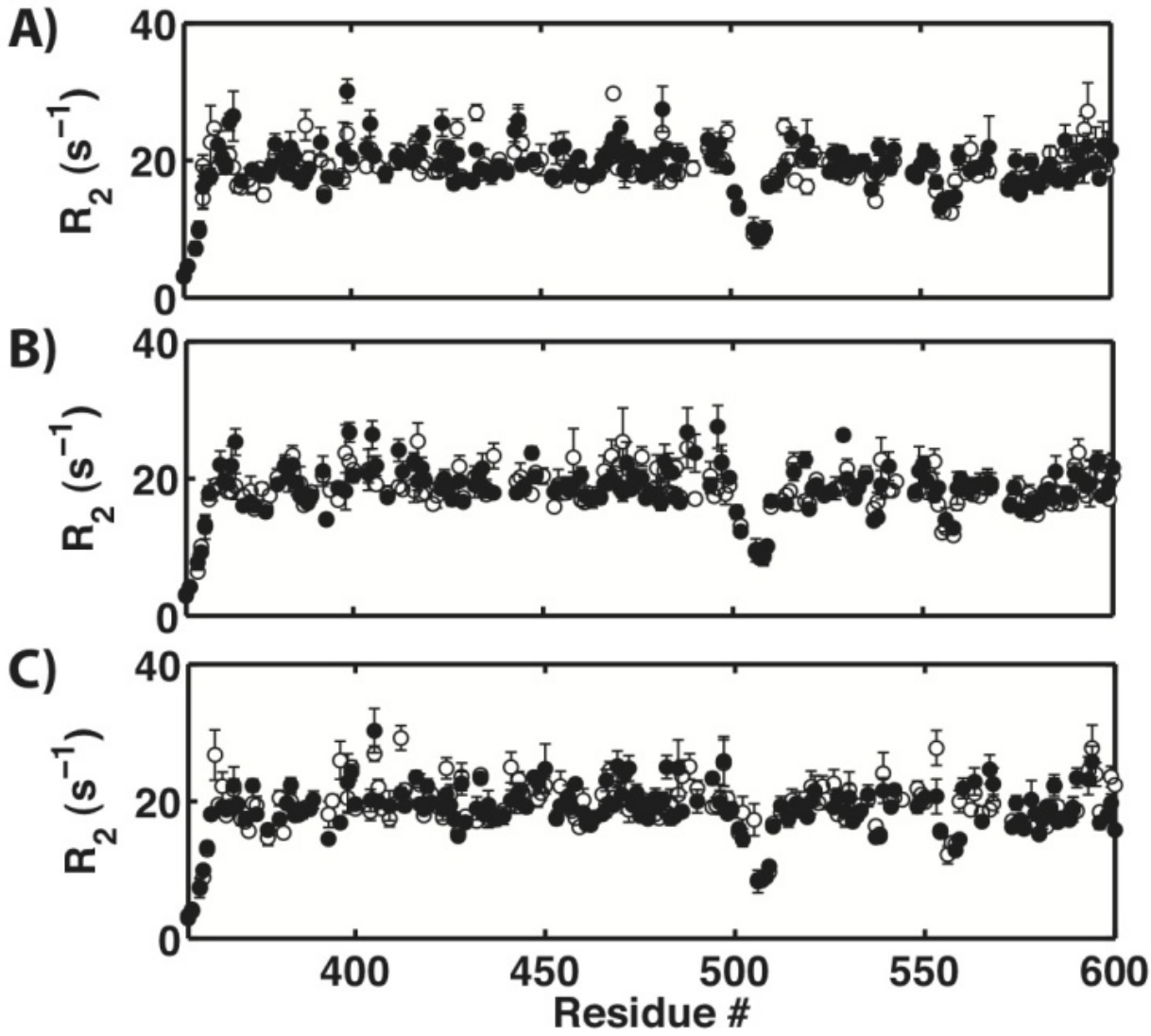

Figure 5.4 The backbone (A) transverse relaxation rates, R_2, for the A) WT, B) T441A, and C) C561A SERCA-N mutants in the presence (open circles) and absence of (closed circles) 10 mM AMP-PNP.

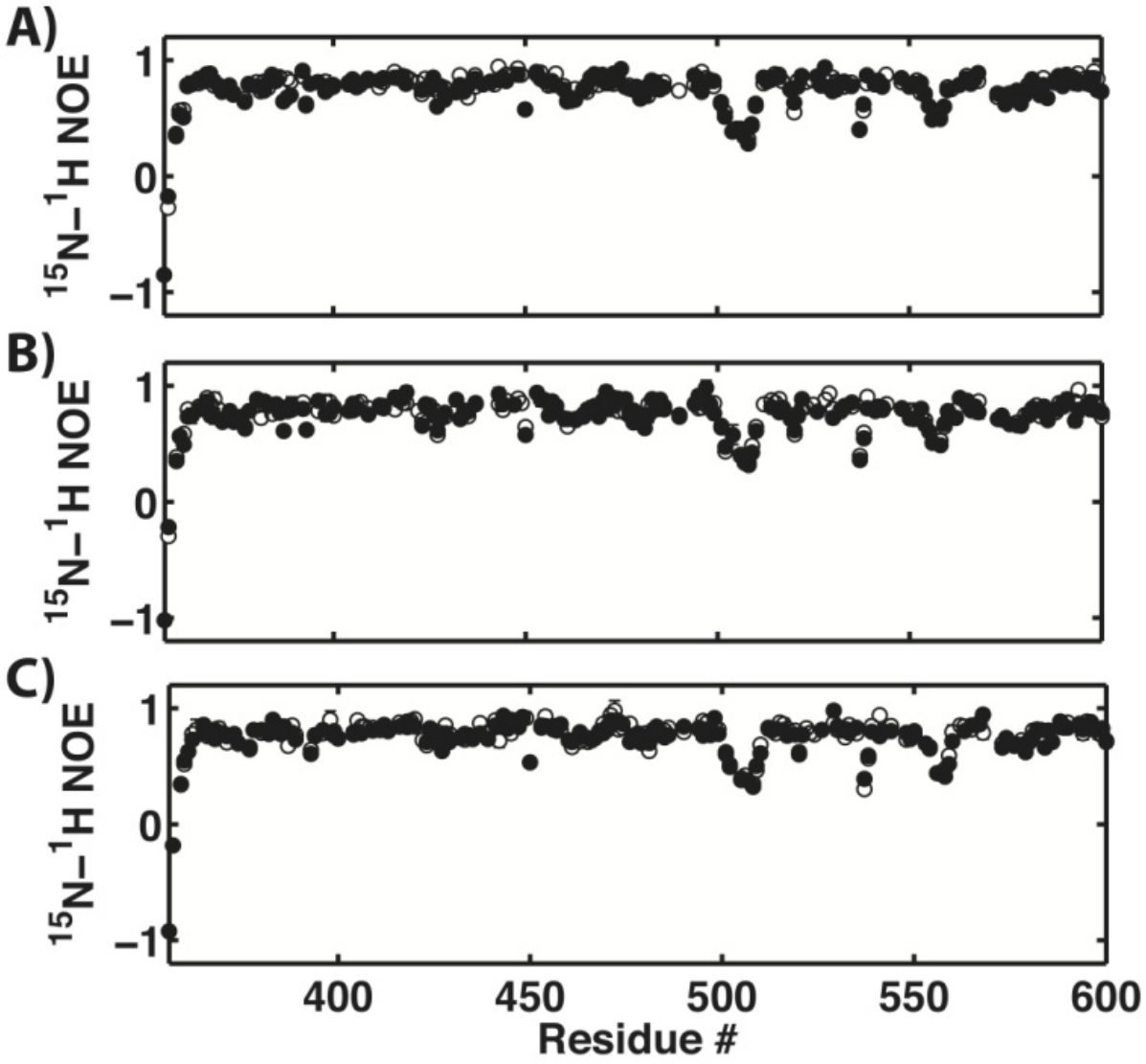

Figure 5.5 The backbone {^{1}H}-^{15}N NOE for the A) WT, B) T441A, and C) C561A SERCA-N mutants in the presence (open circles) and absence of (closed circles) 10 mM AMP-PNP.

5.3.4 Effect of Mutation on AMP-PNP binding

To determine whether the nucleotide binding affinity or binding site is altered by the various mutations, ^{15}N-^{1}H HSQC spectra were recorded at varying concentrations of AMP-PNP, chosen to allow direct comparison of our WT results with those obtained in

the previous report (2). Signal positions in the NMR spectrum of the WT were shifted upon AMP-PNP titration (**Figure 5.6A**), indicating that the exchange is in the fast exchange condition (i. e. the exchange rate is faster than the difference in chemical shifts between the free and bound forms). Significant shifts were observed for residues S423, T441, E442, S488, D490, M494, S495, A517, and L562 (**Figure 5.6A**), all located in the nucleotide-binding pocket. These observations are consistent with those made previously by Ikura's group (2). However, upon close inspection of the spectra, additional residues were found to be perturbed in response to AMP-PNP binding. These residues included T447 and R476, which are located far from the binding site, approximately 14 Å and 17Å, respectively, indicating long-range effects of the nucleotide binding (**Figure 5.7A**).

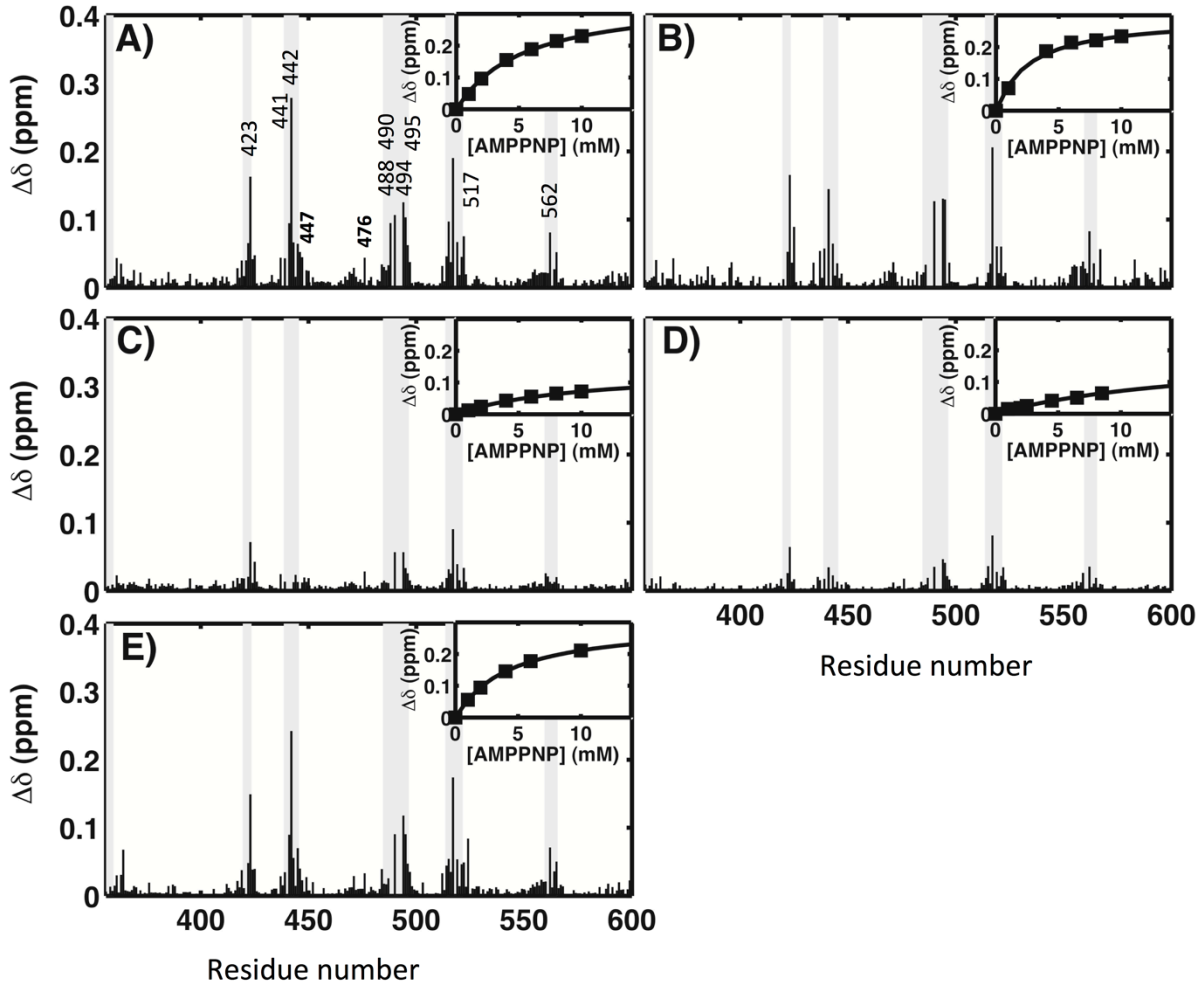

Figure 5.6 Differences in amide backbone chemical shifts, Δδ, between proteins in the presence of 10 mM AMP-PNP and in the absence of AMP-PNP for the (A) WT, (B) E412G, (C) T441A, (D) R560V, and (E) C561A SERCA-N. The residues within 10Å of the nucleotide binding site are highlighted with gray background bars. Note that at 10 mM AMP-PNP, the fraction of protein bound to AMP-PNP are 65.8, 79.9, 51.3, <49.5, and 72.0%, respectively. Insets show the changes in the Δδ as a function of AMP-PNP for residue S423 (black squares).

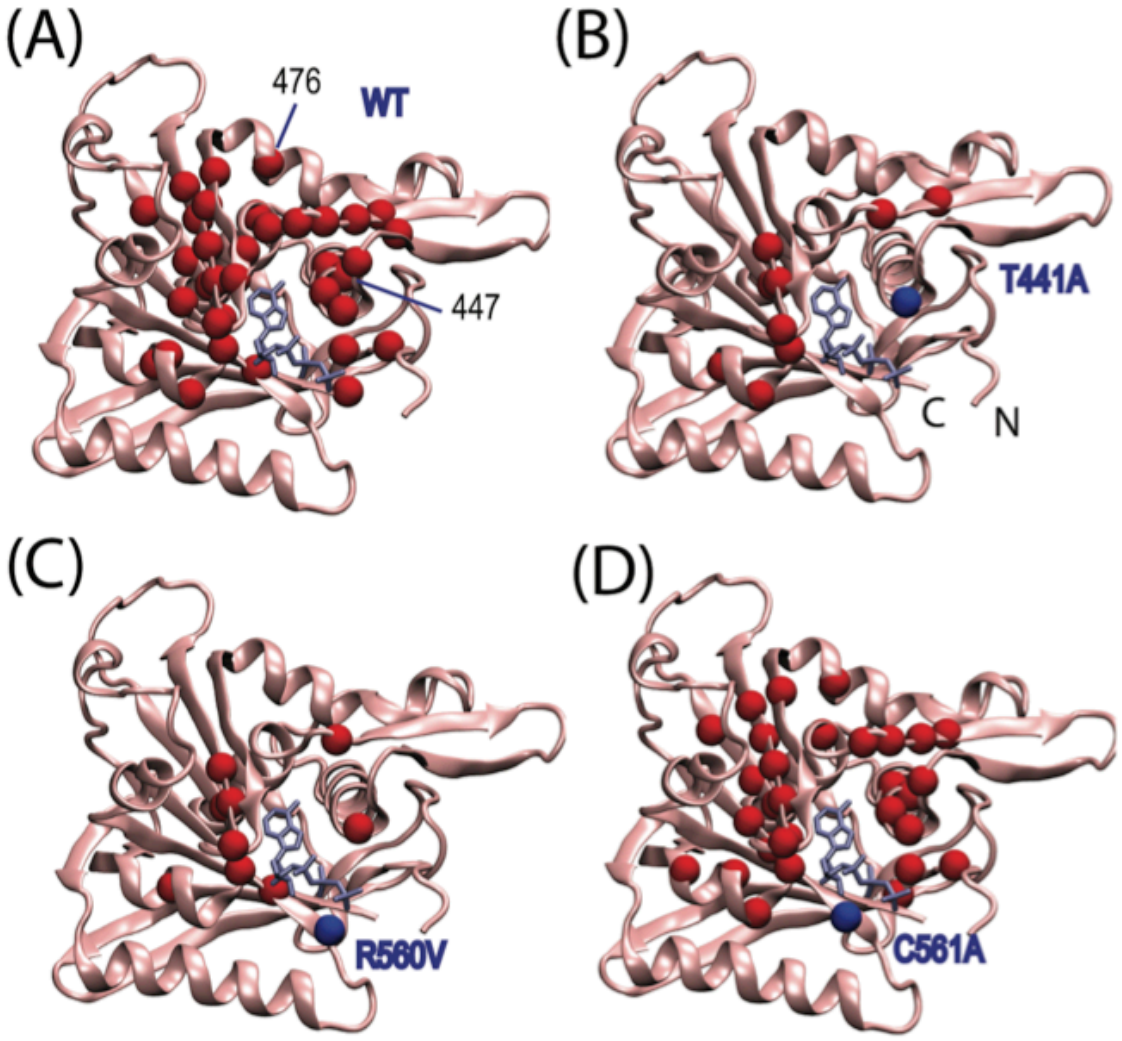

Figure 5.7 Illustration of residues (red spheres) with significant chemical shift changes, Δδ, upon AMP-PNP binding on a SERCA-N structure (PDB ID: 1IWO) for the (A) WT, (B) T441A, (C) R560V, and (D) C561A mutants. A significant change is considered to be two-fold of standard deviations above the average Δδ. In B, C, and D, the mutated residues are highlighted as blue spheres. The mapping was not made for the E412G mutant, which exhibited moderate chemical shift changes but was not be assigned due to the instability of the sample.

Using the NMR titration data (**Figure 5.6**, inset), the AMP-PNP dissociation constant, K_D, for the WT protein was estimated to be 5.1 ± 0.8 mM at 25 °C, which is close to the previous estimation by NMR (~2.4 mM, (3)) but larger than the ATP

dissociation constant (0.7 mM, (27)). The ATP dissociation constant for the WT protein was determined to be 1.3 ± 0.2 mM (data not shown), very similar to that observed previously.

The AMP-PNP K_D value for the C561A mutant was similar to the WT at 3.80 ± 0.22 mM at 25 °C (Fig. 3E). The K_Ds for the T441A and R560V mutants were smaller than the WT at 9.30 ± 0.54 mM and > 10 mM, respectively, at 25 °C (**Figure 5.6C** and **5.6D**). These tendencies of AMP-PNP dissociation are consistent with the reported reductions in the ATPase activities (100%, 50%, and 30% of WT for C561A, T441A, and R560V, respectively) (29). The K_D for E412G mutant was estimated to be 2.5 ± 0.2 mM (at 10 °C, to avoid precipitation). Although it cannot be quantitatively compared to that of WT, it is noteworthy that the E412G mutant can bind to AMP-PNP at a qualitatively similar level at low temperature.

5.4 DISCUSSION

Although mutations that affect the ATPase activity in the SERCA-N domain have been identified (92; 29; 129), the structural consequences of the mutations have not been reported. The results of this study provide insight into the structure-function relationship of the SERCA ATPase.

The CD spectra (**Figure 5.1**) and the HSQC chemical shift data (**Figure 5.2**) of the T441A, R560V, and C561A SERCA-N mutants indicate that little structural perturbation is present in the mutant proteins. Based on the fact that these mutations did not completely abolish the catalytic activity (29), our observation of such small

structural effects is reasonable. Crystal structure studies and NMR studies have shown that the SERCA-N domain does not undergo major conformational changes upon nucleotide interaction (193; 149; 182; 148; 114; 192; 203); root mean square deviation (RMSD) of the backbone Cα in the SERCA-N is only 0.6 Å between the E1 and E2 states (calculated using structures of the PDB codes, 3BA6 and 3B9B). Our results confirm that nucleotide binding by these mutants also results primarily in local conformational change, at the binding sites (**Figures 5.6** and **5.7**). However, small but significant long-range effects were observed upon AMP-PNP binding in both WT and the mutants (**Figure 5.7**), indicating that re-adjustment of the structure occurs in the protein core in the domain study level.

In contrast to these mutants, E412G mutation caused severe protein precipitation at 20 °C. Nevertheless, our data demonstrate that the E412G mutant can bind to AMP-PNP with a similar pattern of chemical shift changes to that of WT at lower temperature suggesting that the E412G mutation may not abolish the nucleotide binding activity. Since the E412G mutation does not cause heart dysfunction (170; 167; 36), it is reasonable that the E412G mutant still maintains the nucleotide binding activity. However, the E412G mutation is found in the patients with Darier's disease. It has been expected that an alternative mechanism exists to rescue the Ca^{2+}-ATPase function in cardiac muscle (170; 172; 167; 189; 36; 129; 133). Based on the current results, we propose that such shift of the equilibrium between the native and denatured forms could be rescued by shifting back the equilibrium by other factors.

The C561A mutant exhibited relatively localized changes on chemical shifts compared to the WT protein (**Figure 5.2D**). As described above, such small changes

are similar to those of T441A and R560V. However, the C561A mutant has an equivalent AMP-PNP K_D to that of WT (**Figure 5.6E**) and precipitates faster than the T441A, R560V, and WT proteins (**Figure 5.1, inset**). Although significant chemical shift changes throughout the protein were not observed for the C561A mutant, these propensities of C561A mutation are somewhat analogous to those of E412G. Based on this point, the instability of the C561A may relate to the mechanism to maintain the ATPase activity but only causes slight reduction of the Ca^{2+} transport (29).

5.5 CONCLUSIONS

In this study, we investigated the effect of both substrate binding site mutations (T441A, R560V, and C561A) (29) as well as a mutation observed in patients with Darier's disease (E412G) (167). The major biological question investigated was why the E412G mutant leads to a skin disorder but not to heart failure and SERCA dysfunction(129). Although the secondary structure of all mutant forms and the WT form were observed to be similar, differences in the thermodynamics of the proteins were found to be different based on precipitation assays. In addition, NMR experiments revealed that the E412G mutant shows significant chemical shift (backbone amide ^{1}H and ^{15}N resonances) differences from WT throughout the entire protein sequence while the T441A, R560V, and C561A mutants showed only chemical shift differences from WT near the site of mutation. Since the K_D parameter for the E412G mutant was found to be similar to the WT while other active site mutants T441A and R560V were found to have significantly higher K_D values, it is likely that the E412G mutant retains ATP

binding affinity as the WT. The C561A mutant was also found to have similar K_D as the WT and E412G mutant and this likely reflects the less severe effect on protein function (observed by biochemical assays) compared to the T441A and R560V mutants (29). Due to the decreased protein stability (as observed from large chemical shift difference from WT throughout the protein and precipitation of the protein) and the retention of the ligand binding affinity, it is likely that the E412G mutant retains function as in WT, preventing heart failure, but may have stability differences that leads to Darier's disease in skin cells.

6.0 DIFFERENTIAL FLAP DYNAMICS IN WILD-TYPE AND A DRUG RESISTANT VARIANT OF HIV-1 PROTEASE REVEALED BY MOLECULAR DYNAMICS AND NMR RELAXATION

In the rapidly evolving disease of HIV drug resistance readily emerges, nullifying the effectiveness of therapy. Drug resistance has been extensively studied in HIV-1 protease where resistance occurs when the balance between enzyme inhibition and substrate recognition and turn-over is perturbed to favor catalytic activity. Mutations which confer drug resistance can impact the dynamics and structure of both the bound and unbound forms of the enzyme. Flap+ is a multi-drug-resistant variant of HIV-1 protease with a combination of mutations at the edge of the active site, within the active site, and in the flaps (L10I, G48V, I54V, V82A). The impact of these mutations on the dynamics in the unliganded form in comparison with the wild-type protease was elucidated with Molecular Dynamic simulations and NMR relaxation experiments. The comparative analyses from both methods concur in showing that the enzyme's dynamics are impacted by the drug resistance mutations in Flap+ protease. These alterations in the enzyme dynamics, particularly within the flaps, likely modulate the balance between substrate turn-over and drug binding, thereby conferring drug resistance. The results presented in this chapter have been published in *Journal of*

Chemical Theory and Computation, 2012, 8:3452-3462. In this chapter, my major contributions are in the experimental portion.

6.1 INTRODUCTION

Acquired immunodeficiency syndrome (AIDS) has become a worldwide, public health threat since 1980s. The AIDS patient's immune system is weakened by infection with the human immunodeficiency virus (HIV-1). Maturation of HIV-1 virus requires the viral protease to cleave the Gag and Gag-Pol polyproteins to release the structural proteins MA, CA, NC and p6, and the enzymes reverse transcriptase (RT), integrase (IN) and protease (PR)(43). HIV protease is a crucial target for drug design in AIDS therapy, due to this critical role in the life cycle of HIV-1.

Since HIV-1 protease is an important drug target for HIV-1 therapy, there has been substantial effort in developing protease inhibitors as drugs. Nine protease inhibitors have been approved by the FDA for clinical use in fighting AIDS, leading to a significant decrease in the death rate due to AIDS. However, due to the high replication rate of the virus and lack of proofreading mechanism of its reverse transcriptase, selective pressure of drugs leads to rapid emergence of many drug-resistant protease variants.

HIV-1 protease is a homodimeric aspartyl protease with 99 amino acids on each subunit (**Figure 6.1**). The dimer interface is a network of hydrogen bonds of an intertwined beta-sheet between the N- and C-terminal regions of each monomers and the active site. Each monomer also has a glycine rich flap: K45-M-I-G-G-I-G-G-F-I-K55.

This flap folds as an anti-parallel β sheet that covers the active site. Since the flaps modulate access to the active site, the flexibility of this region is crucial for enzyme activity and inhibitor binding. Unlike the fully closed conformation in complexes of the protease with inhibitor/substrate, the flaps in crystal structures of the apo protease adopt a “semi-open” conformation (113; 205; 183; 204; 68), which may be due in part to crystal packing constraints. The entrance of substrates or inhibitors to the active site requires further conformational changes of the flaps.

The flexibility of the flaps in unliganded protease has been studied by a combination of experimental (fluorescence, EPR and NMR) (50; 168; 83; 46; 121; 54; 84; 53; 55) and computational methods (174; 161; 73-75; 24; 151). NMR relaxation experiments on the apo form of wild type (WT) protease have previously indicated that the flap region is mobile on a microsecond time scale with the flap tip (48G-G-I-G-G52) having an even higher degree of mobility on a sub-nanosecond time scale (83). MD simulations coupled with experimental techniques have attempted to described how this motion might occur, i.e. whether the flaps curl in or extend out (174; 55).

The structural basis for drug-resistance has been extensively studied in HIV-1 protease. Comparison between the structures of WT and drug-resistant proteases in complex with inhibitors partially elucidated how specific protease mutations decrease protease-inhibitor binding affinity on the atomic level (164; 111; 165; 102; 103; 5; 11). However, static crystal structures do not provide insights into the mechanisms by which mutations can change the dynamic properties of the protease. MD simulations have suggested the role of mutations outside the active site of the protease in altering the

internal dynamics of the flaps and the hydrophobic core and thereby modulating drug resistance (174; 45)

Flap+ is a multi-drug-resistant HIV-1 protease variant with a combination of flap and active site mutations (L10I, G48V, I54V, and V82A) that occur simultaneously in sequences of patients undergoing drug therapy (**Figure 6.1**) (175). Thermodynamic analysis of inhibitor binding to Flap+ protease revealed a surprising entropy-enthalpy compensation phenomenon with the enthalpy and entropy of binding difference between the WT and Flap+ variants (the $\Delta\Delta H_{WT\text{-}Flap+}$ and $-\Delta(T\Delta S_{WT\text{-}Flap+})$) being -14.1 ± 1.1 kcal/mol and 13.1 ± 1.1 kcal/mol, respectively, while the total free energy being almost identical($\Delta\Delta G_{WT\text{-}Flap+}$, -1.0 ± 0.3 kcal/mol) (101). Flap+ exhibits extremely large and opposite changes in the entropy and enthalpy of binding compared to WT protease, indicating that the drug resistance mutations in Flap+ directly modulate the relative thermodynamics of inhibitor interactions. In a previous study we examined the energetics of inhibitor binding (24; 23) however, the molecular mechanisms that cause these thermodynamic changes, and how protease dynamics might be altered in Flap+ protease had not been addressed.

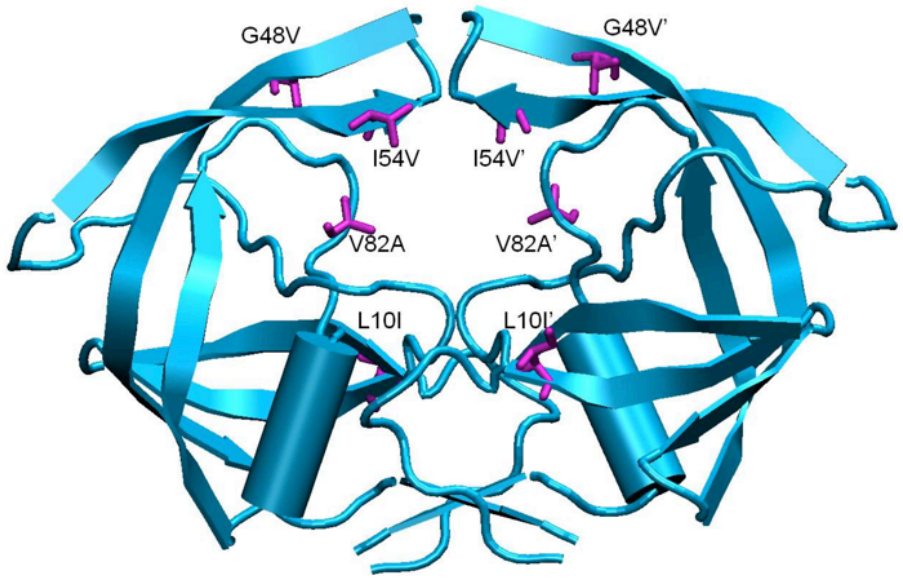

Figure 6.1 Drug-resistant HIV-1 protease variant Flap+. Mutations are highlighted in magenta.

In this study we investigate and compare the dynamics of apo WT and Flap+ protease through a combination of molecular dynamics (MD) simulations and NMR relaxation experiments. Combining MD with experimental NMR data, spearheaded by many seminal developments of the van Gunsteren laboratory (184; 32; 194; 196), has been a powerful method in understanding the atomic basis for the experimental motions observed. The results of this comparative analysis show that the flap dynamics are altered due to the drug resistance mutations in the Flap+ variant. Such changes in the flap dynamics may be modulating the access of substrates and inhibitors to the protease active site.

6.2 METHODS AND MATERIALS

6.2.1 ^{15}N labeled protease expression, purification and refolding

HIV-1 protease was expressed in *Escherichia coli* strain *BL21-Gold*(*DE3*)*pLysS* competent cells using a T7 expression system. For this experiment, protease that contains mutations at the primary auto-proteolysis site and at cysteine sites (Q7K, L33I, L63P, C67A and C95A) were used (reference: Louis, Clore, Gorenborn, 1999, Nat Struct Biol, 6, 868-875):

PQITL WKRPL VTIRI GGQLK EALLD TGADD TVIEE MNLPG KWKPK MIGGI

GGFIK VRQYD QIIIE IAGHK AIGTV LVGPT PVNII GRNLL TQIGA TLNF

This sequence contains additional 3 natural variant mutations (S37N, K14R, K41R) compared to the one used in the MD simulation. Protease was overexpressed and purified using the protocol published previously (ref: paper from Schiffer's lab). In brief, the bacteria were grown in LB or TB media at 37°C. When OD_{600} value of the culture reached 0.4, the bacteria were separated from the LB culture by centrifugation. The pellet was resuspended in 1 L cold (4°C-10°C) wash buffer. The bacteria were separated from the wash buffer by centrifugation and resuspended in 250 mL M9 ^{15}N minimal medium (127). After growing the M9 bacterial culture at 37°C for 10 to 20 min, protease expression was induced with 2 mM IPTG for 4 hours. After induction, the culture was centrifuged and the bacteria pellet was separated and stored at -80°C. The protease was contained in the inclusion body in the bacterial pellet. After the bacterial cells were lysed, the inclusion bodies were isolated by centrifugation and the pellet was dissolved in 50% acetic acid to extract protease. Protease was purified by separating

proteins with different molecular weight by size exclusion chromatography on a 2.1 L Sephadex G-75 superfine column with 50% Acetic Acid. As described above, Flap+ contains additional mutations of L10I, G48V, I54V, and V82A, and was expressed and purified similar to that of the WT.

6.2.2 NMR Sample Preparation

For NMR sample preparation, the purified protein was dialyzed against 20 mM formic acid at pH 2.7. The protein was folded in the presence of 10 mM acetate solution at pH 6.0, and the buffer was exchanged to 20 mM sodium phosphate at pH 5.8, as described previously (89). Prior to this step, protein that underwent partial auto-proteolysis was re-purified by reversed-phase HPLC with a Resource RPC 3 mL column (GE Healthcare) equilibrated with 0.05% trifluoroacetic acid (v/v), and eluted with 80% acetonitrile and 0.05% trifluoroacetic acid (v/v). The protein was concentrated to 150 $\pm$ 25 μM as a dimer. The NMR samples were in 20 mM sodium phosphate buffer in 95% H_2O/5% D_2O at pH 5.8, and placed in a Shigemi tube (Shigemi Inc., Allison Park, PA).

6.2.3 NMR data acquisition and model free analysis

NMR experiments to determine ^{15}N transverse relaxation rate (R_2), ^{15}N longitudinal relaxation rate (R_1), and ^{15}N-^{1}H heteronuclear Nuclear Overhauser Enhancement (hNOE) were performed using Bruker Avance 600 MHz NMR spectrometers equipped with a cryogenic probe at 20°C for the WT and flap mutant (46; 82). In the R_1 and R_2 experiments, spectra were recorded with 7 relaxation delay points:

0, 8, 16, 24, 32, 48, and 64 ms for R_2, and 0, 50, 100, 200, 300, 500, and 800 ms for R_1. The relaxation rates were determined by fitting the signal intensities to a single-exponential decay function that has two unknown parameters, initial intensity (I_0) and relaxation rate (R_1 or R_2). Uncertainties of the R_1 and R_2 values were estimated by Monte-Carlo error simulation using residual of the fits as data uncertainties. The $\{^1H\}$-^{15}N NOE values were determined using the ratio of the two peak heights that were recorded with and without NOE enhancement, and NOE ratio error was estimated from the 2-dimensional peak noise error.

Rotational correlation times of the WT and the flap mutants were determined by assuming a single rotational correlation time, τ_R, for each protein. First, τ_R was optimized by a grid search by fitting the parameter sets of a standard model-free model (that contains two unknown parameters, the generalized order parameter, S^2, and a correlation time for internal motion, τ_i) for a group of residues (42). For this determination, a group of residues that exhibit R_1 and R_2 values within 1.5 standard deviation of the mean, and $\{^1H\}$-^{15}N NOE > 0.69 were selected. Next, once τ_R was determined, the model-free analysis was performed primarily using the standard model (S^2, τ_i) for all the residues for which a set of R_1, R_2, and $\{^1H\}$-^{15}N NOE was available (116; 117; 125). For the data that did not fit to the standard model (with criterion χ^2 > 6.64 (46)), models with three parameters, extended model free (S^2_f, S_s^2, τ_i) and exchange model (S^2, τ_i, R_{ex}), were tested (30). Here, $S^2 = S_f^{\,2} \cdot S_s^{\,2}$ with order parameters for fast (f) and slow (s) internal motions, and R_{ex} indicates contribution of chemical exchange to R_2. Finally, when the dataset for a particular residue either in WT or Flap+ were not fit by the standard model and instead fit using a three-parameter

model, the dataset for that residue in the other construct was also analyzed using the same model. This minimized possible model-dependent artifacts in the comparison of WT and Flap+. In the entire model-free analysis, minimum uncertainties of all R_1, R_2, and $\{^1H\}$-^{15}N NOE were set at 4% to avoid underestimation of the systematic errors in the relaxation rates.

6.3 RESULTS

Protein dynamics, structure, and function are highly correlated. In the case of HIV protease, the dynamics of conformational changes are extremely critical for enzyme function. The first step in the HIV-1 protease substrate-cleavage reaction is opening of the protease flaps to expose the active site cleft to the substrate. This conformational change is highly related to the flexibility of the flaps of the protease. The impact of drug-resistance mutations on the apo form of the Flap+ multi-drug resistant variant on the dynamics and flexibility was compared with the WT enzyme by NMR experiments. In addition, MD simulation results by collaborators were compared to the NMR data. Although the protease sequence used for the NMR experiments contain a total of 9 minor mutations (minor variants) compared to that used in MD simulations by collaborator, the relative change in dynamics between WT and Flap+ dynamics will be compared in two methods.

6.3.1 Comparison of Dynamics with NMR

Flap dynamics is critical to protease function, and has previously been investigated by NMR relaxation (83; 46; 84) and site-directed spin labeling experiments (54; 53; 55). To understand the dynamic differences between the WT and Flap+ protease, especially in the flap region, the enzyme was also evaluated by high resolution NMR. For this purpose, the transverse relaxation rate (R_2), the longitudinal relaxation rate (R_1), and the ^{15}N-^{1}H heteronuclear Nuclear Overhauser Enhancement (hNOE) were measured. These relaxation parameters reflect internal motion of the ^{15}N-^{1}H bond vectors and provide information on the backbone dynamics at the residue-specific level.

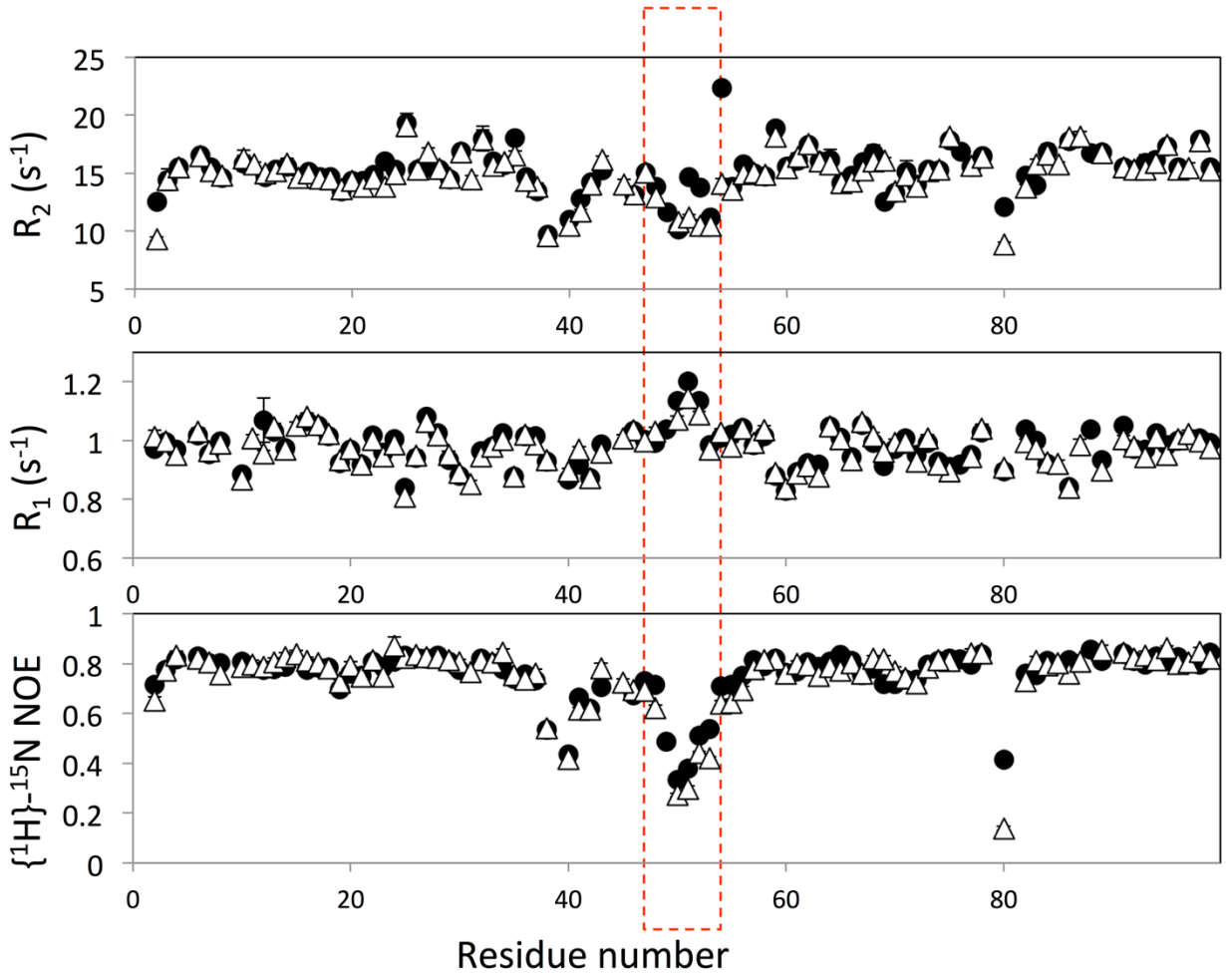

Figure 6.2 NMR relaxation data for WT (filled circles) and Flap+ HIV-1 Protease (open triangles). The red dashed square (residues 47 to 54) indicates the flap region.

Overlay of R_2, R_1, and {^{1}H}-^{15}N NOE data for the WT and the mutant protease demonstrates that the relaxation data for most of the residues in the mutant are very similar to those of the WT, indicating that overall dynamics of the protein core is not affected by the mutations (**Figure 6.2**). This result is consistent with crystal structures of Flap+ mutant (101) being globally similar to the WT protease.

A close look at the relaxation data shows that residues 47-54, which form the tip of the flap, show significant differences in R_2 and {^{1}H}-^{15}N NOE parameters between the

WT and the flap mutant (**Figure 6.2**). The R_2 and $\{^1H\}$-^{15}N NOE values for residues 48, 51, and 52 of the mutant are lower, indicating that the flap region of Flap+ undergoes more significant sub-nanosecond motion than that of the WT. In addition, the invariant Thr 80 (45), which is flanked by proline residues (Pro 79 – Thr 80 – Pro 81), has higher mobility in the mutant.

The experimentally measured relaxation parameters were subjected to model-free analysis to determine the internal dynamics of the protein backbone independent of the overall motion of the protein (116; 117). Model-free analysis takes as input the experimentally measured relaxation parameters (R_1, R_2, and ^{15}N-^1H hNOE) and outputs the generalized order parameter, S^2, which represents the spatial restriction of motion of the ^{15}N-^1H bond vector (116; 117). As S^2 approaches 1, the bond vector undergoes no significant internal motion. As S^2 approaches 0, the bond vector undergoes unconstrained internal motion. The standard model-free analysis assumes two types of motion on sufficiently different time scales that they are independent: local internal motion on the fast time scale (sub-nanosecond) and the slower global motion of the protein. The time scales for these two independent motions are also output as τ_l for each bond vector, and the global rotational correlation time of the protein, τ_R.

Data for most of the residues in WT and Flap+ protease were fit using the standard model (**Table 6.1**). The rotational correlation time τ_R was determined to be 12.52 ± 0.26 ns and 12.48 ± 0.32 ns for the WT and the FLAP+ HIV-1 protease variants, respectively. An axially symmetric model was not used to estimate molecular rotational correlation times, because no particular NH vector orientation can be assumed for the amides at the very flexible flap region. Data sets that do not fit adequately to the

standard model were analyzed using either [1] the extended model with an additional generalized order parameter for slower internal motions on the nanosecond time scale, S^2_s (12), or [2] the chemical exchange model that includes an additional parameter to account for chemical/conformational exchange mostly on the microsecond-millisecond time scale (125). To avoid possible artifacts due to selection of the models, the same model was used for each residue in both the WT and the Flap+ protease, if the dataset was available for both constructs (**Table 6.1**).

Table 6.1 The number of residues for which the relaxation data was analyzed by the given model in model-free analysis.

Model	WT and Mut[#]	WT only[##]	Mutant only[##]
Standard model (S^2 and τ_i)	53	3	5
Extended model (S^2_f, S_s^2, τ_i)	12	2	0
Exchange model (S^2, τ_I, R_{ex})	14	0	1

When an R_2, R_1, and $\{^1H\}$-^{15}N NOE dataset of a residue from one of the two proteins required an extended or exchange model, the dataset from the other protein was analyzed using the same model.

"Only" indicates that an R_2, R_1, and $\{^1H\}$-^{15}N NOE dataset was obtained only for one of the proteins for a residue.

The order parameters obtained through model free analysis are overall very similar for WT and Flap+ protease (**Figure 6.3**), as expected due to the similarity in the measured relaxation data (**Figure 6.2**). The major difference in the order parameters is the lower values for residues in the flap (48, 51, 52 and 43) as well as residue 80 in the

mutant enzyme, indicating higher mobility of flaps in the Flap+ protease in the sub-nanosecond time scale. Additionally, flap regions in both WT and the mutant exhibit significant internal motions (τ_i) on the nano-second time scale. While the results unequivocally demonstrate that the flap dynamics are altered in the Flap+ protease compared to the WT, it should be noted that the parameters from model free analysis presented here may not be sufficient to reflect the complex flap dynamics. The relatively high order parameters for the WT flaps may be due to the insufficient separation of R_{ex}, the chemical/conformational exchange contribution to the measured R_2. The flaps in WT protease undergo milli-microsecond motions (revealed by CPMG-based NMR relaxation experiments (83; 46)), which would give rise to conformational exchange on the NMR timescales and hence R_{ex}. However, the R_{ex} term could not be extracted by the model-free analysis. This is because the flap region of the WT protease undergoes severe sub-nanosecond motions as well as the milli-micro second motion, and no appropriate model (such as both extended and with chemical exchange) is available to describe the range of motions the flaps undergo in various time scales.

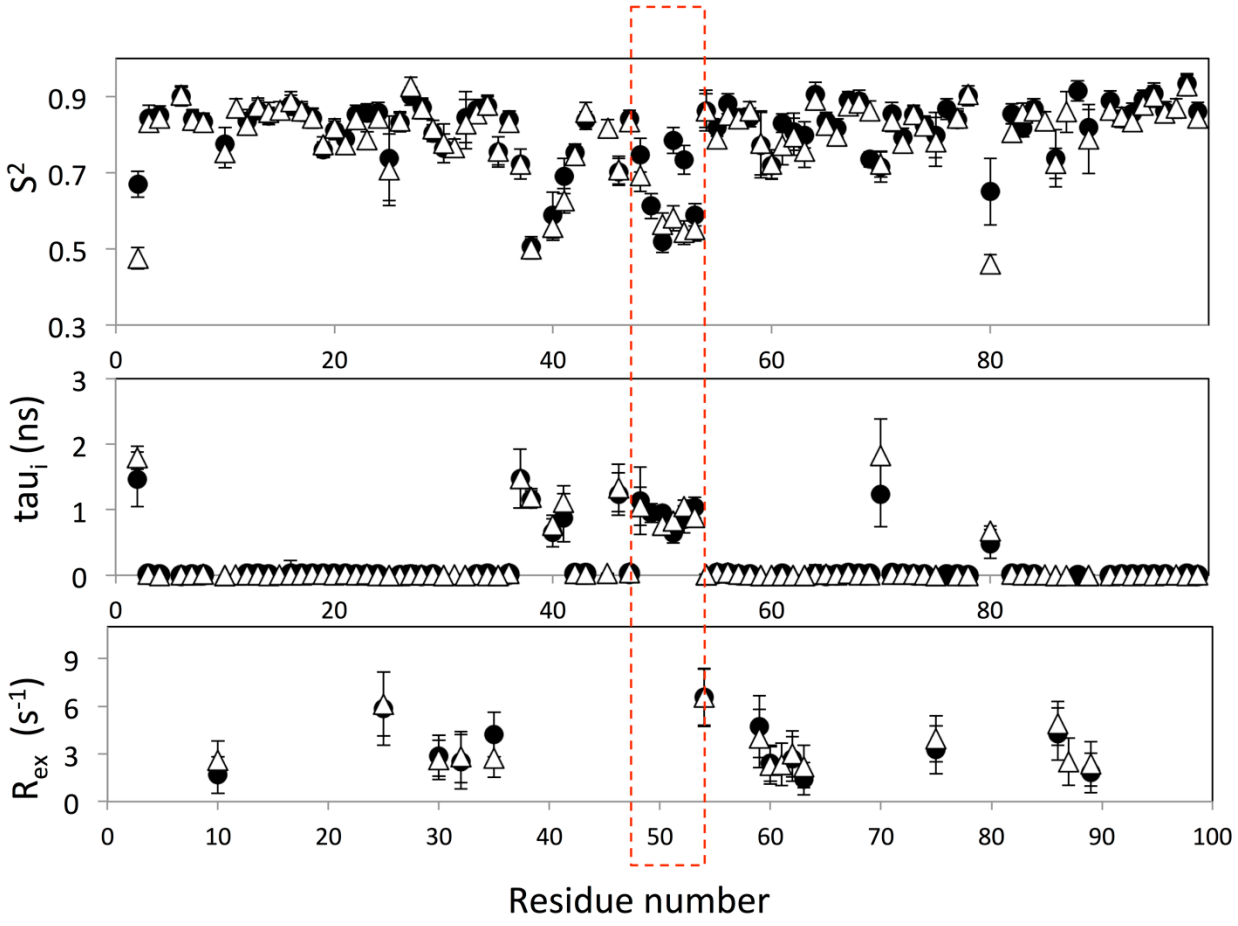

Figure 6.3 Dynamic parameters obtained from model free analysis of NMR relaxation data for WT (filled circles) and Flap+ HIV-1 Protease (open triangles).

Overall, decrease in calculated order parameters, and measured R_2 and $\{^1H\}$-^{15}N NOE values (**Figure 6.4**) converge in indicating that the mutations in the Flap+ protease increases the fast (sub-nanosecond) dynamics of the flap region, by possibly decreasing the slower motions on the micro- to millisecond time scales. Such alteration of flap dynamics may be important for modulating the on/off rates for substrate and inhibitor binding.

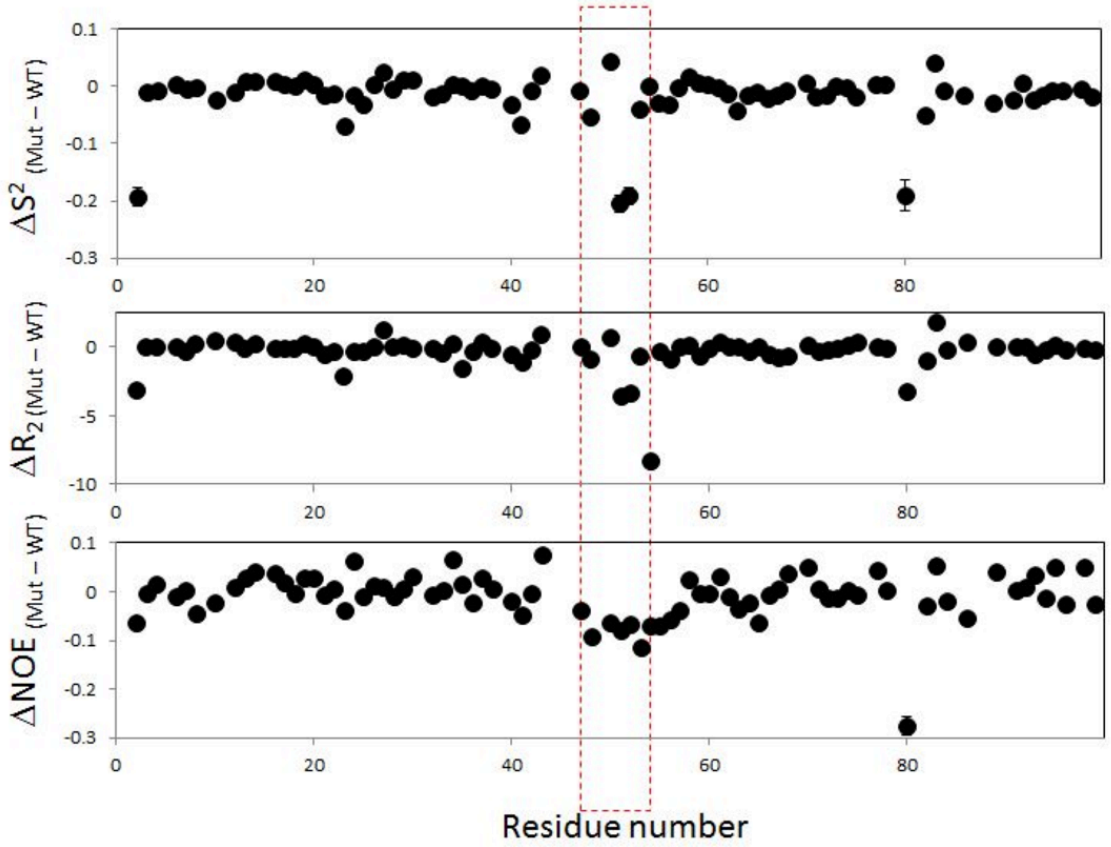

Figure 6.4 Change in dynamic parameters in Flap+ with respect to the WT HIV-1 protease calculated from the data in **Figures 6.2** and **6.3**.

6.3.2 Comparison NMR results to MD results from collaboration

As mentioned in section 6.2, Molecular Dynamics simulations of the apo form WT and Flap+ proteases were performed by our collaborators Yufeng Cai, Nese Yilmaz, and Celia Schiffer. Additional results from the MD simulations are described in Section 6.5. To compare the characteristics of HIV-1 protease local backbone dynamics inferred from MD simulations and NMR experiments, we calculated the generalized order parameters S^2 of the backbone amides from MD trajectories and compared them

with those obtained by NMR model free analysis (**Figure 6.5**). The calculated S^2 values agree well with the NMR results, capturing the regions with restricted and increased internal motions. The flap regions in both WT and Flap+ protease display the lowest S^2 values, indicating they are very mobile on the sub-nanosecond time scale. Calculating the order parameters using only the first 20 ns of the 100 ns trajectories resulted in much higher values for the flap regions (results not shown), indicating slower flap motions with nanosecond time scale correlation times. These slower local motions likely complicate the model free analysis of NMR relaxation data for the flaps, as they happen on a time scale that cannot be assumed independent from the global motion of the protease (rotational correlation time ~12 ns). Nevertheless, comparison of MD and NMR results suggest that MD simulations have captured the overall dynamics of local motions probed in NMR experiments, on the real time scale.

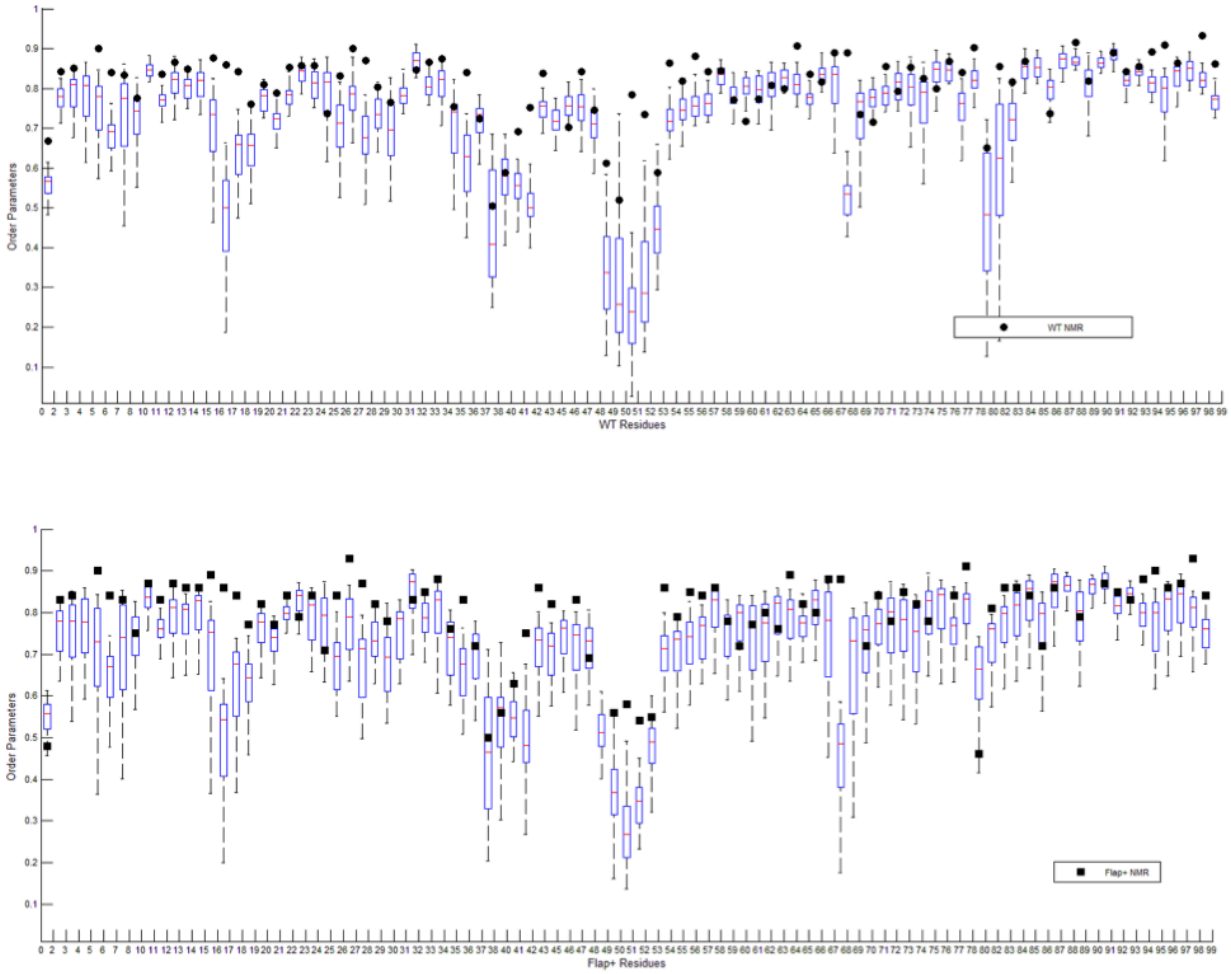

Figure 6.5 Order parameters of backbone N-H bonds calculated from the 20 independent 100 ns MD simulation are shown in boxplot. Order parameters from NMR experiments are displayed as (A) black circles for WT protease, (B) squares for drug-resistant variant FLAP+.

Indeed, results from MD simulations help explain NMR relaxation data obtained. The increase in the inter-monomer distance in Flap+ compared to WT protease in MD simulations (Section 6.6, **Figure 6.9**) is consistent with the observed changes in NMR relaxation parameters (**Figure 6.4**). As previously reported, the flaps undergo slow conformational exchange in solution where the WT protease populates a minor conformation with the two flaps interacting with each other (84). In the Flap+ variant, MD

simulations reveal that the inter-subunit distance increases (Section 6.6, **Figure 6.9**), which will diminish the population of this minor conformation. The loss of this minor conformation will attenuate R_{ex}, the chemical/conformational exchange (in the milli-micro second time scale) contribution to R_2 of the Flap+. In addition, the loss of flap-flap interactions is expected to increase sub-nanosecond motions of the flap region, which should be reflected as a decrease in $\{^1H\}$-^{15}N NOE of Flap+ compared to WT protease. Consistent with this scenario, R_2 and $\{^1H\}$-^{15}N NOE of residues 51 and 52 in the Flap+ are significantly lower than those of the WT in the acquired NMR data (**Figure 6.4**), demonstrating that the MD simulation results nicely dissect the NMR experimental data.

6.4 DISCUSSION

Mutations that are known to confer drug resistance occur throughout HIV-1 protease in a complex and interdependent manner. These mutations not only involve residues that directly contact the protease inhibitors, but occur elsewhere in the enzyme making their role in conferring resistance more difficult to assess. One possible mechanism by which resistance may occur is through the alteration of the dynamics of the enzyme. The flexibility of the protease flaps are critical to the enzyme's activity as the flaps control access of the substrates and inhibitors to the protease active site. Thus resistance could potentially occur by modulating access to the active site.

The dynamics of a multi-drug resistant variant, Flap+ of HIV-1 protease was compared with the WT enzyme by a combination of MD simulations and NMR relaxation experiments. The Flap+ variant binds the protease inhibitors with large entropy-

enthalpy compensations compared to WT variant (101). The molecular mechanisms that cause these thermodynamic changes, and how protease dynamics might contribute to these energetic changes can only begin to be understood by understanding the relative dynamics of the apo forms of Flap+ relative to WT protease. The two methods for understanding dynamics are complementary in that NMR experiments provide an assessment of the overall dynamics and the MD simulations elucidate the details of protease dynamics in atomic details. Analysis of MD and NMR data concur in revealing that the overall dynamic properties of the enzyme are conserved, while the flap dynamics are altered in the Flap+ variant. In Flap+ protease, the flaps sample a more open conformational ensemble compared to the WT enzyme, with the flap tips curling towards the active site walls (80s loops), while these walls are coming closer together. The NMR results indicate that in the Flap+ variant, sub-nanosecond dynamics of the flaps are enhanced with respect to the WT protease, and the trends in the order parameters are reflected in the order parameters calculated in the MD trajectories. These complex alterations in the enzyme dynamics in Flap+ relative to the WT enzyme, particularly within the flaps, may contribute to the thermodynamic differences in the two enzymes and likely modulate the balance between substrate turn-over and drug binding, thereby conferring drug resistance.

6.5 CONCLUSIONS

The apo forms of the Flap+ HIV-1 Protease shows significant differences in the dynamics of flap region residues from the WT based on the NMR data. In addition, the

MD simulations indicate that the flap tips show significant difference in distance between the flaps from one subunit to another. Both data suggests that the flap region of the Flap+ protein shows fewer inter-flap contacts and suggest that the Flap+ protein may assume more of an open conformation with large distances. Although information on the ligand bound forms of the WT and Flap+ proteases are necessary for a more conclusive interpretation of the apo form data, it is likely that differences in the flap dynamics and conformations may be responsible for the differences in the thermodynamics of binding.

6.6 COLLABORATIVE WORK: MOLECULAR DYNAMICS SIMULATIONS

The methods and the parameters for the Molecular Dynamics simulations by our collaborators are described in detail in the original manuscript (22). In brief, a total of 20 fully hydrated 100 ns-MD trajectories each for WT and Flap+ apo form proteases were performed. In each simulation, energies converged and enabled extensive sampling of the conformational space. Snap shots of 20 MD simulations at each end point, i.e.,100 ns for the apo form WT and Flap+ HIV-1 PR show that flap regions are highly flexible, and adopt a variety of conformations (**Figure 6.6**). In this section, the analysis of the simulation data, in addition to the generalized order parameters described above (section XC), necessary for discussion will be described.

Variation of conformations observed in the snap shots (**Figure 6.6**) is more quantitatively evaluated by extracting the root-mean-squared (RMSF) fluctuations of the backbone Cα atoms, calculation of order parameters for backbone ^{15}N atoms, and

distribution of inter-atomic distances between atom pairs from the MD trajectories. The RMSF for the WT and Flap+ HIV-1 proteases (**Figure 6.7**) reflects the fluctuations of the protein backbone, similar to the NMR order parameters and the order parameters from MD simulations shown in **Figure 6.5**. The flap region of the protein shows increased fluctuations compared to the rest of the protein. Due to the large fluctuations of the Cα atoms, it is not clear that there is a significant difference between the WT and the Flap+ mutant proteases. However, the WT protein shows overall lower RMSF values and indicate that the Flap+ protein has more flexible backbone.

To identify correlation of motion in specific sites of the protease, distances between atom pairs were analyzed for the WT and Flap+ proteases from the MD simulation trajectories. The percent of time distribution of the atom pairs in the WT and Flap+ from the MD trajectories are shown in **Figures 6.8** and **6.9** and summarized in **Table 6.2**. In particular, the distance between the nitrogen atoms of the two side chain amino groups for K55 residues from the two subunits were investigated for comparison to studies in the literature that used EPR spectroscopy. The results show agreement with respect to the distribution of the atom pair distances and indicate that the Flap+ shows larger distance between the flap tips. This is in agreement with the model of the apo WT protease assuming a more rigid conformation with flap interactions while the apo Flap+ protease assumes a more flexible conformation with less flap interaction.

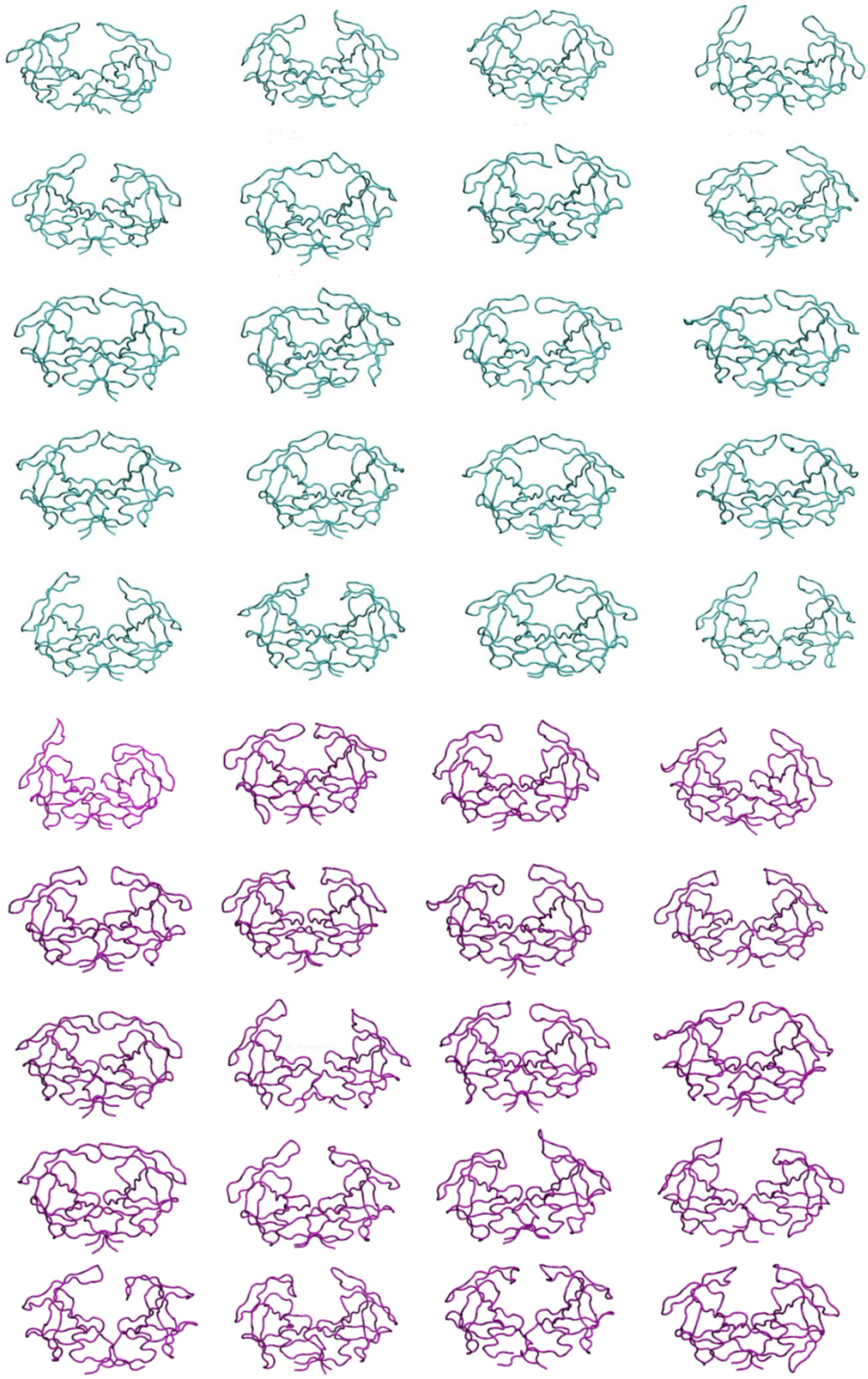

Figure 6.6 The 20 snapshots of WT (cyan) and Flap+ (magenta) HIV-1 protease conformation at the end of each 100 ns MD simulations.

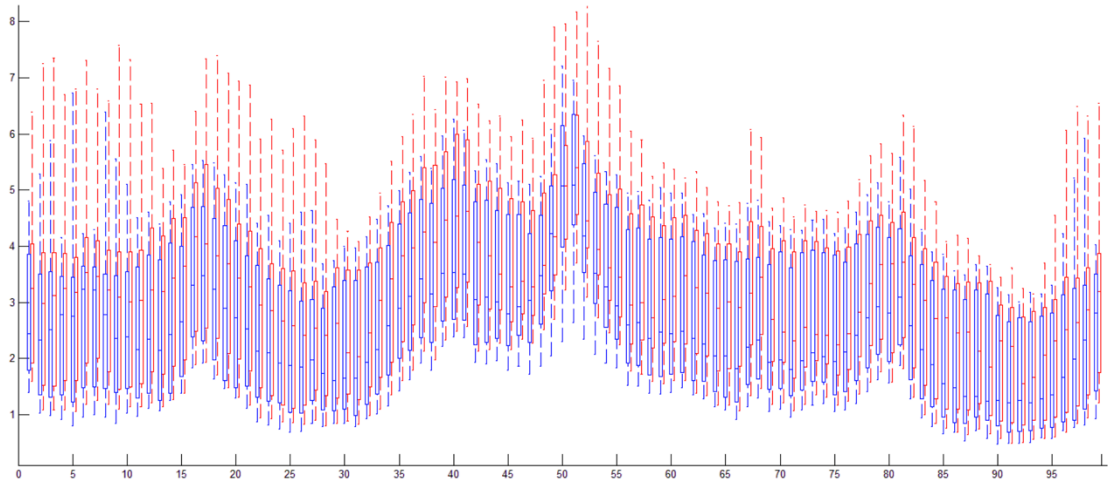

Figure 6.7 RMSF values of the Cα atoms for each residue in the 40 100nsec MD simulations displayed as boxplots for WT (blue) and Flap+ (red) HIV-1 protease.

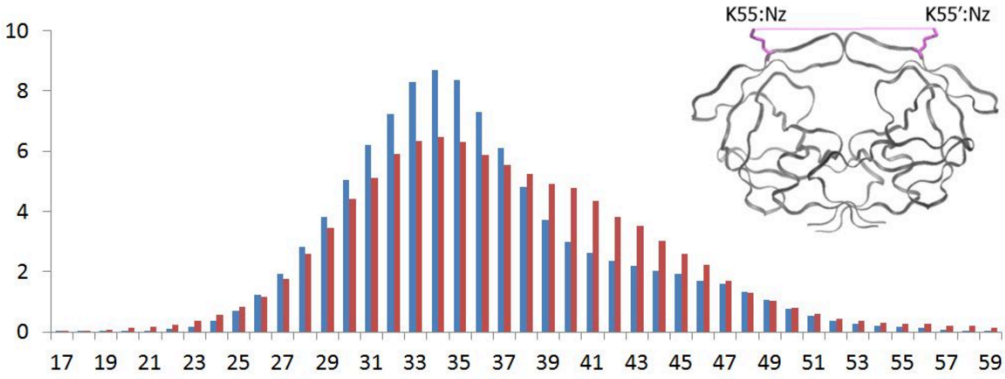

Figure 6.8 Distribution in percent of distances in Å between the nitrogen atoms in the amino group of the K55 and K55' side chain calculated over all 80 monomers during the 100 ns trajectories. Distribution data from the wild-type protease simulation are in blue, and from the Flap+ variant are in red.

Table 6.2 The mean and standard deviation for the distance distributions in Å between atom pairs (displayed in Figures 6.8 and 6.9) averaged over 80 monomers during 100 ns MD trajectories.

Atom pairs	Crystal (Å)	WT mean(Å)	WT sigma*	FLAP+ mean(Å)	FLAP+ sigma*	ΔMean**
nz55-	33.1	35.8	5.9	36.9	6.8	-1.1

nz55'						
50-50'	4.3	9.7	7.0	13.1	8.3	-3.4
50-80'	13.5	18.0	5.2	19.2	6.0	-1.1
50-25'	17.7	18.9	5.3	19.5	6.4	-0.6
50-25	17.2	16.8	3.2	16.2	3.3	0.6
80-80'	21.7	26.6	3.2	24.7	3.7	2.0
50-80	10.6	11.6	3.6	8.8	2.9	2.8

*** Sigma refers to standard deviation**

****ΔMean = (WT mean) – (Flap+ mean)**

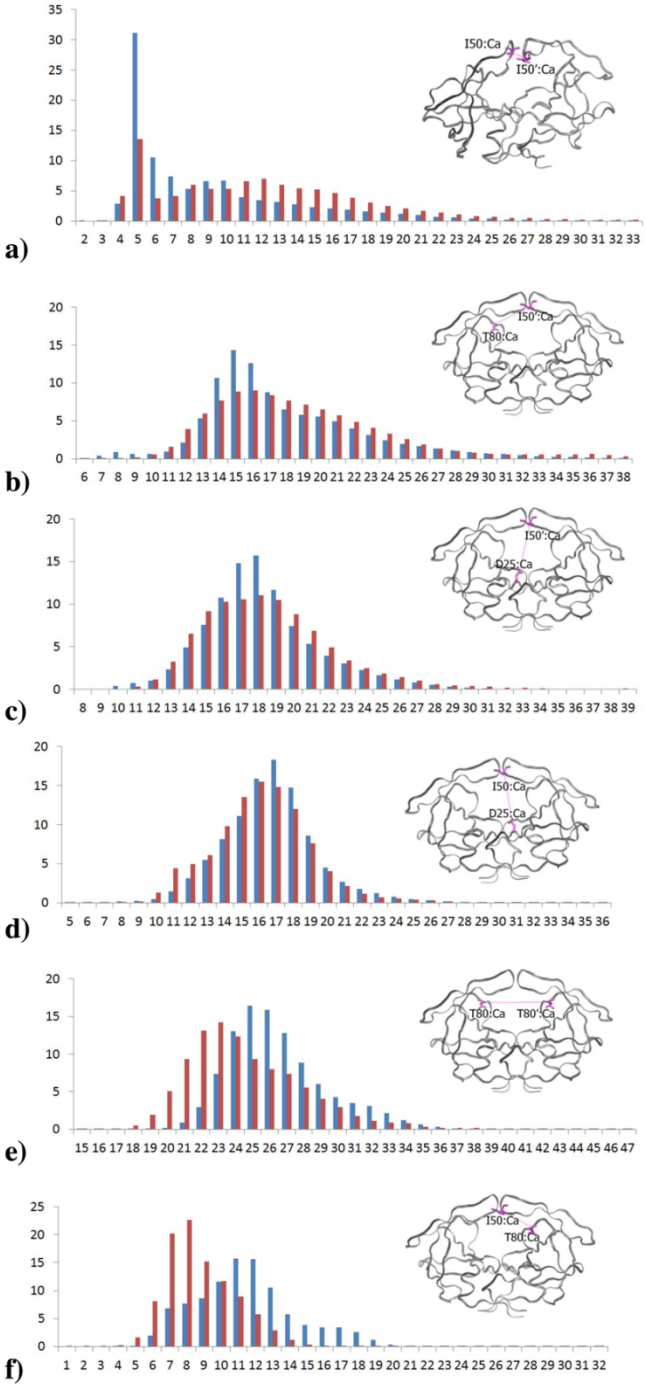

Figure 6.9 Distribution in percent of distances in Å between alpha carbons of the flaps, 80s loop and the active site in WT (blue) and Flap+ (red) HIV-1 protease calculated over all 80 monomers during the 100 ns trajectories. a) 50 – 50', b) 80 – 50', c) 25 – 50', d) 25 – 50, e) 80 – 80' f) 50-80

7.0 SUMMARY AND FUTURE WORK

7.1 ANALYSIS AND IMPROVEMENT OF METHODOLOGY OF NMR RELAXATION EXPERIMENTS

The detailed analysis of NMR relaxation experiments that were performed in this thesis has provided insight into their strengths and limitations. Advancements in the instrumentation of NMR spectrometers(186; 185; 126; 141) and the improved sensitivity have required reevaluation of the methodology to ensure that assumptions used in the analysis of relaxation data remain valid. Furthermore, the applicability of new experiments(209) was tested by simulation and experiment.

In Chapter 2, the effect of different pulse sequences on ^{1}H decoupling during the CPMG pulse sequence is tested by simulation and experiment(139). In the measurement of the ^{15}N R_2 in-phase relaxation rate, the relaxation contribution due to the ^{1}H-^{15}N anti- phase component is minimized by decoupling of the ^{15}N nuclei from the directly bonded ^{1}H using different 180º decoupling pulse schemes (for standard CPMG sequence with ^{1}H decoupling pulses or with more frequent ^{1}H pulses, Schemes I and III) or composite decoupling of ^{1}H(Scheme II). However, due to limitations in the NMR instrumentation, specifically the limited power capabilities of cryogenically cooled probes, high power decoupling pulses may not be utilized. The motivation for this study

is to evaluate the decoupling pulse sequences to determine whether significant R_2 error due to anti-phase ^1H-^{15}N relaxation may be present in the measurement of in-phase ^{15}N relaxation rates due to insufficient ^1H decoupling. The results indicate that Schemes II and III both show correlation of the measured (both experimentally determined and from simulation) with Scheme I, the standard CPMG sequence. However, Schemes II and III may be better for protein samples with low ionic concentration due to reduction of probe heating from frequent ^{15}N 180º pulses. In addition, Scheme III does not have the limitation on setting the τ_N to be synchronized with the ^1H composite pulse supercycle.

The effect of chemical exchange during refocusing pulses and their possible contribution to systematic errors in the CT-CPMG R_2 relaxation dispersion experiment was studied in Chapter 3(140). In the analysis of the CT-CPMG experiment(25; 94), the 180º refocusing ^{15}N pulses are assumed to be instantaneous rotations and the effect of finite pulse widths are not considered. Since chemical exchange during the pulses occur under different effective field (similar to the condition of chemical exchange during $R_1\rho$ experiment) compared to exchange that occurs during the inter-pulse delays, the possible contribution to systematic errors due to the assumptions in the analysis of the data were analyzed. To evaluate the effect of pulse duration in the CT-CPMG R_2 relaxation dispersion experiment, the results of various chemical exchange conditions were calculated using the Bloch-McConnell equations(130) and were analyzed by solutions to the Bloch-McConnell equations(25; 94). The results indicated that under some chemical exchange conditions at high values of ν_{eff}, the R_2 parameters calculated using instantaneous pulses deviate from R_2 parameters determined using finite pulses (with 90 μs for 180º rotation). When the chemical exchange parameters are optimized

to the calculated R_2 values, the discrepancy between the instantaneous pulses and 90 μs finite pulses may lead to error in the major population, p_a, of up to 3.5% (as a percent of the input p_a) and timescale of exchange, k_{ex}, of 12.5%.

With the availability of higher field NMR spectrometers operating at ^{1}H Larmor frequencies of 900 MHz and higher(126; 141), the issue of resonance offset has become more significant. Although the spectrum width is over 1.5 times the width of a 600 MHz spectrometer, the ^{15}N pulse width often remains similar (at ~90 μs for 180° pulses) due to power limitations of cryogenically cooled probes. In addition, the power limitations of some cryogenically cooled probes were lower at ~200 μs for 180º ^{15}N pulses(209). To address the increased resonance offset effect, a phase alternating pulse sequence was developed by the Zuiderweg group(209). In contrast to the conventional CPMG sequence (referred to as the [00000000] sequence in the chapter), the phase alternating sequence, called the [00130031] sequence, incorporates alternative phase (such as Y and -Y) pulses in addition to the conventional CPMG sequence (such as X) pulses(209). The results from simulations indicate that both the [00000000] and [00130031] sequences show similar results under most conditions When the ^{15}N pulse is miscalibrated with B_1 being 20% weaker, the [00130031] sequence shows lower resonance offset errors in the absence of chemical exchange but indicate systematic contamination of R_2 relaxation by R_1.

In Chapter 4, the viability of the minimum component of the alternating phase scheme [00-13] was tested using simulation and experiment and compared to the equivalent conventional CPMG pulse sequence, [00-00] (137). The results from the comparison of the [00-13] and the [00-00] pulse sequences indicate that when using

higher power pulses both sequences show similar R_2 values for a wide spectral range but the [00-13] sequence shows lower R_2 errors compared to the [00-00] sequence at large resonance offset. The comparison of the errors in the in-phase R_2 for the [00-00] and the [00-13] sequences was performed using two methods: 1) taking the noise errors or 2) taking the deviation of the intensity from the initial fit to single exponential decay. In method 1, only the signal-to-noise ratio of the experiment is considered while in method 2, more errors such as error due to resonance offsets were considered. However, for experimental data of a moderately sized protein (HIV-1 protease) at lower field strength (600 MHz), no significant difference was observed between the two methods (although method 2 shows a small increase in the R_2 error compared to method 1).

In addition to the work presented in this thesis, the methods used in the analysis of the {^{1}H}-^{15}N NOE experiment will need to be evaluated in detail. Error for the {^{1}H}-^{15}N NOE parameter is typically calculated from the experimental noise(40). However, with increases in sensitivity from improved instrumentation, it is possible that the {^{1}H}-^{15}N NOE errors can be underestimated. Therefore, it is important to reevaluate the methods used in the estimation of peak intensities as well as estimation of errors in the {^{1}H}-^{15}N NOE experiment to ensure that the current methods are valid for high sensitivity data.

7.2 PROTEIN DYNAMICS FROM NMR RELAXATION EXPERIMENTS

In this thesis, the protein backbone dynamics and conformations for SERCA-N (138) and HIV-1 protease (22) were studied using NMR relaxation experiments as well as other methods. The information gathered from the biophysical methods provided insight into the function of the proteins and the effects of mutations on protein structure, dynamics, and stability. In Chapter 5(138), the mutations in SERCA-N protein were investigated by NMR, CD, and Fluorescence spectroscopies to characterize ATP binding for WT, active site mutants (T441A, R560V, and C561A) (29), and a mutant found in patients with Darier's Disease (E412G) (167; 129). Although the Circular Dichroism spectra shows almost identical secondary structure content, the ^{1}H and ^{15}N chemical shifts from NMR spectra showed that the E412G mutant shows small differences from WT throughout the entire protein while the active site mutants showed only chemical shift perturbations near the site of mutation. Considering the decreased stability of the E412G mutant and the similar K_D of the mutant to WT, it is likely that the E412G mutant SERCA is active and stable in cardiac cells allowing for function but other cellular factors may lead to instability and SERCA dysfunction in skin cells to lead to Darier's disease.

In Chapter 6, the dynamics of the HIV-1 protease WT and a multi-drug resistant mutant Flap+ were characterized by NMR relaxation experiments and the results were compared to results obtained by MD simulations (in collaboration with Yufeng Cai, Nese Yilmaz, and Celia Schiffer at the University of Massachusetts Medical School) (137). The Flap+ mutant was shown to have significant differences from the WT in the thermodynamics of ligand binding (more favorable entropy of binding and unfavorable

enthalpy of binding to Darunavir was observed for the Flap+ protease compared to the WT) and the dynamics of the Flap+ mutant were investigated to determine how mutations change the mechanism of the protein and possibly lead to drug resistance. The NMR results indicate that significant differences in the functionally important flap region are present, with the Flap+ mutant showing increased backbone flexibility in the sub-nano second timescale compared to WT. In addition, MD results showed agreement with the NMR relaxation results and showed increase in the flexibility of Flap+ compared to WT and also showed significant differences in the inter-flap distances between the WT and Flap+ proteases. The Flap+ protease showed a larger distance between the tips of the flaps compared to the WT. The decrease in the interaction of the flap tips may be a consequence of the increase in flap dynamics as seen by NMR.

7.3 CHARACTERIZATION OF APO AND DARUNAVIR BOUND WT AND FLAP+ HIV-1 PROTEASE

Currently, the Darunavir (DRV) (57; 58) bound form dynamics and conformations for the WT and Flap+ proteases are being characterized. Possible differences in the dynamics or the DRV bound conformations of the WT and Flap+ proteases may help explain the differences in the mechanism of inhibitor binding. In addition, slower timescale motions, ranging from the millisecond to microsecond, were investigated for the apo form and DRV bound form WT and Flap+ proteases by Constant Time Carr-Purcell-Meiboom-Gill R_2 relaxation dispersion experiments. In conjunction with the sub-

nanosecond dynamics information, the information on the free form conformations may help relate the thermodynamics of binding to the conformational and dynamical aspects of HIV-1 protease.

BIBLIOGRAPHY

1. Abragam A. 1961. Principles of Nuclear Magnetism, Oxford University Press, Oxford.
2. Abu-Abed M, Mal TK, Kainosho M, MacLennan DH, Ikura M (2002) Characterization of the ATP-Binding Domain of the Sarco(endo)plasmic Reticulum Ca2+-ATPase: Probing Nucleotide Binding by Multidimensional NMR. Biochemistry 41:1156-1164.
3. Abu-Abed M, Millet O, MacLennan DH, Ikura M (2004) Probing nucleotide-binding effects on backbone dynamics and folding of the nucleotide-binding domain of the sarcoplasmic/endoplasmic-reticulum Ca2+-ATPase. Biochem J 379:235-242.
4. Akke M, Palmer AGr (1996) Monitoring Macromolecular Motions on Microsecond to Millisecond Time Scales by R1ρR1 Constant Relaxation Time NMR Spectroscopy. J Am Chem Soc 118:911-912.
5. Ali A, Bandaranayake RM, Cai Y, King NM, Kolli M, Mittal S, Murzycki JF, Nalam MN, Nalivaika EA, Ozen A, Prabu-Jeyabalan MM, Thayer K, Schiffer CA (2010) Molecular Basis for Drug Resistance in HIV-1 Protease. Viruses 2:2509-2535.
6. Allard P, Helgstrand M, Hard T (1997) A Method for Simulation of NOESY, ROESY, and Off-Resonance ROESY Spectra. J Magn Reson 129:19-29.
7. Allard P, Helgstrand M, Hard T (1998) The complete homogeneous master equation for a heteronuclear two-spin system in the basis of Cartesian product operators. J Magn Reson 134:7-16.
8. Axelsen KB, Palmgren MG (1998) Evolution of substrate specificities in the P-type ATPase superfamily. J Mol Evol 46:84-101.
9. Bain AD, Anand CK, Nie Z (2010) Exact solution to the Bloch equations and application to the Hahn echo. J Magn Reson 206:227-240.
10. Bain AD, Anand CK, Nie Z (2011) Exact solution of the CPMG pulse sequence with phase variation down the echo train: application to R2 measurements. J Magn Reson 209:183-194.
11. Bandaranayake RM, Kolli M, King NM, Nalivaika EA, Heroux A, Kakizawa J, Sugiura W, Schiffer CA (2010) The effect of clade-specific sequence polymorphisms on HIV-1 protease activity and inhibitor resistance pathways. J Virol 84:9995-10003.
12. Barchi JJ, Jr., Grasberger B, Gronenborn AM, Clore GM (1994) Investigation of the backbone dynamics of the IgG-binding domain of streptococcal protein G by heteronuclear two-dimensional 1H-15N nuclear magnetic resonance spectroscopy. Protein Sci 3:15-21.
13. Bax A, Clore GM, Gronenborn AM (1990) 1H□1H correlation via isotropic mixing of 13C magnetization, a new three-dimensional approach for assigning 1H and 13C spectra of 13C-enriched proteins. Journal of Magnetic Resonance (1969) 88:425-431.

14. Bax A, Ikura M (1991) An efficient 3D NMR technique for correlating the proton and15N backbone amide resonances with the α-carbon of the preceding residue in uniformly15N/13C enriched proteins. Journal of Biomolecular NMR 1:99-104.
15. Beach H, Cole R, Gill ML, Loria JP (2005) Conservation of mu s-ms enzyme motions in the apo- and substrate-mimicked state. Journal of the American Chemical Society 127:9167-9176.
16. Bevington PR, Robinson DK. 1992. Data Reduction and Error Analysis for the Physical Sciences, McGraw-Hill Neew York.
17. Boucher W, Laue ED, Campbell-Burk S, Domaille PJ (1992) Four-dimensional heteronuclear triple resonance NMR methods for the assignment of backbone nuclei in proteins. Journal of the American Chemical Society 114:2262-2264.
18. Brath U, Akke M, Yang D, Kay LE, Mulder FA (2006) Functional dynamics of human FKBP12 revealed by methyl 13C rotating frame relaxation dispersion NMR spectroscopy. J Am Chem Soc 128:5718-5727.
19. Bretthorst GL, Hutton WC, Garbow JR, Ackerman JJH (2005) Exponential parameter estimation (in NMR) using Bayesian probability theory. Concepts Magn Reson 27A:55-63.
20. Brini M, Carafoli E (2009) Calcium pumps in health and disease. Physiol Rev 89:1341-1378.
21. Bruschweiler R (2003) New approaches to the dynamic interpretation and prediction of NMR relaxation data from proteins. Current Opinion in Structural Biology 13:175-183.
22. Cai Y, Kurt Yilmaz N, Myint W, Ishima R, Schiffer CA (2012) Differential Flap Dynamics in Wild-Type and a Drug Resistant Variant of HIV-1 Protease Revealed by Molecular Dynamics and NMR Relaxation. Journal of Chemical Theory and Computation 8:3452-3462.
23. Cai Y, Schiffer C (2012) Decomposing the energetic impact of drug-resistant mutations: the example of HIV-1 protease-DRV binding. Methods Mol Biol 819:551-560.
24. Cai Y, Schiffer CA (2010) Decomposing the energetic impact of drug resistant mutations in HIV-1 protease on binding DRV. J Chem Theory Comput 6:1358-1368.
25. Carver JP, Richards RE (1972) General 2-Site Solution for Chemical Exchange Produced Dependence of T2 Upon Carr-Purcell Pulse Separation. Journal of Magnetic Resonance 6:89-105.
26. Cavanagh J, Fairbrother WJ, Palmer AG, Skelton NJ. 1996. Protein NMR Spectroscopy, Academic Press, San Diego.
27. Champeil P, Menguy T, Soulie S, Juul B, de Gracia AG, Rusconi F, Falson P, Denoroy L, Henao F, le Maire M, Moller JV (1998) Characterization of a Protease-resistant Domain of the Cytosolic Portion of Sarcoplasmic Reticulum Ca2+-ATPase. Journal of Biological Chemistry 273:6619-6631.
28. Chandrasekhar I, Clore GM, Szabo A, Gronenborn AM, Brooks BR (1992) A 500 ps molecular dynamics simulation study of interleukin-1 beta in water. Correlation with nuclear magnetic resonance spectroscopy and crystallography. J Mol Biol 226:239-250.
29. Clausen JD, McIntosh DB, Vilsen B, Woolley DG, Andersen JP (2003) Importance of Conserved N-domain Residues Thr441, Glu442, Lys515, Arg560, and Leu562 of Sarcoplasmic Reticulum Ca2+-ATPase for MgATP Binding and Subsequent Catalytic Steps. Journal of Biological Chemistry 278:20245-20258.

30. Clore GM, Driscoll PC, Wingfield PT, Gronenborn AM (1990) Analysis of the backbone dynamics of interleukin-1 beta using two-dimensional inverse detected heteronuclear 15N-1H NMR spectroscopy. Biochemistry 29:7387-7401.
31. Czisch M, King GC, Ross A (1997) Removal of systematic errors associated with off-resonance oscillations in T2 measurements. J magn Reson 126:154-157.
32. Daura X, Gademann K, Schafer H, Jaun B, Seebach D, van Gunsteren WF (2001) The beta-peptide hairpin in solution: Conformational study of a beta-hexapeptide in methanol by NMR spectroscopy and MD simulation. J Am Chem Soc 123:2393-2404.
33. Davis DG, Perlman ME, London RE (1994) Direct Measurements of the Dissociation-Rate Constant for Inhibitor-Enzyme Complexes Via the T-1-Rho and T-2 (Cpmg) Methods. Journal of Magnetic Resonance Series B 104:266-275.
34. Dayie KT, Wagner G, Lefevre JF (1996) Theory and practice of nuclear spin relaxation in proteins. Annual Review of Physical Chemistry 47:243-282.
35. Delaglio F, Grzesiek S, Vuister GW, Zhu G, Pfeifer J, Bax A (1995) NMRPipe: A multidimensional spectral processing system based on UNIX pipes. Journal of Biomolecular NMR 6:277-293.
36. Dhitavat J, Dode L, Leslie N, Sakuntabhai A, Lorette G, Hovnanian A (2003) Mutations in the Sarcoplasmic/Endoplasmic Reticulum Ca2+ ATPase Isoform Cause Darier's Disease. J Investig Dermatol 121:486-489.
37. Eisenmesser E, Millet O, Labeikovsky W, Korzhnev D, Wolf-Watz M, Bosco DA, Skalicky JJ, Kay LE, Kern D (2005) Intrinsic dynamics of an enzyme underlies catalysis. Nature 438:117-121.
38. Eriksson MA, Berglund H, Härd T, Nilsson L (1993) A comparison of 15N NMR relaxation measurements with a molecular dynamics simulation: backbone dynamics of the glucocorticoid receptor DNA-binding domain. Proteins 17:375-390.
39. Ernst RR, Bodenhausen G, Wokaun A. 1987. Principles of Nuclear Magnetic Resonance in One and Two Dimensions, Clarendon Press, Oxford.
40. Farrow NA, Muhandiram R, Singer AU, Pascal SM, Kay CM, Gish G, Shoelson SE, Pawson T, Forman-Kay JD, Kay LE (1994) Backbone Dynamics of a Free and a Phosphopeptide-Complexed Src Homology 2 Domain Studied by 15N NMR Relaxation. Biochemistry 33:5984-6003.
41. Farrow NA, Zhang O, Forman-Kay JD, Kay LE (1995) Comparison of the backbone dynamics of a folded and an unfolded SH3 domain existing in equilibrium in aqueous buffer. Biochemistry 34:868-878.
42. Farrow NA, Zhang O, Forman-Kay JD, Kay LE (1997) Characterization of the backbone dynamics of folded and denatured states of an SH3 domain. Biochemistry 36:2390-2402.
43. Flexner C (2007) HIV drug development: the next 25 years. Nat Rev Drug Discov 6:959-966.
44. Floyd R, Wray S (2007) Calcium transporters and signalling in smooth muscles. Cell Calcium 42:467-476.
45. Foulkes JE, Prabu-Jeyabalan M, Cooper D, Henderson GJ, Harris J, Swanstrom R, Schiffer CA (2006) Role of invariant Thr80 in human immunodeficiency virus type 1 protease structure, function, and viral infectivity. J Virol 80:6906-6916.
46. Freedberg DI, Ishima R, Jacob J, Wang YX, Kustanovich I, Louis JM, Torchia DA (2002) Rapid structural fluctuations of the free HIV protease flaps in solution. Protein Sci 11:221-232.

47. Freedberg DI, Ishima R, Jacob J, Wang YX, Kustanovich I, Louis JM, Torchia DA (2002) Rapid structural fluctuations of the free HIV protease flaps in solution: Relationship to crystal structures and comparison with predictions of dynamics calculations. Protein Sci 11:221-232.
48. Freeman R, Hill HDW (1971) Fourier Transform Study of NMR Spin-Lattic Relaxation by "Progressive Saturation". Journal of Chemical Physics 54:3367-3377.
49. Fulton DB, Ni F (1997) ROESY with Water Flip Back for High-Field NMR of Biomolecules. J Biomol NMR 129:93-97.
50. Furfine ES, Dsouza E, Ingold KJ, Leban JJ, Spector T, Porter DJT (1992) 2-Step Binding Mechanism for Hiv Protease Inhibitors. Biochemistry 31:7886-7891.
51. Fushman D, Cowburn D. Nuclear magnetic resonance relaxation in determination of residue-specific N-15 chemical shift tensors in proteins in solution: Protein dynamics, structure, and applications of transverse relaxation optimized spectroscopy. (2001) Methods in Enzymology Nuclear Magnetic Resonance of Biological Macromolecules, Pt B. pp. 109-126.
52. Gadian DG, Robinson FNH (1979) Radiofrequency Losses in NMR Experiments on Electrically Conducting Samples. J Magn Reson 34:449-455.
53. Galiano L, Blackburn ME, Veloro AM, Bonora M, Fanucci GE (2009) Solute effects on spin labels at an aqueous-exposed site in the flap region of HIV-1 protease. J Phys Chem B 113:1673-1680.
54. Galiano L, Bonora M, Fanucci GE (2007) Interflap distances in HIV-1 protease determined by pulsed EPR measurements. J Am Chem Soc 129:11004-11005.
55. Galiano L, Ding F, Veloro AM, Blackburn ME, Simmerling C, Fanucci GE (2009) Drug pressure selected mutations in HIV-1 protease alter flap conformations. J Am Chem Soc 131:430-431.
56. Ghose R, Fushman D, Cowburn D (2001) Determination of the rotational diffusion tensor of macromolecules in solution from nmr relaxation data with a combination of exact and approximate methods--application to the determination of interdomain orientation in multidomain proteins. J Magn Reson 149:204-217.
57. Ghosh AK, Chapsal BD, Weber IT, Mitsuya H (2007) Design of HIV Protease Inhibitors Targeting Protein Backbone: An Effective Strategy for Combating Drug Resistance. Accounts of Chemical Research 41:78-86.
58. Ghosh AK, Dawson ZL, Mitsuya H (2007) Darunavir, a conceptually new HIV-1 protease inhibitor for the treatment of drug-resistant HIV. Bioorganic & Medicinal Chemistry 15:7576-7580.
59. Goldman M (1984) Interference Effects in the Relaxation of a Pair of Unlike Spin-1/2 Nuclei. Journal of Magnetic Resonance 60:437-452.
60. Grzesiek S, Bax A (1992) Correlating backbone amide and side chain resonances in larger proteins by multiple relayed triple resonance NMR. Journal of the American Chemical Society 114:6291-6293.
61. Grzesiek S, Bax A (1992) An efficient experiment for sequential backbone assignment of medium-sized isotopically enriched proteins. Journal of Magnetic Resonance (1969) 99:201-207.
62. Grzesiek S, Bax A (1992) Improved 3D triple-resonance NMR techniques applied to a 31 kDa protein. Journal of Magnetic Resonance (1969) 96:432-440.

63. Guerini D, Foletti D, Vellani F, Carafoli E (1996) Mutation of conserved residues in transmembrane domains 4,6 and 8 causes loss of Ca2+ transport by the plasma membrane Ca2+ pump. Biochemistry 35:3290-3296.
64. Guerini D, Zecca-Mazza A, Carafoli E (2000) Single amino acid mutations in transmembrane domain 5 confer to the plasma membrane Ca2+ pump properties typical of the Ca2+ pump of endo(sarco)plasmic reticulum. J Biol Chem 275:31361-31368.
65. Gullion T, Baker DB, Conradi MS (1990) New, Compensated Carr-Purcell Sequences. J Magn Reson 89:479-484.
66. Hansen DF, Yang D, Feng H, Zhou Z, Wiesner S, Bai Y, Kay LE (2007) An exchange-free measure of 15N transverse relaxation: an NMR spectroscopy application to the study of a folding intermediate with pervasive chemical exchange. J Am Chem Soc 129:11468-11478.
67. Hass MA, Vlasie MD, Ubbink M, Led JJ (2009) Conformational exchange in pseudoazurin: different kinds of microsecond to millisecond dynamics characterized by their pH and buffer dependence using 15N NMR relaxation. Biochemistry 48:50-58.
68. Heaslet H, Rosenfeld R, Giffin M, Lin YC, Tam K, Torbett BE, Elder JH, McRee DE, Stout CD (2007) Conformational flexibility in the flap domains of ligand-free HIV protease. Acta Crystallogr D Biol Crystallogr 63:866-875.
69. Heinrich J, Lyons L (2007) Systematic errors Ann Rev Nucl Part Sci 57:145-169.
70. Hoffman RE (2006) Standardization of chemical shifts of TMS and solvent signals in NMR solvents. Magn Reson Chem 44:606-616.
71. Horita DA, Zhang W, Smithgall TE, Gmeiner WH, Byrd RA (2000) Dynamics of the Hck-SH3 domain: comparison of experiment with multiple molecular dynamics simulations. Protein Sci 9:95-103.
72. Horiuchi T, Takahashi M, Kikuchi J, Yokoyama S, Maeda H (2005) Effect of dielectric properties of solvents on the quality factor for a beyond 900 MHz cryogenic probe model. J Magn Reson 174:34-42.
73. Hornak V, Okur A, Rizzo RC, Simmerling C (2006) HIV-1 protease flaps spontaneously close to the correct structure in simulations following manual placement of an inhibitor into the open state. J Am Chem Soc 128:2812-2813.
74. Hornak V, Okur A, Rizzo RC, Simmerling C (2006) HIV-1 protease flaps spontaneously open and reclose in molecular dynamics simulations. Proc Natl Acad Sci USA 103:915-920.
75. Hornak V, Simmerling C (2007) Targeting structural flexibility in HIV-1 protease inhibitor binding. Drug Discovery Today 12:132-138.
76. Hoult DI, Lauterbur PC (1979) The Sensitivity of the Zeugmatographic Experiment Involving Human Samples. J Magn Reson 34:425-433.
77. Huang GS, Oas TG (1995) Submillisecond folding of monomeric lambda repressor. Proc Natl Acad Sci U S A 92:6878-6882.
78. Hurlimann MD (2001) Carr-Purcell sequences with composite pulses. J Magn Reson 152:109-123.
79. Igumenova TI, Frederick KK, Wand AJ (2006) Characterization of the fast dynamics of protein amino acid side chains using NMR relaxation in solution. Chemical Reviews 106:1672-1699.
80. Ikura M, Kay LE, Bax A (1990) A novel approach for sequential assignment of proton, carbon-13, and nitrogen-15 spectra of larger proteins: heteronuclear triple-resonance

three-dimensional NMR spectroscopy. Application to calmodulin. Biochemistry 29:4659-4667.
81. Inesi G, Prasad AM, Pilankatta R (2008) The Ca2+ ATPase of cardiac sarcoplasmic reticulum: Physiological role and relevance to diseases. Biochemical and Biophysical Research Communications 369:182-187.
82. Ishima R (2011) Recent Developments in (15)N NMR Relaxation Studies that Probe Protein Backbone Dynamics. Top Curr Chem Sep 7:Epub ahead of print.
83. Ishima R, Freedberg DI, Wang YX, Louis JM, Torchia DA (1999) Flap opening and dimer-interface flexibility in the free and inhibitor-bound HIV protease, and their implications for function. Structure 7:1047-1055.
84. Ishima R, Louis JM (2008) A diverse view of protein dynamics from NMR studies of HIV-1 protease flaps. Proteins 70:1408-1415.
85. Ishima R, Torchia D (2006) Accuracy of Optimized Chemical-exchange Parameters Derived by Fitting CPMG R 2 Dispersion Profiles when R 2 0a≠ R 2 0b. Journal of Biomolecular NMR 34:209-219.
86. Ishima R, Torchia DA (2000) Protein dynamics from NMR. Nat Struct Biol 7:740-743.
87. Ishima R, Torchia DA (2003) Extending the range of amide proton relaxation dispersion experiments in proteins using a constant-time relaxation-compensated CPMG approach. J Biomol NMR 25:243-248.
88. Ishima R, Torchia DA (2005) Error estimation and global fitting in transverse-relaxation dispersion. J Biomol NMR 32:41-54.
89. Ishima R, Torciha DA, Louis JM (2007) Mutational and structural studies aimed at characterizing the monomer of HIV-1 protease and its precursor. J Biol Chem 282:17190-17199.
90. Ishima R, Wingfield PT, Stahl SJ, Kaufman JD, Torchia DA (1998) Using amide H-1 and N-15 transverse relaxation to detect millisecond time-scale motions in perdeuterated proteins: Application to HIV-1 protease. Journal of the American Chemical Society 120:10534-10542.
91. Istratov AA, Vyvenko OF (1999) Exponential analysis in physical phenomena. Rev Sci Instrum 70:1233–1257.
92. Jacobsen NJ, Lyons I, Hoogendoorn B, Burge S, Kwok PY, O'Donovan MC, Craddock N, Owen MJ (1999) ATP2A2 mutations in Darier's disease and their relationship to neuropsychiatric phenotypes. Hum Mol Genet 8:1631-1636.
93. Jarymowycz VA, Stone MJ (2006) Fast time scale dynamics of protein backbones: NMR relaxation methods, applications, and functional consequences. Chemical Reviews 106:1624-1671.
94. Jen J (1974) Chemical exchange and NMR-T2 relaxation. Advances in Molecular Relaxation Processes 6:171-183.
95. Johnson BA, Blevins RA (1994) NMR View: A computer program for the visualization and analysis of NMR data. Journal of Biomolecular NMR 4:603-614.
96. Kay LE (2005) NMR studies of protein structure and dynamics. J Magn Reson 173:193-207.
97. Kay LE, Ikura M, Tschudin R, Bax A (1990) Three-dimensional triple-resonance NMR spectroscopy of isotopically enriched proteins. Journal of Magnetic Resonance (1969) 89:496-514.
98. Kay LE, Nicholson LK, Delaglio F, Bax A, Torchia DA (1992) Pulse Sequences for Removal of the Effects of Cross Correlation between Dipolar and Chemical-Shift

Anisotropy Relaxation Mechanisms on the Measurement of Heteronuclear T1 and T2 Values in Proteins. Journal of Magnetic Resonance 97:359-375.
99. Kay LE, Torchia DA, Bax A (1989) Backbone dynamics of proteins as studied by nitrogen-15 inverse detected heteronuclear NMR spectroscopy: application to staphylococcal nuclease. Biochemistry 28:8972-8979.
100. Kelly AE, Ou HD, Withers R, Dotsch V (2002) Low-conductivity buffers for high-sensitivity NMR measurements. J Am Chem Soc 124:12013-12019.
101. King NM, Prabu-Jeyabalan M, Bandaranayake RM, Nalam MN, Ozen A, Haliloglu T, Schiffer C (2012) Extreme Entropy-Enthalpy Compensation in a Drug Resistant Variant of HIV-1 Protease. in preparation.
102. King NM, Prabu-Jeyabalan M, Nalivaika EA, Schiffer CA (2004) Combating susceptibility to drug resistance: Lessons from HIV-1 protease. Chem Biol 11:1333-1338.
103. King NM, Prabu-Jeyabalan M, Nalivaika EA, Wigerinck P, de Bethune MP, Schiffer CA (2004) Structural and thermodynamic basis for the binding of TMC114, a next-generation human immunodeficiency virus type 1 protease inhibitor. J Virol 78:12012-12021.
104. Korzhnev DM, Kloiber K, Kay LE (2004) Multiple-quantum relaxation dispersion NMR spectroscopy probing. J Am Chem Soc 126:7320-7329.
105. Korzhnev DM, Neudecker P, Zarrine-Afsar A, Davidson AR, Kay LE (2006) Abp1p and Fyn SH3 domains fold through similar low-populated intermediate states. Biochemistry 45:10175-10183.
106. Korzhnev DM, Religa TL, Banachewicz W, Fersht AR, Kay LE (2010) A Transient and Low-Populated Protein-Folding Intermediate at Atomic Resolution. Science 329:1312-1316.
107. Korzhnev DM, Tischenko EV, Arseniev AS (2000) Off-resonance effects in N-15 T-2 CPMG measurements. J Biomol NMR 17:231-237.
108. Kovrigin EL, Kempf JG, Grey MJ, Loria JP (2006) Faithful estimation of dynamics parameters from CPMG relaxation dispersion measurements. J Magn Reson 180:83-104.
109. Kumar A, Welti D, Ernst RR (1975) NMR Fourier zeugmatography. Journal of Magnetic Resonance (1969) 18:69-83.
110. Kupce E, Freeman R (1995) Adiabatic Pulses for Wideband Inversion and Broadband Decoupling. J Magn Reson A 115:273-276.
111. Kurt N, Scott WR, Schiffer CA, Haliloglu T (2003) Cooperative fluctuations of unliganded and substrate-bound HIV-1 protease: a structure-based analysis on a variety of conformations from crystallography and molecular dynamics simulations. Proteins 51:409-422.
112. Labeikovsky W, Eisenmesser EZ, Bosco DA, Kern D (2007) Structure and dynamics of pin1 during catalysis by NMR. J Mol Biol 367:1370-1381.
113. Lapatto R, Blundell T, Hemmings A, Overington J, Wilderspin A, Wood S, Merson JR, Whittle PJ, Danley DE, Geoghegan KF, et al. (1989) X-ray analysis of HIV-1 proteinase at 2.7 A resolution confirms structural homology among retroviral enzymes. Nature 342:299-302.
114. Laursen M, Bublitz M, Moncoq K, Olesen C, Moller JV, Young HS, Nissen P, Morth JP (2009) Cyclopiazonic acid is complexed to a divalent metal ion when bound to the sarcoplasmic reticulum Ca2+-ATPase. J Biol Chem 284:13513-13518.
115. Li Z, Raychaudhuri S, Wand AJ (1996) Insights into the local residual entropy of proteins provided by NMR relaxation. Protein Sci 5:2647-2650.

116. Lipari G, Szabo A (1982) Model-free approach to the interpretation of nuclear magnetic resonance relaxation in macromolecules. 1. Theory and range of validity. J Am Chem Soc 104:4546-4559.
117. Lipari G, Szabo A (1982) Model-free approach to the interpretation of nuclear magnetic resonance relaxation in macromolecules. 2. Analysis of experimental results. J Am Chem Soc 104:4559-4570.
118. Long D, Liu M, D. Y (2008) Accurately probing slow motions on millisecond timescales with a robust NMR relaxation experiment. J Am Chem Soc 130:2432-2433.
119. Loria JP, Berlow RB, Watt ED (2008) Characterization of enzyme motions by solution NMR relaxation dispersion. Acc Chem Res 41:212-221.
120. Loria JP, Rance M, Palmer AG (1999) A relaxation-compensated Carr-Purcell-Meiboom-Gill sequence for characterizing chemical exchange by NMR spectroscopy. Journal of the American Chemical Society 121:2331-2332.
121. Louis JM, Ishima R, Nesheiwat I, Pannell LK, Lynch SM, Torchia DA, Gronenborn AM (2003) Revisiting monomeric HIV-1 protease. Characterization and redesign for improved properties. J Biol Chem 278:6085-6092.
122. Luginbühl P, Wüthrich K (2002) Semi-classical nuclear spin relaxation theory revisited for use with biological macromolecules. Progress in nuclear magnetic resonance spectroscopy 40:199-247.
123. Luz Z, Meiboom S (1963) Nuclear Magnetic Resonance Study of the Protolysis of Trimethylammonium Ion in Aqueous Solution - Order fo the Reacion with Respect to Solvent. J Chem Phys 39:366-370.
124. Makinose M (1973) Possible functional states of the enzyme of the sarcoplasmic calcium pump. FEBS Lett 37:140-143.
125. Mandel AM, Akke M, Palmer AG (1995) Backbone Dynamics of Escherichia-Coli Ribonuclease Hi - Correlations with Structure and Function in an Active Enzyme. J Mol Biol 246:144-163.
126. Markiewicz WD, Dixon IR, Swenson CA, Marshall WS, Painter TA, Bole ST, Cosmus T, Parizh M, King M, Ciancetta G (2000) 900 MHz wide bore NMR spectrometer magnet at NHMFL. Applied Superconductivity, IEEE Transactions on 10:728-731.
127. Marley J, Lu M, Bracken C (2001) A method for efficient isotopic labeling of recombinant proteins. J Biomol NMR 20:71-75.
128. Masse JE, Keller R (2005) AutoLink: automated sequential resonance assignment of biopolymers from NMR data by relative-hypothesis-prioritization-based simulated logic. J Magn Reson 174:133-151.
129. Mayosi BM, Kardos A, Davies CH, Gumedze F, Hovnanian A, Burge S, Watkins H (2006) Heterozygous disruption of SERCA2a is not associated with impairment of cardiac performance in humans: implications for SERCA2a as a therapeutic target in heart failure. Heart 92:105-109.
130. McConnell HM (1958) Reaction Rates by Nuclear Magnetic Resonance. Journal of Chemical Physics 28:430-431.
131. Meiboom S, Gill D (1958) Modified Spin-Echo Method for Measuring Nuclear Relaxation Times. Rev Sci Instrm 29:688-691.
132. Misquitta CM, Mack DP, Grover AK (1999) Sarco/endoplasmic reticulum Ca2+(SERCA)-pumps: link to heart beats and calcium waves. Cell Calcium 25:277-290.

133. Miyauchi Y, Daiho T, Yamasaki K, Takahashi H, Ishida-Yamamoto A, Danko S, Suzuki H, Iizuka H (2006) Comprehensive Analysis of Expression and Function of 51 Sarco(endo)plasmic Reticulum Ca2+-ATPase Mutants Associated with Darier Disease. Journal of Biological Chemistry 281:22882-22895.
134. Mulder FA, Hon B, Mittermaier A, Dahlquist FW, Kay LE (2002) Slow internal dynamics in proteins: application of NMR relaxation dispersion spectroscopy to methyl groups in a cavity mutant of T4 lysozyme. J Am Chem Soc 124:1443-1451.
135. Mulder FA, van Tilborg PJ, Kaptein R, Boelens R (1999) Microsecond time scale dynamics in the RXR DNA-binding domain from a combination of spin-echo and off-resonance rotating frame relaxation measurements. J Biomol NMR 13:275-288.
136. Muthu P, Anuradha K (2007) SERCA pump isoforms: Their role in calcium transport and disease. Muscle & Nerve 35:430-442.
137. Myint W, Cai Y, Schiffer C, Ishima R (2012) Quantitative comparison of errors in 15N transverse relaxation rates measured using various CPMG phasing schemes. Journal of Biomolecular NMR 53:13-23.
138. Myint W, Gong Q, Ahn J, Ishima R (2011) Characterization of sarcoplasmic reticulum Ca2+ ATPase nucleotide binding domain mutants using NMR spectroscopy. Biochemical and Biophysical Research Communications 405:19-23.
139. Myint W, Gong Q, Ishima R (2009) Practical aspects of 15N CPMG transverse relaxation experiments for proteins in solution. Concepts Magn Reson 34A:63-75.
140. Myint W, Ishima R (2009) Chemical exchange effects during refocusing pulses in constant-time CPMG relaxation dispersion experiments. J Biomol NMR 45:207-216.
141. Nagai H, Sato A, Kiyoshi T, Matsumoto F, Wada H, Ito S, Miki T, Yoshikawa M, Kawate Y, Fukui S (2001) Development and testing of superfluid-cooled 900 MHz NMR magnet. Cryogenics 41:623-630.
142. Nalam MN, Peeters A, Jonckers TH, Dierynck I, Schiffer CA (2007) Crystal structure of lysine sulfonamide inhibitor reveals the displacement of the conserved flap water molecule in human immunodeficiency virus type 1 protease. J Virol 81:9512-9518.
143. Neuhaus D, Williamson MP. 2000. The Nuclear Overhauser Effect in Structural and Conformational Analysis, A John Wiley & Sons, Inc., New York.
144. Nicholson LK, Kay LE, Baldisseri DM, Arango J, Young PR, Bax A, Torchia DA (1992) Dynamics of methyl groups in proteins as studied by proton-detected 13C NMR spectroscopy. Application to the leucine residues of Staphylococcal nuclease. Biochemistry 31:5253-5263.
145. Nielsen G, Malmendal A, Meissner A, Moller JV, Nielsen NC (2003) NMR studies of the fifth transmembrane segment of sarcoplasmic reticulum Ca2+-ATPase reveals a hinge close to the Ca2+-ligating residues. FEBS Lett 544:50-56.
146. Nirmala NR, Wagner G (1988) Measurement of C-13 relaxation-times in proteins by two-dimensional heteronuclear H1-C-13 correlation spectroscopy. J Am Chem Soc 110:7557-7558.
147. Olejniczak E, Xu R, Fesik S (1992) A 4D HCCH-TOCSY experiment for assigning the side chain1H and13C resonances of proteins. Journal of Biomolecular NMR 2:655-659.
148. Olesen C, Picard M, Winther A-ML, Gyrup C, Morth JP, Oxvig C, Moller JV, Nissen P (2007) The structural basis of calcium transport by the calcium pump. Nature 450:1036-1042.

149. Olesen C, Sorensen TL, Nielsen RC, Moller JV, Nissen P (2004) Dephosphorylation of the calcium pump coupled to counterion occlusion. Science 306:2251-2255.
150. Orekhov VY, Pervushin KV, Arseniev AS (1994) Backbone dynamics of (1-71)bacterioopsin studied by two-dimensional 1H-15N NMR spectroscopy. Eur J Biochem 219:887-896.
151. Ozen A, Haliloglu T, Schiffer CA (2011) Dynamics of Preferential Substrate Recognition in HIV-1 Protease: Redefining the Substrate Envelope. J Mol Biol 410:726-744.
152. Palmer AG, 3rd (1997) Probing molecular motion by NMR. Curr Opin Struct Biol 7:732-737.
153. Palmer AG, 3rd (2001) Nmr probes of molecular dynamics: overview and comparison with other. Annu Rev Biophys Biomol Struct 30:129-155.
154. Palmer AG, Rance M, Wright PE (1991) Intramolecular motions of a zinc finger DNA-binding domain from Xfin characterized by proton-detected natural abundance 13C Heteronuclear NMR spectroscopy. J Am Chem Soc 113:4371-4380.
155. Palmer AG, Skelton NJ, Chazin WJ, Wright PE, Rance M (1992) Suppression of the Effects of Cross-Correlation between Dipolar and Anisotropic Chemical-Shift Relaxation Mechanisms in the Measurement of Spin Spin Relaxation Rates. Molecular Physics 75:699-711.
156. Palmer AGr, Massi F (2006) Characterization of the dynamics of biomacromolecules using rotating-frame spin relaxation NMR spectroscopy. Chem Rev 106:1700-1719.
157. Pang Y, Buck M, Zuiderweg ER (2002) Backbone dynamics of the ribonuclease binase active site area using multinuclear ((15)N and (13)CO) NMR relaxation and computational molecular dynamics. Biochemistry 41:2655-2666.
158. Peng JW, Thanabal V, Wagner G (1991) Improved accuracy of heteronuclear transverse relaxation time measurements in macromolecules. elimination of antiphase contributions. J Magn Reson 85:421-427.
159. Peng JW, Wagner G (1995) Frequency spectrum of NH bonds in eglin c from spectral density mapping at multiple fields. Biochemistry 34:16733-16752.
160. Periasamy M, Huke S (2001) SERCA Pump Level is a Critical Determinant of Ca2+Homeostasis and Cardiac Contractility. Journal of Molecular and Cellular Cardiology 33:1053-1063.
161. Perryman AL, Lin JH, McCammon JA (2004) HIV-1 protease molecular dynamics of a wild-type and of the V82F/I84V mutant: possible contributions to drug resistance and a potential new target site for drugs. Protein Sci 13:1108-1123.
162. Piper HM, Kasseckert S, Abdallah Y (2006) The sarcoplasmic reticulum as the primary target of reperfusion protection. Cardiovascular Research 70:170-173.
163. Powers R, Gronenborn AM, Marius Clore G, Bax A (1991) Three-dimensional triple-resonance NMR of 13C/15N-enriched proteins using constant-time evolution. Journal of Magnetic Resonance (1969) 94:209-213.
164. Prabu-Jeyabalan M, Nalivaika E, Schiffer CA (2000) How does a symmetric dimer recognize an asymmetric substrate? A substrate complex of HIV-1 protease. J Mol Biol 301:1207-1220.
165. Prabu-Jeyabalan M, Nalivaika EA, King NM, Schiffer CA (2003) Viability of a drug-resistant HIV-1 protease variant: structural insights for better anti-viral therapy. J Virol 77:1306-1315.

166. Redfield C (2004) Using nuclear magnetic resonance spectroscopy to study molten globule states of proteins. Methods Mol Biol 34:121-132.
167. Ringpfeil F, Raus A, DiGiovanna JJ, Korge B, Harth W, Mazzanti C, Uitto J, Bale SJ, Richard G (2001) Darier disease – novel mutations in ATP2A2 and genotype–phenotype correlation. Experimental Dermatology 10:19-27.
168. Rodriguez EJ, Debouck C, Deckman IC, Abusoud H, Raushel FM, Meek TD (1993) Inhibitor Binding to the Phe53trp Mutant of Hiv-1 Protease Promotes Conformational-Changes Detectable by Spectrofluorometry. Biochemistry 32:3557-3563.
169. Ross A, Czisch M, King GC (1997) Systematic errors associated with the CPMG pulse sequence and their effect on motional analysis of biomolecules. Journal of Magnetic Resonance 124:355-365.
170. Ruiz-Perez VL, Carter SA, Healy E, Todd C, Rees JL, Steijlen PM, Carmichael AJ, Lewis HM, Hohl D, Itin P, Vahlquist A, Gobello T, Mazzanti C, Reggazini R, Nagy G, Munro CS, Strachan T (1999) ATP2A2 mutations in Darier's disease: variant cutaneous phenotypes are associated with missense mutations, but neuropsychiatric features are independent of mutation class. Hum Mol Genet 8:1621-1630.
171. Rule GS, Hichens KT. 2006. Fundamentals of Protein NMR Spectroscopy, Springer, Dordrecht, The Netherlands.
172. Sakuntabhai A, Ruiz-Perez V, Carter S, Jacobsen N, Burge S, Monk S, Smith M, Munro CS, O'Donovan M, Craddock N, Kucherlapati R, Rees JL, Owen M, Lathrop GM, Monaco AP, Strachan T, Hovnanian A (1999) Mutations in ATP2A2, encoding a Ca2+ pump, cause Darier disease. Nat Genet 21:271-277.
173. Schmidt U, Hajjar RJ, Helm PA, Kim CS, Doye AA, Gwathmey JK (1998) Contribution of Abnormal Sarcoplasmic Reticulum ATPase Activity to Systolic and Diastolic Dysfunction in Human Heart Failure. Journal of Molecular and Cellular Cardiology 30:1929-1937.
174. Scott WR, Schiffer CA (2000) Curling of flap tips in HIV-1 protease as a mechanism for substrate entry and tolerance of drug resistance. Structure 8:1259-1265.
175. Shafer RW, Stevenson D, Chan B (1999) Human immunodeficiency virus reverse transcriptase and protease sequence database. Nucleic Acids Res 27:348-352.
176. Shaka AJ, Barker PB, Freeman R (1985) Computer-optimized decoupling scheme for wideband applications and low-level operation. J Magn Reson 64:547-552.
177. Shaka AJ, Keeler J, Frenkiel T, Freeman R (1983) An Improved Sequence for Broadband Decoupling: WALTZ-16. J Magn Reson 52:335-338.
178. Skelton NJ, Palmer AG, Akke M, Kordel J, Rance M, Chazin WJ (1993) Practical Aspects of 2-Dimensional Proton-Detected N-15 Spin Relaxation Measurements. Journal of Magnetic Resonance Series B 102:253-264.
179. Skrynnikov NR, Dahlquist FW, Kay LE (2002) Reconstructing NMR spectra of "invisible" excited protein states using. J Am Chem Soc 124:12352-12360.
180. Smith LJ, Mark AE, Dobson CM, van Gunsteren WF (1995) Comparison of MD simulations and NMR experiments for hen lysozyme. Analysis of local fluctuations, cooperative motions, and global changes. Biochemistry 34:10918-10931.
181. Solomon I (1955) Relaxation Processes in a System of Two Spins. Physical Review 99:559-565.
182. Sorensen TL, Moller JV, Nissen P (2004) Phosphoryl transfer and calcium ion occlusion in the calcium pump. Science 304:1672-1675.

183. Spinelli S, Liu QZ, Alzari PM, Hirel PH, Poljak RJ (1991) The three-dimensional structure of the aspartyl protease from the HIV-1 isolate BRU. Biochimie 73:1391-1396.
184. Stocker U, van Gunsteren WF (2000) Molecular dynamics simulation of hen egg white lysozyme: A test of the GROMOS96 force field against nuclear magnetic resonance data. Proteins 40:145-153.
185. Styles P, Soffe NF, Scott CA (1989) An improved cryogenically cooled probe for high-resolution NMR. Journal of Magnetic Resonance (1969) 84:376-378.
186. Styles P, Soffe NF, Scott CA, Crag DA, Row F, White DJ, White PCJ (1984) A high-resolution NMR probe in which the coil and preamplifier are cooled with liquid helium. Journal of Magnetic Resonance (1969) 60:397-404.
187. Sugase K, Dyson HJ, Wright PE (2007) Mechanism of coupled folding and binding of an intrinsically disordered protein. Nature 447:1021-1025.
188. Szyperski S, Luginbühl P, Otting G, Güntert P, Wüthrich K (1993) Protein dynamics studied by rotating frame. J Biomol NMR 3:151-164.
189. Tavadia S, Tait RC, McDonagh TA, Munro CS (2001) Platelet and cardiac function in Darier's disease. Clin Exp Dermatol 26:696-699.
190. Tolkatchev D, Xu P, Ni F (2003) Probing the kinetic landscape of transient peptide-protein interactions by use of peptide (15)n NMR relaxation dispersion spectroscopy: binding of an antithrombin peptide to human prothrombin. J Am Chem Soc 125:12432-12442.
191. Tollinger M, Skrynnikov NR, Mulder FA, Forman-Kay JD, Kay LE (2001) Slow dynamics in folded and unfolded states of an SH3 domain. J Am Chem Soc 123:11341-11352.
192. Toyoshima C (2009) How Ca2+-ATPase pumps ions across the sarcoplasmic reticulum membrane. Biochim Biophys Acta 1793:941-946.
193. Toyoshima C, Nomura H (2002) Structural changes in the calcium pump accompanying the dissociation of calcium. Nature 418:605-611.
194. Trzesniak D, Glattli A, Jaun B, van Gunsteren WF (2005) Interpreting NMR data for beta-peptides using molecular dynamics simulations. J Am Chem Soc 127:14320-14329.
195. Valentine ER, Palmer AG, 3rd (2005) Microsecond-to-millisecond conformational dynamics demarcate the GluR2. Biochemistry 44:3410-3417.
196. van Gunsteren WF, Dolenc J, Mark AE (2008) Molecular simulation as an aid to experimentalists. Curr Opin Struc Biol 18:149-153.
197. Veglia G, Ha KN, Shi L, Verardi R, Traaseth NJ (2010) What can we learn from a small regulatory membrane protein? Methods Mol Biol 654:303-319.
198. Viles JH, Duggan BM, Zaborowski E, Schwarzinger S, Huntley JJ, Kroon GJ, Dyson HJ, Wright PE (2001) Potential bias in NMR relaxation data introduced by peak intensity analysis and curve fitting methods. J Biomol NMR 21:1-9.
199. Wagner G, Bruehwiler D (1986) Toward the complete assignment of the carbon nuclear magnetic resonance spectrum of the basic pancreatic trypsin inhibitor. Biochemistry 25:5839-5843.
200. Wang C, Grey MJ, Palmer AG, 3rd (2001) CPMG sequences with enhanced sensitivity to chemical exchange. J Biomol NMR 21:361-366.
201. Wang CY, Rance M, Palmer AG (2003) Mapping chemical exchange in proteins with MW > 50 kD. Journal of the American Chemical Society 125:8968-8969.
202. Wang L, Pang Y, Holder T, Brender JR, Kurochkin AV, Zuiderweg ER (2001) Functional dynamics in the active site of the ribonuclease binase. Proc Natl Acad Sci U S A 98:7684-7689.

203. Winther AM, Liu H, Sonntag Y, Olesen C, le Maire M, Soehoel H, Olsen CE, Christensen SB, Nissen P, Moller JV (2010) Critical roles of hydrophobicity and orientation of side chains for inactivation of sarcoplasmic reticulum Ca2+-ATPase with thapsigargin and thapsigargin analogs. J Biol Chem 285:28883-28892.
204. Wlodawer A, Erickson JW (1993) Structure-based inhibitors of HIV-1 protease. Annual Review of Biochemistry 62:543-585.
205. Wlodawer A, Miller M, Jaskolski M, Sathyanarayana BK, Baldwin E, Weber IT, Selk LM, Clawson L, Schneider J, Kent SB (1989) Conserved folding in retroviral proteases: crystal structure of a synthetic HIV-1 protease. Science 245:616-621.
206. Wrabl JO, Shortle D, Woolf TB (2000) Correlation between changes in nuclear magnetic resonance order parameters and conformational entropy: molecular dynamics simulations of native and denatured staphylococcal nuclease. Proteins 38:123-133.
207. Yamasaki K, Saito M, Oobatake M, Kanaya S (1995) Characterization of the internal motions of Escherichia coli ribonuclease HI by a combination of 15N-NMR relaxation analysis and molecular dynamics simulation: examination of dynamic models. Biochemistry 34:6587-6601.
208. Yang DW, Kay LE (1996) Contributions to conformational entropy arising from bond vector fluctuations measured from NMR-derived order parameters: Application to protein folding. Journal of Molecular Biology 263:369-382.
209. Yip GN, Zuiderweg ER (2004) A phase cycle scheme that significantly suppresses offset-dependent artifacts in the R2-CPMG 15N relaxation experiment. J Magn Reson 171:25-36.
210. Zamoon J, Nitu F, Karim C, Thomas DD, Veglia G (2005) Mapping the interaction surface of a membrane protein: unveiling the conformational switch of phospholamban in calcium pump regulation. Proc Natl Acad Sci U S A 102:4747-4752.